

Novel Applications of Eutectic Freeze Crystallization

Xiaoqian Lu



Novel Applications of Eutectic Freeze Crystallization

Proefschrift

ter verkrijging van de graad van doctor
aan de Technische Universiteit Delft,
op gezag van de Rector Magnificus prof. ir. K.C.A.M. Luyben,
voorzitter van het college voor Promoties,
in het openbaar te verdedigen op vrijdag 12 september 2014 om 10.00 uur

door

Xiaoqian LU

Bachelor of Materials Science and Engineering (Shandong Jianzhu University)
Geboren te Jinan, Shandong, China

Dit proefschrift is goedgekeurd door de promotor:

Prof. dr. G.J. Witkamp

Copromotor Dr. F.E. Genceli Güner

Samenstelling promotiecommissie:

Rector Magnificus

Prof. dr. G.J. Witkamp

Dr. F.E. Genceli Güner

Prof. dr. S.R.A. Kersten

Prof. dr. ir. B.J. Boersma

Prof. dr. ir. T.J.H. Vlugt

Prof. dr. P.C. Rem

Prof. dr. P. Osseweijer

voorzitter

Technische Universiteit Delft, promotor

Technische Universiteit Delft, copromotor

Istanbul Technical University

Universiteit Twente

Technische Universiteit Delft

Technische Universiteit Delft

Technische Universiteit Delft

Technische Universiteit Delft

Dr. J. van Spronsen heeft als begeleider in belangrijke mate aan de totstandkoming van het proefschrift bijgedragen.

This research is supported by the China Scholarship Council ([2009]).

ISBN: 978-94-6186-341-6



Table of Contents

| | | |
|-----------------------------|--|-----|
| Chapter 1 | Introduction | 1 |
| Chapter 2 | Eutectic Freeze Crystallization of Nickel Sulfate from an Industrial Stream: a Comparison with Evaporative Crystallization | 13 |
| Chapter 3 | Recrystallization of $\text{NiSO}_4 \cdot 7\text{H}_2\text{O}$ into $\text{NiSO}_4 \cdot 6\text{H}_2\text{O}$ | 35 |
| Chapter 4 | Analysis of NiSO_4 Samples by hrICP-MS | 55 |
| Chapter 5 | Desalination of Oil Coproduced Water by Eutectic Freeze Crystallization | 85 |
| Chapter 6 | Eutectic Freeze Crystallization as a Tool for Separation of Shale Gas Produced Water into Pure Ice and Salt | 103 |
| Chapter 7 | Crystal Structure, Stability, and Electronic Properties of Hydrated Metal Sulfates $\text{MSO}_4(\text{H}_2\text{O})_n$ ($\text{M}=\text{Ni}, \text{Mg}$; $n=6,7$) and Their Mixed Phases: A First Principles Study | 121 |
| Samenvatting | Nieuwe Toepassingen van Eutectische Vrieskristallisatie | 147 |
| Summary | Novel Applications of Eutectic Freeze Crystallization | 151 |
| Acknowledgements | | 153 |
| Curriculum Vitae | | 157 |
| List of Publications | | 158 |



To my dear mom and dad

致我亲爱的爸爸妈妈



Chapter 1

Introduction

1.1 Background

The rapid progress of science and society is strongly related to the increasing demand and consumption of raw materials and energy. A 30-year increase of 56 percent of the world total energy consumption is predicted (**Figure 1.1**). Almost 80 percent of the energy is produced from fossil fuel such as crude oil and natural gas. The increasing consumption of energy will lead to a higher rate of depletion for these two resources (U.S. Energy Information Administration, 2013)(**Figure 1.2**).

Intricately connected to energy is the demand for water. For an overview, the global water use is demonstrated in **Figure 1.3** (Shiklomanov, 1999). We can see from this figure that since 1950, the yearly world fresh water consumption for urban population needs (domestic water consumption), industry (including thermal power), irrigated farming and agriculture keeps increasing with approximately 27 km³ per year. Currently, the production of crude oil requires huge amounts of water in the stages of drilling, pumping, refinement and treatment. The average water use is estimated to be 1.058 m³ per GJ (Gerbens-Leenes P. W. et al., 2008). For conventional gas sources the water requirement is at an estimation of 0.109 m³ per GJ (Gerbens-Leenes P. W. et al., 2008); whereas, for shale gas production, more water is needed since its extraction method, hydraulic fracturing, requires millions of liters of water for each well (United Nations World Water, 2012). The growth of the world population (United Nations, 2011) also aggravates the water problem. It is predicted that by 2025, 1.8 billion people will live in regions with absolute water scarcity, and two-thirds of the world's population could be living under water stressed conditions (Food and Agriculture Organization, 2012). Also the global metals consumption keeps increasing as shown in **Table 1.1** (The World Bank Group, 2006). In fifteen years, the consumption of 6 major industrial metals (Aluminum, Copper, Lead, Nickel, Tin and Zinc) grew on an average varying from 2.1% to 3.9% per annum. The relieving thing is that recovery of these metals is simultaneously happening. According to the recycling report from U.S. Geological Survey (Papp, 2011), the United States recycled 68.8 million metric tons (Mt) of selected metals, an amount equivalent to 62% of the apparent supply of those metals.

Of all the energy and raw materials-consuming sectors, industrial sector consumes about one-half of the world's total produced energy (**Figure 1.4a**), which is much more than any other end-use sector (U.S. Energy Information Administration, 2013). Meanwhile, this energy consumption increases faster than prediction, for instance, the total industrial delivered energy consumption in 2040 in AEO 2014 is 5% higher than in AEO 2013 (U.S. Energy Information Administration, 2014). It is reported that approximately 20 % of the world's freshwater withdrawals are used by industry (United Nations World Water, 2012). The detailed data for industrial water use are shown

in **Figure 1.4b** (Shiklomanov, 1999). Besides water and energy the metallurgical industries use a great amounts of ores that contain next to required metals increasing levels of impurities. These impurities have to be removed in an environmentally friendly way. For example, **Table 1.2** lists the impurities contained in crude nickel sulfate from copper production and in commercially available nickel sulfate, and gives specifications of nickel sulfate for electroplating and catalyst production (Danish Environmental Protection Agency, 2008). It is worthwhile to recycle these impurities.

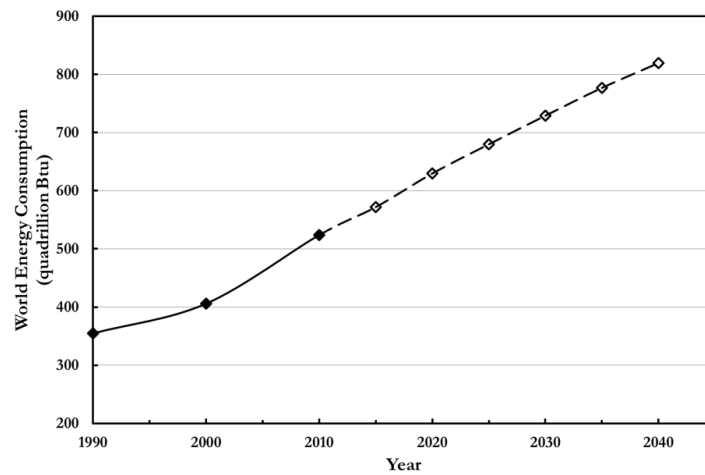


Figure 1.1 World energy consumption (U.S. Energy Information Administration, 2013).
(1 quadrillion Btu = 1.055×10^{18} joules)

Table 1.1 Global metals consumption, 1990-2005 (The World Bank Group, 2006).

| | Aluminum | Copper | Lead | Zinc | Nickel | Tin | Iron Ore |
|-----------|-----------------------|--------|-------|--------|--------|------|---------------------|
| | 10 ³ ton | | | | | | 10 ⁶ ton |
| 1990 | 18,009 | 10,755 | 5,511 | 6,671 | 856 | 238 | 976 |
| 2005 | 31,947 | 16,930 | 7,524 | 10,580 | 1,236 | 332 | 1,455 |
| | Growth rates (% CAGR) | | | | | | |
| 1990-2005 | 3.9% | 3.1% | 2.1% | 3.1% | 2.5% | 2.3% | 2.7% |

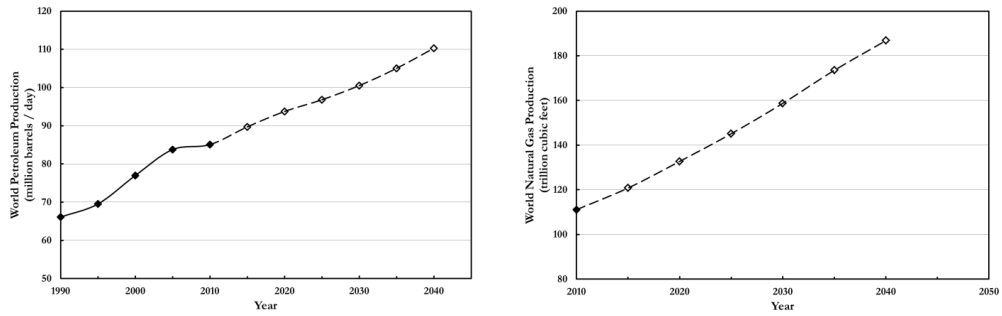


Figure 1.2 World petroleum and natural gas production (U.S. Energy Information Administration, 2013).

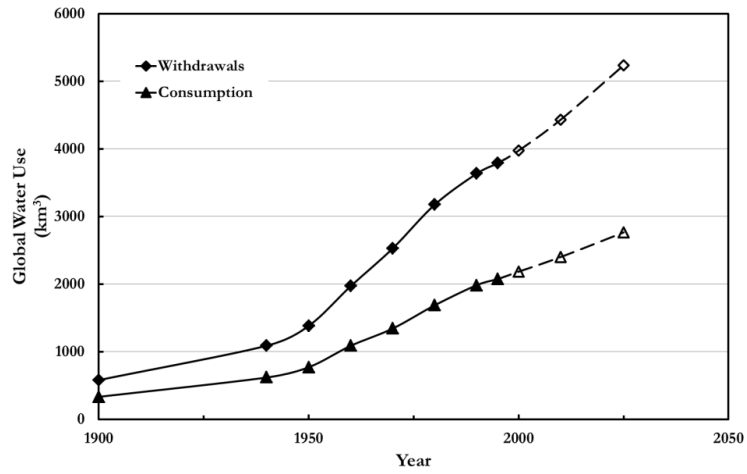


Figure 1.3 Global water use from water natural resources (Shiklomanov, 1999).

Table 1.2 Impurity distribution in crude nickel sulfate from copper production and in commercially available nickel sulfate. Specifications of nickel sulfate for electroplating and catalyst production (Danish Environmental Protection Agency, 2008).

| NiSO ₄ | Crude | Electroplating | Catalysts | Commercial |
|-------------------|----------------|----------------|----------------|----------------|
| Element | assay mg/kg | Spec. mg/kg | Spec. mg/kg | assay mg/kg |
| Co | 50-100 | 5000 | 1000 | <100 |
| Zn | 2500-5000 | 30 | 200 | <10 |
| Fe | 1000-2000 | 20 | 40 | <5 |
| Cu | 1700-6000 | 20 | 40 | <5 |
| Pb | 140-460 | 10 | 40 | <5 |
| Cd | 50-125 | 10 | 20 | <4 |
| As | 1500-3000 | 10 | 20 | <1 |

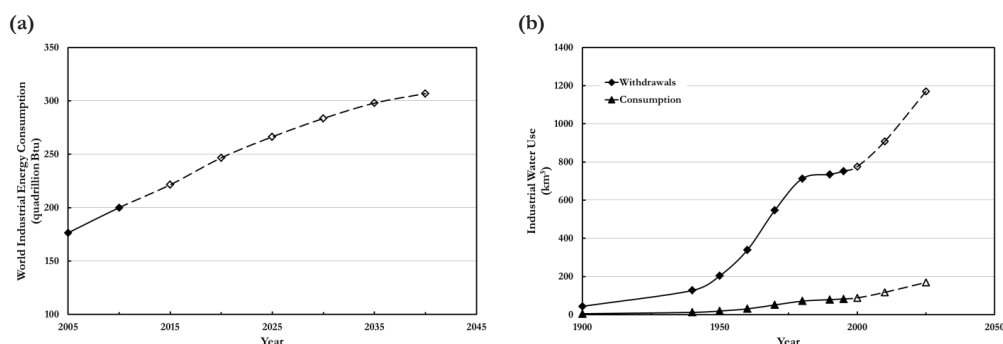


Figure 1.4 Energy consumption (a) (U.S. Energy Information Administration, 2013) and water use (b) (Shiklomanov, 1999) for industrial sector.

Since the Industrial Revolution, the development of a country is significantly dependent on industry. In the category of industries, the Primary (or extractive) and Secondary (or Manufacturing) industrial sectors consume most of the raw materials and energy compared to the other industrial sectors (tertiary or services, quaternary or knowledge, and quinary or culture and research). They involve the extraction of resources directly from the earth, and the processing products from the primary industries. In these two kinds of industrial sectors, separation technology is an essentially key technique since plenty of valuable raw materials staying in the waste etc. need to be recovered due to ecological and economical reasons. Meanwhile, separations are the most costly process in industrial sectors because of the high equipment investment and vast energy consumption. At this moment huge amounts of valuable industrial aqueous streams needs to be disposed in an energy-friendly way while energy might be saved and the valuable materials might be recovered if suitable technologies were available.

Based on the driving force, separation technology can be broadly divided into four categories: e.g., thermal (based on temperature differences), pressure, electrical potential, and chemical potential-driven processes (Waly, 2011). Depending on the types of the aqueous solutions, the most commonly used technologies for separation, their principles and disadvantages are listed in **Table 1.3**. Unfortunately, all of the mentioned separation technologies have their own specific theoretical and technological drawbacks. A promising separation technology should apparently be “an optimized process with respect to selectivity, conversion, energy efficiency, minimization of waste and the usage of hazardous extra materials” (Ulrich, 2004). Consequently, to find a novel separation technology with low energy consumption and high quality products without additional chemicals is essential from the sustainable point of view. Eutectic Freeze Crystallization (EFC) is a promising candidate for such a novel process. EFC has been proven to recover high quality products such as pure water and salt with commercial value for sale. Furthermore, it is evident that

EFC not only replaces existing technologies, but also constitutes a new unit operation that can be combined with other separation technologies.

Table 1.3 Conventional separation technologies.

| Technology | Separation principle | Disadvantage |
|---|--|--|
| Removal of low solute concentrations | | |
| Solvent extraction | A selective solute from the aqueous phase is separated out by dissolving in an additional solvent | <ul style="list-style-type: none"> Additional chemicals Re-separation requirements |
| Reverse osmosis | Solution is pressurized against a selective membrane, which only allows the pure solvent to pass | <ul style="list-style-type: none"> Sensitive to fouling and scaling |
| Ion exchange/adsorption | To remove dissolved ions from solution and replace them with other similarly charged ions/to adhere the dissolved solvent to a surface of the adsorbent. | <ul style="list-style-type: none"> Fouling (iron/Calcium sulfate) Organic contamination from the Resin Thermal/design problems of adsorbent |
| Removal of high solute concentrations | | |
| Evaporative crystallization | To Crystallize the solutes by vaporizing the solvent to reach the needed supersaturation | <ul style="list-style-type: none"> High energy consumption Operation at high working temperature |
| Cooling crystallization | To crystallize the crystals by cooling the solution below its saturation temperature | <ul style="list-style-type: none"> A positive and steep solubility- temperature line Limited yield |
| Anti-solvent crystallization | To add anti-solvent into the solution that has selective affinity with water to reduce salt solubility | <ul style="list-style-type: none"> Extra chemicals Recovery for anti-solvent |
| Precipitation | To add extra reactant to form a sparingly soluble product and conversion to solid particles | <ul style="list-style-type: none"> Extra chemicals Formation of unexpected solid phase |
| Membrane crystallization | To remove the solvent from the solution by membrane to create or to enhance generation of crystals | <ul style="list-style-type: none"> Scale formation on the membrane surface |
| Removal of both low and high solute concentrations | | |
| Freeze crystallization | To remove water by ice formation | <ul style="list-style-type: none"> Not suit for eutectic systems |

1.2 Eutectic Freeze Crystallization

Crystallization is a recovery process for a dissolved compound forming a crystalline phase. This process is closely associated with the thermodynamics of the system expressed by its phase diagram, which represent the stable state of the solid and liquid phases in the range of temperature, pressure and composition. **Figure 1.5** (Pascual, 2009) illustrates a binary phase diagram for the eutectic system, which is the common situation for the inorganic compounds. There are regions of one phase (solution), two phases (ice in equilibrium with the solution; salt with solution; ice and salt) and three phases (ice, salt and solution in equilibrium at the eutectic point E). In our investigation of Eutectic Freeze Crystallization, aqueous solutions with eutectic point were the main research objects.

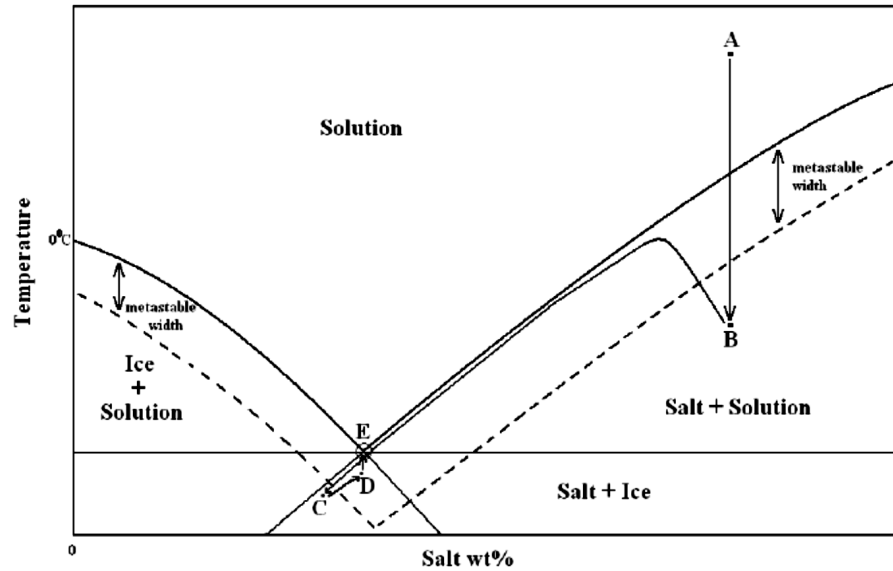


Figure 1.5 Kinetics in a general phase diagram for binary aqueous solutions (Pascual, 2009).

1.2.1 Definition and principle

Eutectic Freeze Crystallization (EFC) is a combination of crystallization by concentration and freeze crystallization. The ice freezes out by freeze crystallization, and the other compound crystallizes because of the increasing concentration. In **Figure 1.5**, the phase equilibrium information is depicted in terms of solubility lines at constant pressure, which means the solid is in equilibrium with the solution under the specific temperature and concentration. EFC is the technology used in this diagram to separate aqueous solution into ice and solidified solute simultaneously by operating near the eutectic point (Vaessen et al., 2003). The so called eutectic point is the intersection of the ice line and the salt solubility line. The composition of the feed solution can be either higher or lower than the concentration at the eutectic point E. For example (in a batch process) a solution at point A in the phase diagram is cooled down. Upon crossing the solubility line of the salt, the solution becomes supersaturated. Within the metastable zone, there will be no primary nucleation and growth of salt crystals to be observed. Only when passing this region, the crystallization of the salt visibly starts at point B. The temperature suddenly increases because of the heat release of salt crystallization, and the salt concentration in solution decreases. The solution conditions remain close to the solubility line until traversing the metastable region of ice, and ice starts to form at point C. Ice and salt then crystallizes simultaneously at supersaturated

conditions D below the eutectic point. The equilibrium of the system of ice, salt and solution is at the eutectic point E. A similar scheme applies to the solution with a lower concentration than the eutectic composition; the ice crystallizes first instead of the solute. For a more complex solution EFC still works. Ice and one of the compounds are crystallized first, and leave a more concentrated mixture of the other compounds; in subsequent steps, ice and the other compounds will crystallize one by one. Crystallization is a separation process where the crystallized solids can be of high purity after separation. Since EFC is a cooling process where the heat of crystallization is only one sixth of evaporation, a less energy consumption is needed than for evaporative crystallization. Since eutectic freeze crystallization is a spontaneous separation process where no further chemicals are added, no more chemical treatments are required. After crystallization, ice floats to the top of the vessel and the other compounds settle to the bottom, and the separation of the ice and the salts from their mixture is facilitated.

1.2.2 State of the art of Eutectic Freeze Crystallization

Thermodynamically the eutectic coexistence of ice and salts in equilibrium has been known since long time, and earlier efforts were performed to apply it to the production of drinking water from for instance sea water using natural cold sources in winter (Barduhn, 1963; Powell, 1964; Stepakoff et al., 1974). This was found too expensive and no further development of a consistent process, equipment and product system has taken place. Swenne and Thoenes (Swenne and Thoenes, 1985) have investigated at laboratory scale the eutectic crystallization of sodium chloride. In Delft the first full continuous EFC crystallizer system was designed, constructed and tested in an industrial environment (Genceli et al., 2005; Himawan, 2005; Pascual et al., 2010; Vaessen et al., 2003; Van Der Ham et al., 1999), and process design calculations have shown that EFC is not only technically, but also economically an attractive technology. Pronk (Pronk et al., 2008) developed eutectic freeze in a fluidized bed column at pilot scale.

1.3 Scope of the research and outline of the thesis

Now that EFC over the last two decades has principally been proven to work from an equipment, process and product perspective, industrial applications can be addressed. The aim of this research was to investigate the feasibility of EFC for the treatment of streams from the chemical, oil and shale gas industries. Because the value of the obtained salt and water depend upon their purity, special attention was paid to develop and apply analytical techniques to determine the fate of trace impurities in the purification process.

Chapter 2 focuses on the feasibility of EFC for a NiSO_4 industrial stream from lab scale experiments to pilot plant scale demonstration. Pure $\text{NiSO}_4 \cdot 7\text{H}_2\text{O}$ crystals were recovered as well as

sufficiently pure water suitable for recycling into the process. Because of the high Na content in the original industrial stream, the quaternary point of the $\text{NaSO}_4/\text{NiSO}_4/\text{H}_2\text{O}$ system was determined in our work. The final $\text{NiSO}_4 \cdot 7\text{H}_2\text{O}$ product from EFC was compared with the product from evaporative crystallization in order to prove the advantages of EFC.

Chapter 3 describes how the $\text{NiSO}_4 \cdot 7\text{H}_2\text{O}$ product from the industrial solution in Chapter 2 was treated further by recrystallization into $\text{NiSO}_4 \cdot 6\text{H}_2\text{O}$. Recrystallization proved to be an extra purification step for $\text{NiSO}_4 \cdot 7\text{H}_2\text{O}$. Partition coefficients and distribution coefficients were determined from the analytical data obtained by hrICP-MS and used to characterize the purification performance.

Chapter 4 shows more impurity concentrations in the nickel sulfate systems and how they were measured by hrICP-MS.

In Chapter 5, the feasibility of EFC for treating oil co-produced water from the oil industry was investigated. EFC could be used to recover the main constituent sodium chloride in form of $\text{NaCl} \cdot 2\text{H}_2\text{O}$ and pure water successfully at 1 liter and 10 liter laboratorial scale. Anhydrous NaCl with a higher quality could be obtained by an additional purification recrystallization step.

Chapter 6 concentrates on the feasibility of using EFC for the treatment of shale gas water produced from the shale gas industry. The process was scaled up from 1 liter to 10 liter and 200 liter scale. High quality pure water was recovered successfully to meet the target of reducing the amount of disposed water. The eutectic points of the different salts were determined by this specific composition.

In Chapter 7, we have investigated an industrial problem of removing Mg from hydrated Ni sulfates using state-of-the-art molecular simulations. Periodic Density Functional Theory (DFT) and cluster DFT calculations are used to study the crystal structures and phase stability of the hexahydrated and heptahydrated Ni and Mg sulfates and their mixed phases. The calculated lattice parameters of $\text{MSO}_4(\text{H}_2\text{O})_n$ ($\text{M}=\text{Ni}, \text{Mg}; n=6,7$) crystals are in good agreement with available experimental data.

References

- Danish Environmental Protection Agency, 2008. The Risk Assessment Report on Nickel Sulphate.
- Food and Agriculture Organization, 2012. http://www.unwater.org/statistics_res.html.
- The World Bank Group, 2006. The Outlook for Metals Markets. http://siteresources.worldbank.org/INTOGMC/Resources/outlook_for_metals_market.pdf.
- U.S. Energy Information Administration, 2014. Annual Energy Outlook 2014 Early Release Overview. [http://www.eia.gov/forecasts/aeo/er/pdf/0383er\(2014\).pdf](http://www.eia.gov/forecasts/aeo/er/pdf/0383er(2014).pdf).
- U.S. Energy Information Administration, 2013. International Energy Outlook 2013. [http://www.eia.gov/forecasts/ieo/pdf/0484\(2013\).pdf](http://www.eia.gov/forecasts/ieo/pdf/0484(2013).pdf).
- United Nations World Water, 2012. Managing Water under Uncertainty and Risk. <http://unesdoc.unesco.org/images/0021/002156/215644e.pdf>.
- United Nations, 2011. Seven Billion and Growing: the Role of Population Policy in Achieving Sustainability. http://www.un.org/esa/population/publications/technicalpapers/IP2011-3_SevenBillionandGrowing.pdf
- Barduhn, A.J., 1963. Waste Water Renovation: Part 1. A Design Study of Freezing and Gas Hydrate Formation. Public Health Service Publication.
- Genceli, F.E., Trambitas, D., Gartner, R.S. and Witkamp, G.J., 2005. 3rd generation Cooled Disk Column Crystallizer and a Skid Mounted Unit for Eutectic Freeze Crystallization. 16th International Symposium on Industrial Crystallization, D-15: 855-860.
- Gerbens-Leenes P. W., Hoekstra, A.Y. and Van der Meer, T.H., 2008. Water Footprint of Bio-Energy and Other Primary Energy Carriers. Value of Water Research Report Series. <http://www.waterfootprint.org/Reports/Report29-WaterFootprintBioenergy.pdf>
- Himawan, C., 2005. Characterization and Population Balance Modelling of Eutectic Freeze Crystallization, PhD Thesis, Delft University of Technology.
- Papp, J.F., 2011. 2011 Minerals Yearbook: Recycling, Metals. <http://minerals.usgs.gov/minerals/pubs/commodity/recycle/myb1-2011-recyc.pdf>.
- Pascual, M.R., 2009. Physical Aspects of Scraped Heat Exchanger Crystallizers: an Application in Eutectic Freeze Crystallization, PhD thesis, Delft University of Technology.
- Pascual, M.R. et al., 2010. A novel scraped cooled wall crystallizer. Recovery of sodium carbonate and ice from an industrial aqueous solution by eutectic freeze crystallization. Chemical Engineering Research and Design, 88(9): 1252-1258.
- Powell, R.L., 1964. A Study of the Concentration of Waste Water by Eutectic Freezing. M. S. thesis, Syracuse University.
- Pronk, P., Ferreira, C.A.I. and Witkamp, G.J., 2008. Prevention of crystallization fouling during eutectic freeze crystallization in fluidized bed heat exchangers. Chem Eng Process, 47(12): 2140-2149.
- Shiklomanov, I.A., 1999. World Water Resources: Modern Assessment and Outlook for the 21st Century (Summary of World Water Resources at the Beginning of the 21st Century, prepared in the framework of the IHP UNESCO). <http://webworld.unesco.org/water/ihp/db/shiklomanov/>.
- Stepakoff, G.L., Siegelman, D., Johnson, R. and Gibson, W., 1974. Development of a eutectic freezing process for brine disposal. Desalination, 14(1): 25-38.
- Swenne, D.A. and Thoenes, D., 1985. The eutectic crystallization of sodium chloride dihydrate and ice. Journal of Separation Process Technology, 6: 17-25.

- Ulrich, J., 2004. Is melt crystallization a green technology? *Crystal Growth and Design*, 4(5): 879-880.
- Vaessen, R.J.C., Janse, B.J.H., Seckler, M.M. and Witkamp, G.J., 2003. Evaluation of the performance of a newly developed eutectic freeze crystallizer: Scraped cooled wall crystallizer. *Chemical Engineering Research and Design*, 81(10): 1363-1372.
- Van Der Ham, F., Witkamp, G.J., De Graauw, J. and Van Rosmalen, G.M., 1999. Eutectic freeze crystallization simultaneous formation and separation of two solid phases. *Journal of Crystal Growth*, 198-199(PART I): 744-748.
- Waly, T., 2011. Minimizing the Use of Chemicals to Control Scaling in SWRO: Improved Prediction of Scaling Potential of Calcium Carbonate, PhD thesis, Delft University of Technology.



Chapter 2

Eutectic Freeze Crystallization of Nickel Sulfate from an Industrial Stream: a Comparison with Evaporative Crystallization

Xiaoqian Lu, Elif Genceli Güner, Jaap van Spronsen, Harald Oosterhof, Geert-Jan Witkamp.

Prepared for submission to Hydrometallurgy.

Abstract

Eutectic freeze crystallization (EFC) was tested at pilot plant scale on an industrial nickel sulfate stream. The heat transfer rate over the heat exchangers inside the crystallizer could be maintained at 9 kWm⁻². The ice and NiSO₄·7H₂O (morenosite) production rate was 16 and 4 kg/h respectively. Filtration and washing of the ice and nickel sulfate crystals led to a high degree of purification. The ice crystals with a spherical shape and an average size of 0.3 mm are sufficiently pure to be recycled into the process. The nickel sulfate crystals are bar-shaped with an average size of 0.5×0.05 mm. After washing the nickel sulfate crystal lattice contains magnesium as the major impurity (300 mg/kg). Sodium (6000 mg/kg in the mother liquor) and other minor impurities were removed to below the mg/kg level. The quaternary point of the Na₂SO₄/NiSO₄/H₂O system was determined at -4.8 °C and a composition in solution of 5.2 wt % Na₂SO₄ and 21.3 wt% NiSO₄. The phase diagram shows that with EFC, as compared to evaporative crystallization, 70% more nickel sulfate can be crystallized from solution before the solution is saturated with sodium sulfate.

2.1 Introduction

The metallurgical and hydrometallurgical industries face many challenges today. The most important ones are an increasing demand for metals and metal containing products due to increasing global wealth and population. High quality ores are being depleted and lower purity ores have to be processed. Also environmental regulations become stricter worldwide. These challenges have to be met by continuous improvement of existing processes and by the development of new, better purification and recycling technologies. A typical example is nickel sulfate. The main applications of nickel sulfate are in nickel plating, in catalyst production and in the production of nickel containing batteries. These applications require a highly pure nickel sulfate otherwise inferior products will result (Table 2.1).

Table 2.1 Impurity distribution in crude nickel sulfate from copper production and in commercially available nickel sulfate. Specifications of nickel sulfate for electroplating and catalyst production (Danish Environmental Protection Agency, 2008).

| NiSO ₄ | Crude | Electroplating | Catalysts | Commercial |
|-------------------|-------------------|-------------------|-------------------|-------------------|
| Element | assay in mg/kg | Spec. in mg/kg | Spec. in mg/kg | assay in mg/kg |
| Co | 50-100 | 5000 | 1000 | <100 |
| Zn | 2500-5000 | 30 | 200 | <10 |
| Fe | 1000-2000 | 20 | 40 | <5 |
| Cu | 1700-6000 | 20 | 40 | <5 |
| Pb | 140-460 | 10 | 40 | <5 |
| Cd | 50-125 | 10 | 20 | <4 |
| As | 1500-3000 | 10 | 20 | <1 |

Nickel sulfate is produced in a variety of ways from nickel ore, from copper ore as a side product and from recycling products containing nickel. The last step in the purification process of nickel sulfate is evaporative crystallization of a nickel sulfate solution. An alternative for evaporative crystallization that can possibly contribute to meet the challenges of today is eutectic freeze crystallization (EFC). EFC is a new technology that separates ice and salt from a salt solution in water by cooling crystallization. The workings of EFC can be explained with the binary phase

diagram of salt and water depicted in **Figure 2.1**.

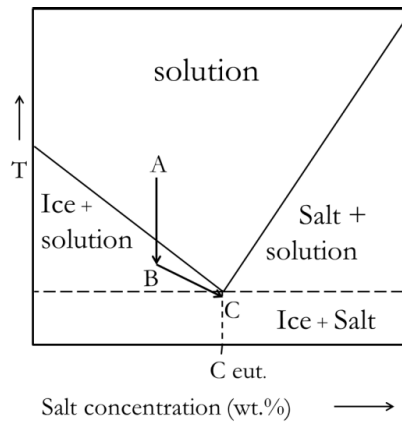


Figure 2.1 Typical binary phase diagram for salt/water with a batch EFC trajectory (A->B->C).

A dilute salt solution at point A is cooled. As the temperature crosses the phase line (the ice line) in the phase diagram at point B ice will start crystallizing. The crystallization of ice will cause an increasing salt concentration in solution and the temperature keeps decreasing due to melting point depression. Upon reaching the temperature at point C the solution is saturated with salt and salt will also start crystallizing. Upon further cooling both ice and salt will crystallize and the temperature of the solution will remain constant because the salt concentration in the solution remains constant. This point in the phase diagram is called the eutectic point. Due to density differences, ice will float to the top and salt will sink to the bottom and can be easily separated. During continuous operation the temperature in the crystallizer will remain constant at the eutectic temperature. The effect of impurities in solution is a lower eutectic point due to melting point depression.

The advantages of EFC over evaporative crystallization can be many. The energy consumption of ice crystallization in EFC is 7 times less compared to evaporation of the same amount of water in single stage evaporative crystallization (van der Ham et al., 1998). Local high super saturation at the evaporation point is avoided. This has a positive effect upon crystal purity and particle size distribution. With EFC there are no temperature differences inside the crystallizer except on the

surface of the heat exchangers. Possible hot spots are cooled down by melting of ice and dissolution of salt. Cold spots are immediately taken away by crystallization of salt and ice. This results in a very controlled crystallization process and an improved product quality. Also scaling can be less severe. Because EFC operates at a lower temperature corrosion is less. New and different separations are possible because EFC is performed at another part of the phase diagram.

EFC can be performed with direct cooling (Stepakoff, GL et al., 1974) with the risk of contamination of the environment with refrigerants like CFC's or hydrocarbons as a major disadvantage. For indirect cooling, crystallizers with scraped heat exchangers were developed (van der Ham et al., 1998). Applications that were investigated so far are the recovery of NaCl from brines (Svenne and Thoenes, 1985), the crystallization of CuSO_4 and NaNO_3 (van der Ham, 1999; van der Ham et al., 1998), MgSO_4 (Genceli et al., 2005; Himawan et al., 2006), and the recovery of soda from an industrial waste stream (Pascual et al., 2008).

Aim of this investigation is to test if EFC can be performed with an industrial nickel sulfate solution and to find out if there are advantages compared to evaporative crystallization. Starting point for the investigation is a nickel sulfate bleed stream from the evaporator that has to be recycled back into the process in order to remove trace impurities (**Figure 2.2**).

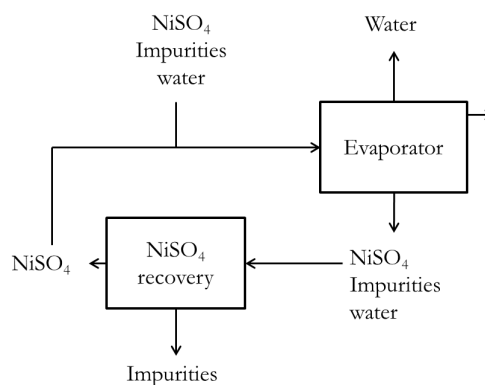


Figure 2.2 Production of nickel sulfate by evaporative crystallization.

First, batch EFC experiments with a nickel sulfate bleed stream from the evaporator were run at lab scale. In the next phase a continuous EFC experiment was performed in a pilot plant equipped with a 200 liter scraped cooled wall crystallizer.

2.2 Materials and Methods

2.2.1 Materials

Nickel sulfate p.a. and sodium sulfate p.a. were obtained from Sigma Aldrich.

The industrial nickel sulfate solution contains 26 wt% NiSO_4 and 0.7 wt% total impurities. The trace element composition is presented in **Table 2.2**.

Table 2.2 Composition of the industrial nickel sulfate solution (mg/kg).

| Element | Ni | SO_4 | Na | Cl | Mg | K | Ca | B | Sr |
|---------|-------|---------------|------|-----|-----|-----|----|----|----|
| Content | 98000 | 183000 | 6250 | 360 | 223 | 103 | 34 | 20 | 9 |

2.2.2 Set-up batch experiments

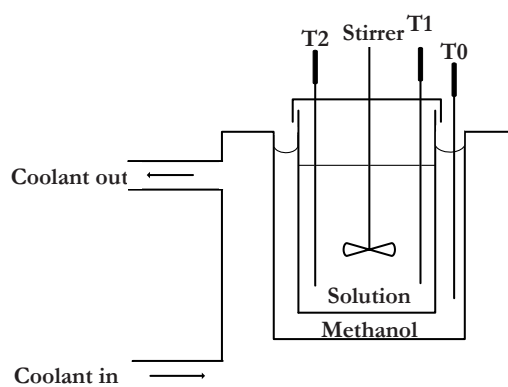


Figure 2.3 Batch set-up.

The batch crystallization experiments were performed in a clear plastic beaker with a volume of 1 liter equipped with a mechanical stirrer (**Figure 2.3**). The crystallizer was placed inside a double walled vessel and was cooled indirectly with methanol between the crystallizer and the double walled vessel. The methanol was cooled indirectly with a cooling machine from Tamson Instruments B.V., having 10 kW cooling capacity at 0 °C and a temperature accuracy of 0.05 °C. The temperature was measured with three PT-100 sensors connected to an ASL F250 precision thermometer switchbox with an accuracy of 0.01 °C. Two sensors measured the temperature inside the crystallizer at different locations, while the third sensor measured the temperature of the methanol.

2.2.3 Experimental procedure batch experiments

The crystallizer was filled with 1 liter of an industrial nickel sulfate solution. The agitator was started at 200 rpm. Cooling was started with a temperature set point of -9 °C, approximately 5 °C below the eutectic point of pure nickel sulfate solution. After crystallization of ice and salt had occurred the agitation was stopped. The salt crystals were allowed to settle at the bottom of the crystallizer and the ice crystals were allowed to float to the top. Salt and ice were isolated separately by vacuum filtration over a glass filter. The ice crystals were washed with pure water of 0 °C with a mass ratio of 1:1 between the washing liquid and the wet crystals on the filter. The salt crystals were washed with saturated pure saturated nickel sulfate solution (prepared from p.a. nickel sulfate) with a mass ratio of 1:1 between the washing liquid and the wet crystals on the filter. All actions were performed in a cold room at -3 °C in order to prevent melting of ice and dissolution of salt. The crystallization process was followed by studying samples from the crystallizer under the microscope. All process streams were sampled and analyzed.

2.2.4 Experimental procedure evaporative crystallization

500 milliliter of the industrial nickel sulfate solution was added to a 1 liter one-necked round-bottom flask. At 80 °C under reduced pressure the solution was concentrated with a laboratory rotary evaporator (Laborota 4002-control from Heidolph). After crystallization of

nickel sulfate the evaporation process was stopped and the nickel sulfate crystals were isolated by vacuum filtration over a glass filter. The nickel sulfate crystals were washed with pure saturated nickel sulfate solution.

2.2.5 Determination of the $\text{NiSO}_4/\text{Na}_2\text{SO}_4/\text{H}_2\text{O}$ ternary phase diagram

The quaternary point of the phase diagram was determined as follows. The crystallizer, used for the batch experiments, was filled with 1 litre solution containing 22 wt% nickel sulfate and 10 wt% sodium sulfate. Cooling was started and after crystallization of ice, nickel sulfate and sodium sulphate the temperature of the cooling liquid was increased to 0.05 °C below the temperature of the crystal slurry. When the temperature in the crystallizer was constant for 2 hours a sample was taken from the solution with a syringe equipped with a filter. The composition of the solution was determined by ICP-OES. The crystallization process was visually followed with the microscope. Next the two eutectic solubility lines were determined. First the eutectic point of a pure nickel sulfate solution was measured according to the procedure described for the quaternary point. Second, the sodium sulphate concentration was stepwise increased to determine the next point on the solubility line until the quadruple point was reached. After each addition the system was allowed to equilibrate for two hours before sampling. The same procedure was repeated starting with a pure sodium sulfate solution with the stepwise addition of nickel sulphate.

2.2.6 Pilot Plant set up

The flow sheet of the pilot plant is presented in **Figure 2.4**. The nickel sulfate stream entered a 200 liter buffer tank, from which the solution was pumped into the crystallizer. For all process streams Watson Marlow peristaltic pumps were used. The flow rates of the process streams and of the cooling liquid were measured with an accuracy of ± 0.25 l/h by magnetic flow transmitters manufactured by Rosemount Fisher. The cooling machine with a 10 kW cooling capacity at 0 °C used freezium™ (43% potassium formate in water) as a coolant and was supplied by Tamson Instruments B.V.. The temperature of the cooling liquid was controlled with an accuracy of 0.1 °C. The temperatures of all streams as well as the temperature within the crystallizer and in the separator were measured with an accuracy of ± 0.01 °C by PT-100 sensors connected to an ASL

F250 precision thermometer with a resolution of ± 0.001 °C. The scraped cooled wall crystallizer with a volume of 200 liter contained two heat exchanger modules stacked on top of each other (Pascual et al., 2010). One module consisted of two vertical concentric cylinders that were scraped from both sides. The heat exchangers total surface area was 0.76 m². The separator had a volume of 120 liter. The belt filters for the salt and the ice with a surface area of 0.75 and 2.25 m² respectively were supplied by Larox-Pannevis (Utrecht, Netherlands). In order to prevent cold losses into the environment all equipment was well isolated. For automatic data acquisition a Labview system was used.

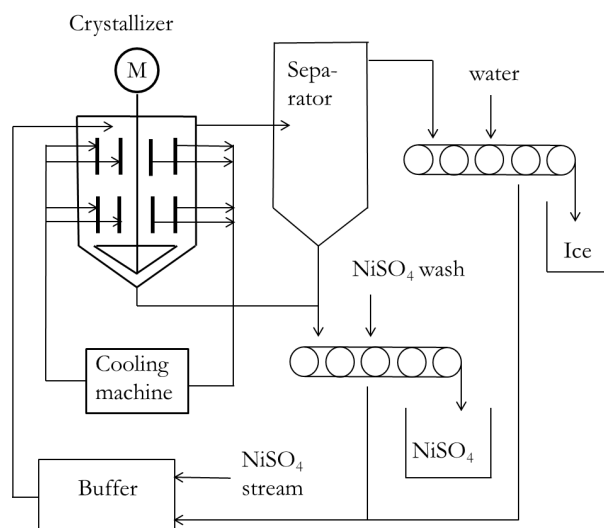


Figure 2.4 Flow sheet of the pilot plant.

2.2.7 Experimental procedure pilot plant experiments

Under continuous operation the buffer tank was fed with the nickel sulfate stream, with the recycled filtrate and the wash liquors from the belt filters. The slurry in the crystallizer was cooled by the heat flux through the vertical heat exchangers.

The overflow of the crystallizer consisted of ice slurry with minor amounts of the salt and was pumped to the separator. The overflow of the separator consisting of ice slurry was pumped to

the ice belt filter. On the belt filter the ice was filtered and washed with pure water of 0 °C. The bottom flow of the crystallizer consisted of nickel sulfate slurry was combined with the bottom flow from the separator and pumped to the salt belt filter. On this filter nickel sulfate was filtered and washed with saturated nickel sulphate solution. Samples were taken from all process streams.

2.2.8 Analysis

Nickel and trace element composition of the ice, salt and liquid samples was determined with ICP-OES (Inductive Couples Plasma Optical Emission Spectrometry with the type of SPECTRO ARCOS EOP) with an accuracy of 3 %. Photographs of salt and ice crystals were taken under a Nikon TMS microscope equipped with a Nikon D700 camera. Nickel sulfate samples were analyzed by X-Ray Diffraction (XRD) using a D8 ADVANCE powder diffractometer from Bruker AXS Inc. with an accuracy of $\pm 0.01^\circ$ for 2θ over the whole angular range.

2.3 Results and Discussion

2.3.1 Batch EFC experiments

The composition of the industrial nickel sulfate stream (**Table 2.2**) used for the batch experiment shows that it still is a fairly pure stream when compared to the crude nickel sulfate stream in the introduction (**Table 2.1**). The major impurities are sodium (6000 mg/kg) followed by chlorine (360 mg/kg) magnesium (223 mg/kg) and potassium (103 mg/kg). The nickel sulfate concentration is 26 wt% and from the phase diagram (**Figure 2.5**, (Linke and Seidell, 1965)) it follows that upon cooling first nickel sulfate is expected to crystallize.

Indeed in our batch EFC experiments with the industrial solution this was the case. After 70 minutes of cooling the temperature had reached -1.4 °C. Because at this point the solution was supersaturated in nickel sulfate, nucleation of nickel sulfate occurred. The temperature inside the crystallizer as a function of time for the batch experiment is presented in **Figure 2.6**.

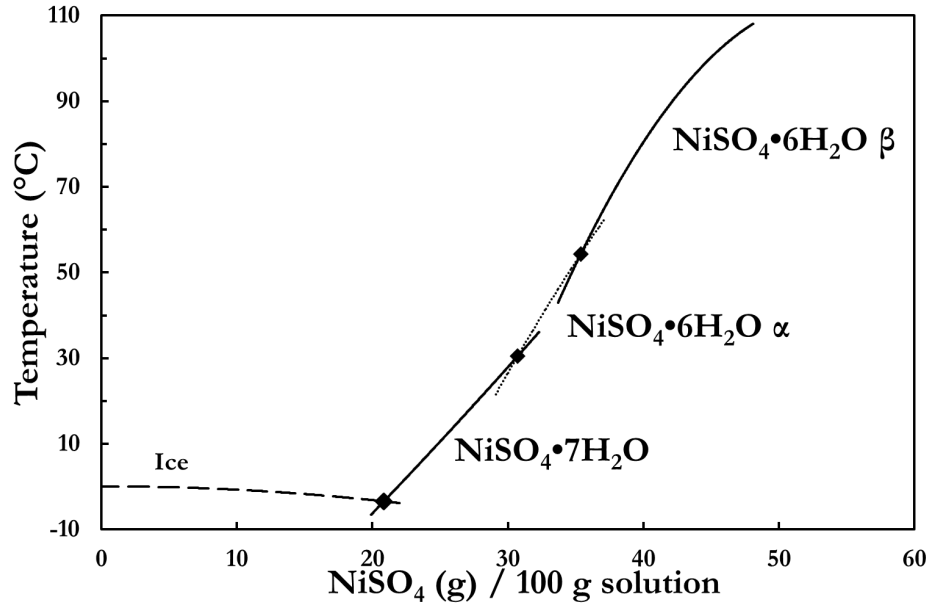


Figure 2.5 Binary phase diagram of nickel sulfate/water (Rohmer, 1939).

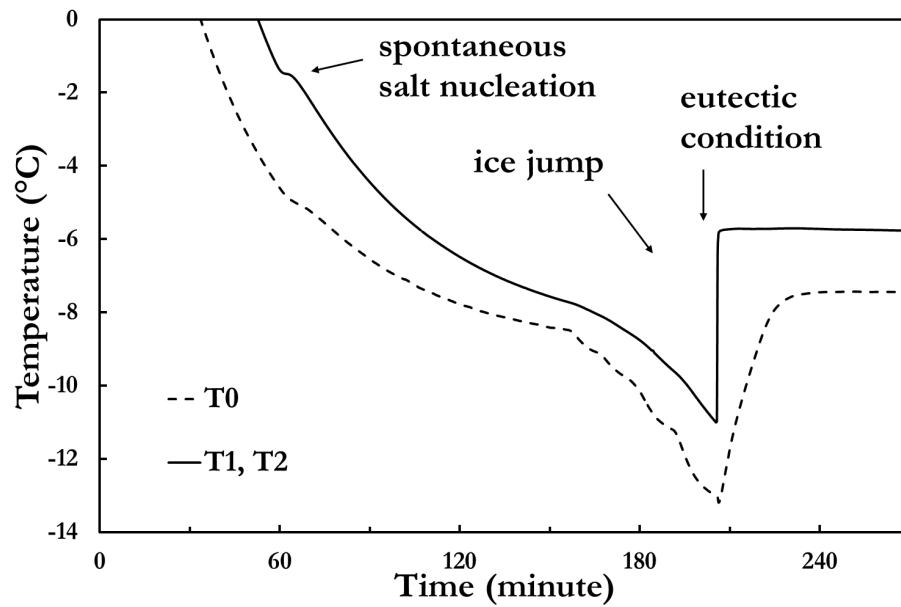


Figure 2.6 Temperature as a function of time in a batch EFC process for nickel sulfate solution (T₁, T₂: temperature inside the crystallizer, T₀: temperature of the coolant).

From the figure it can be seen that at the point of nickel sulfate nucleation, the temperature inside the crystallizer increased temporarily due to the released heat of crystallization. Upon further cooling the temperature decreased again and the amount of nickel sulfate crystals increased. After 3 hours and 25 minutes the temperature had decreased to $-10.5\text{ }^{\circ}\text{C}$ and the solution was highly supersaturated in ice. Ice nucleation occurred and the temperature increased from $-10.5\text{ }^{\circ}\text{C}$ to $-5.5\text{ }^{\circ}\text{C}$ due to the released heat of crystallization. Upon further cooling ice and nickel sulfate kept crystallizing simultaneously at the eutectic point and the temperature decreased very slowly due to the increasing concentration of impurities. The crystallization process was followed by sampling and taking pictures of the crystals under the microscope (**Figure 2.7**). The nickel sulfate crystals are bar-shaped with a size of approximately $0.5\times 0.05\text{ mm}$. The ice crystals are roughly spherical with a size of 0.15 mm .

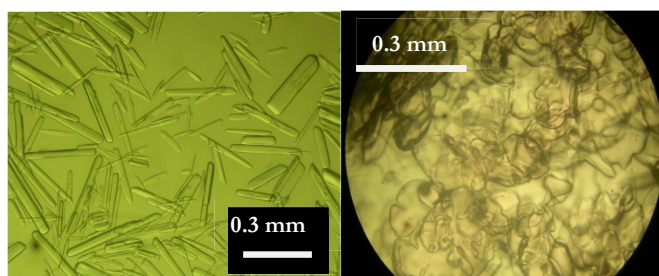


Figure 2.7 Pictures of Nickel sulfate crystals (left) and ice crystals (right).



Figure 2.8 Floating Ice and settled nickel sulfate inside the crystallizer.

***Eutectic Freeze Crystallization of Nickel Sulfate from an Industrial Stream: a Comparison with
Evaporative Crystallization***

After 2 hours of batch operation at eutectic conditions, around 30 % of the crystallizer volume was visually observed to be filled with ice and salt crystals. The agitator and cooling were stopped and ice and salt crystals were allowed to separate by gravitation (**Figure 2.8**).

The ice slurry was decanted from the crystal slurry, filtrated and washed 2 times with 0 °C water. **Table 2.3** presents the analytical data (ICP-OES) with respect to the washing of the ice. From this table it follows that after two washing steps 90% of the impurities are washed from the ice. It is expected that further washing will remove most of the remaining impurities because ice crystallization is very selective with respect to impurity uptake (Gross and Svec, 1997).

Table 2.3 Impurity distribution between the solution and the ice crystals and the effect of washing of the ice crystals with water at 0 °C.

| | Ni | SO ₄ | Na | Cl | Mg | K | Ca | B | Sr |
|-----------------------------------|------|-----------------|-------|-----|-----|-----|----|----|------|
| | wt% | | mg/kg | | | | | | |
| Start solution | 10.1 | 17.4 | 6257 | 338 | 225 | 109 | 30 | 16 | 9 |
| Ice unwashed | 2.3 | 4.0 | 1001 | 226 | 52 | 13 | 4 | 6 | 2 |
| Mother liquor | 8.3 | 15.0 | 6175 | 398 | 225 | 103 | 46 | 22 | 11 |
| Ice after 1 st wash | 0.7 | 1.1 | 246 | 150 | 15 | <4 | <1 | 3 | 0.5 |
| Ice after 2 nd wash | 0.2 | 0.4 | 80 | <40 | 6 | <4 | <1 | <1 | <0.1 |

The salt crystal slurry was filtered and washed 3 times with saturated nickel sulfate solution of 20 °C. According to the phase diagram, morenosite, NiSO₄·7H₂O is the stable crystal structure under eutectic conditions. This was confirmed by XRD. **Table 2.4** presents the analytical results (ICP-OES) with respect to the washing of the salt. This table shows that after three washing steps Na, K, Cl, Sr, and Ca were washed from the surface of the crystals and that these elements are not taken up in the crystal lattice above the mg/kg level. The very low Na content of the crystals indicates that inclusions are almost nonexistent (<0.1 wt%). The only impurity that is taken up in the crystal lattice above the mg/kg level is Mg with a level of 300 mg/kg. The high uptake can be explained by the similar ionic radius and charge of Mg²⁺ and Ni²⁺. Furthermore MgSO₄·7H₂O and NiSO₄·7H₂O have almost identical unit cell dimensions. This leads to an excellent fit of Mg

into the nickel sulfate lattice.

Table 2.4 Impurity distribution between the solution and the nickel sulfate crystals and the effect of washing of the salt crystals.

| | Ni | SO ₄ | Na | Cl | Mg | K | Ca | B | Sr |
|----------------------------|------|-----------------|-------|-----|-----|-----|----|----|------|
| | wt% | | mg/kg | | | | | | |
| Start solution | 10.1 | 17.4 | 6257 | 338 | 225 | 109 | 30 | 16 | 9 |
| Crystals after fil. | 16.6 | 25.5 | 2558 | 143 | 309 | 43 | 8 | 10 | 3 |
| Mother liquor | 8.3 | 15.2 | 6287 | 404 | 226 | 106 | 58 | 19 | 10 |
| Crystals | | | | | | | | | |
| After 1 st wash | 19.0 | 27.7 | <5 | <40 | 294 | 34 | 4 | 8 | 1 |
| After 2 nd wash | 18.2 | 26.7 | <5 | <40 | 297 | 39 | 3 | 9 | 1 |
| After 3 rd wash | 20.7 | 29.4 | <5 | <40 | 275 | <4 | <1 | 7 | <0.1 |
| Washing liquid | 11.0 | 15.9 | 5 | <40 | 3 | <4 | <1 | 4 | <0.1 |

From this batch experiment it was concluded that nickel sulfate can be isolated from a nickel sulfate solution in by EFC. The above mg/kg level impurities like Na, K, Ca and Cl in the industrial bleed stream did not end up in the product but remained in the mother liquor except for Mg. Mg partitioned between the solution and the crystals.

2.3.2 The Na₂SO₄/NiSO₄/H₂O phase diagram

As the industrial stream is concentrated by EFC or evaporative crystallization the sodium content in solution will increase. At a certain moment in time the sodium sulfate concentration will reach the saturation level and in the case of evaporative crystallization Na₂SO₄·NiSO₄·4H₂O will co-crystallize from solution (Soboleva, 2007). In the case of EFC Na₂SO₄·10H₂O will start co-crystallizing with the nickel sulfate. In both cases this will lead to an unsuitable product contaminated with sodium sulfate which has to be prevented. The information needed to be able to prevent contamination of the product with sodium sulfate is the relevant part of the nickel sulfate/sodium sulfate/water phase diagram as presented in **Table 2.5** (Linke and Seidell, 1965).

*Eutectic Freeze Crystallization of Nickel Sulfate from an Industrial Stream: a Comparison with
Evaporative Crystallization*

Table 2.5 Points in the nickel sulfate/sodium sulfate/water phase diagram.

| T °C | NiSO ₄ % | Na ₂ SO ₄ % | solid phase |
|---------|------------------------|--------------------------------------|---|
| 0 | 17 | 7.6 | NiSO ₄ ·7H ₂ O ; Na ₂ SO ₄ ·10H ₂ O |
| 10 | 19 | 11 | NiSO ₄ ·7H ₂ O ; Na ₂ SO ₄ ·10H ₂ O |
| 75 | 37 | 4.6 | NiSO ₄ ·6H ₂ O ; NiNa ₂ (SO ₄) ₂ ·4H ₂ O |
| 75 | 38 | 3.5 | NiSO ₄ ·6H ₂ O |
| 97 | 42 | 3.4 | NiSO ₄ ·6H ₂ O ; NiNa ₂ (SO ₄) ₂ ·4H ₂ O |
| 97 | 43 | 3.1 | NiSO ₄ ·6H ₂ O |

What is missing in these data is the phase behavior around the quaternary point. In order to get an impression of the situation around the quaternary point the two eutectic solubility lines and the quaternary point were experimentally determined (**Table 2.6, Figure 2.9**).

In the ternary phase diagram the two eutectic solubility lines projected along the temperature axis represent the conditions where two solid phases are in equilibrium with the solution. One line represents the situation where solid nickel sulfate and ice are in equilibrium with nickel sulfate solution containing a varying amount of dissolved sodium sulfate. For the other line solid sodium sulfate and ice are in equilibrium with sodium sulfate solution containing a varying amount of dissolved nickel sulfate. The two eutectic phase lines meet in the quadruple point at -4.78 °C.

The composition at the quadruple point is 5 wt% sodium sulfate and 21 wt% nickel sulfate. So in order to prevent contamination of the product with sodium sulfate in an EFC process, the sodium sulfate concentration in solution should be kept below 5 wt%. **Table 2.5** shows that for an evaporative crystallization process at 97 °C the sodium sulfate concentration should be kept below 3 wt% in order to prevent contamination of the product with the double salt. The nickel sulfate concentration is at this point 43 wt%. So a stream containing 3 wt% sodium sulfate and 43 wt% nickel sulfate is unsuitable for evaporative crystallization at 97 °C but can still be used in an EFC process. Recovery of about 70 % of the nickel sulfate from this solution by EFC is still possible before the sodium sulfate concentration in solution reaches 5 wt% and starts co-crystallizing with the nickel sulfate.

Table 2.6 Determination of the two eutectic solubility lines and the quaternary point of the system $\text{NiSO}_4/\text{Na}_2\text{SO}_4/\text{H}_2\text{O}$.

| Crystals present in solution | T (°C) | Na_2SO_4 (wt%) | NiSO_4 (wt%) | H_2O (wt%) |
|---|-----------|-----------------------------------|--------------------------|-------------------------------|
| Ice | -3.7 | 0.02 | 24.7 | 75.3 |
| + | -4.02 | 1.2 | 22.4 | 76.4 |
| $\text{NiSO}_4 \cdot 7\text{H}_2\text{O}$ | -4.2 | 2.8 | 22.4 | 74.8 |
| | -4.45 | 4.1 | 21.3 | 74.6 |
| Ice + $\text{NiSO}_4 \cdot 7\text{H}_2\text{O}$ | -4.77 | 5.2 | 21.3 | 73.5 |
| + $\text{Na}_2\text{SO}_4 \cdot 10\text{H}_2\text{O}$ | -4.78 | 5.1 | 21.6 | 73.3 |
| Ice | -4.2 | 5.3 | 20.4 | 74.3 |
| + | -3.08 | 5.7 | 14.6 | 79.7 |
| $\text{Na}_2\text{SO}_4 \cdot 10\text{H}_2\text{O}$ | -2.08 | 5.9 | 8.0 | 86.1 |
| | -1.14 | 6.1 | 0.04 | 93.9 |

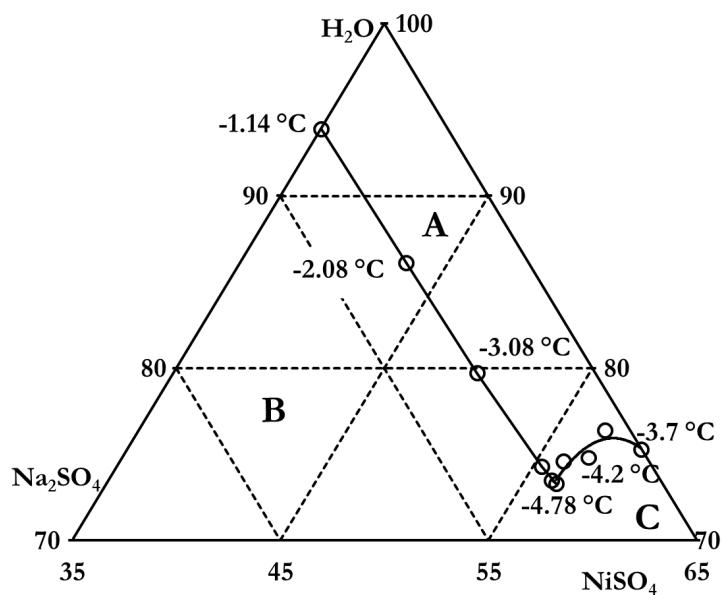


Figure 2.9 Projected ternary phase diagram of nickel sulfate, sodium sulfate and water with two eutectic solubility lines. Phase A: solution; Phase B: sodium sulfate/ice/solution; Phase C: nickel sulfate/ice/solution.

2.3.3 Evaporative crystallization

In order to compare EFC and evaporative crystallization with respect to the nickel sulfate quality, part of the industrial nickel sulfate solution was crystallized by evaporation. The experiment was performed at 80 °C in a laboratory rotary evaporator. The analytical results are depicted in **Table 2.7**. The table shows that the $\text{NiSO}_4 \cdot 6\text{H}_2\text{O}$ crystals still contain a high amount of sodium after washing. According to the phase diagram (**Table 2.5**) it is expected that the nickel sulfate is contaminated with the double salt. The magnesium content of the nickel sulfate from the evaporator is comparable to that from EFC.

Table 2.7 Impurity distribution in evaporative crystallization of $\text{NiSO}_4 \cdot 6\text{H}_2\text{O}$.

| | Na | Mg | K | Sr |
|--|-------|-----|-----|----|
| | mg/kg | | | |
| Start solution | 6520 | 225 | 111 | 8 |
| $\text{NiSO}_4 \cdot 6\text{H}_2\text{O}$ before washing | 2640 | 401 | 50 | 4 |
| $\text{NiSO}_4 \cdot 6\text{H}_2\text{O}$ after washing | 1280 | 319 | <1 | 2 |
| EFC: $\text{NiSO}_4 \cdot 7\text{H}_2\text{O}$ | <5 | 300 | <4 | 1 |
| Commercial $\text{NiSO}_4 \cdot 6\text{H}_2\text{O}$ | 239 | 259 | 18 | 2 |

2.3.4 Continuous EFC of nickel sulfate at pilot plant scale

In order to determine the effect of scaling up and the effect of continuous crystallization, EFC experiments were performed in a mobile pilot plant at a production location for nickel sulfate. The EFC process was started by filling up the crystallizer with nickel sulfate solution followed by starting up the cooling. The composition of the feed solution (**Table 2.9**) indicates that the nickel sulfate concentration is close to the concentration at the eutectic point. First ice started crystallizing at -6 °C and upon further cooling at -6.5 °C nickel sulfate started crystallizing and the temperature increased to -5.0 °C. After nucleation of nickel sulfate the feed to the crystallizer was started at 200 l/h and continuous operation began. The residence time of the feed solution in the crystallizer was 1 hour and the average production rate was 16 kg/h for ice and 4 kg/h for nickel sulfate. The operating conditions during continuous nickel sulfate production are given in **Table 2.8**.

Table 2.8 Experimental operating conditions.

| Crystallizer (200 liter) | | | Separator (120 liter) | | |
|----------------------------|------|-------------------------------|--------------------------|------|-------------------------------|
| Flow from the buffer | 200 | $\text{l}\cdot\text{h}^{-1}$ | Flow from crystallizer | 150 | $\text{l}\cdot\text{h}^{-1}$ |
| Temperature inside | -5.5 | $^{\circ}\text{C}$ | Bottom flow to salt belt | | |
| Temperature cooling liq. | -14 | $^{\circ}\text{C}$ | Filter | 60 | $\text{l}\cdot\text{h}^{-1}$ |
| Heat transfer rate | 9 | $\text{kW}\cdot\text{m}^{-2}$ | | | |
| Bottom flow to salt filter | 50 | $\text{l}\cdot\text{h}^{-1}$ | Overflow to ice belt | | |
| Overflow to separator | 150 | $\text{l}\cdot\text{h}^{-1}$ | Filter | 90 | $\text{l}\cdot\text{h}^{-1}$ |
| Residence time | 60 | min. | Temperature | -5.5 | $^{\circ}\text{C}$ |
| Ice production rate | 16 | $\text{kg}\cdot\text{h}^{-1}$ | Residence time | 48 | min. |
| Salt production rate | 4 | $\text{kg}\cdot\text{h}^{-1}$ | | | |
| Process in: | | | Process out: | | |
| Nickel sulfate solution | 14 | $\text{kg}\cdot\text{h}^{-1}$ | Ice from belt filter | 16 | $\text{kg}\cdot\text{h}^{-1}$ |
| Ice wash water | 1.6 | $\text{kg}\cdot\text{h}^{-1}$ | Salt from belt filter | 4 | $\text{kg}\cdot\text{h}^{-1}$ |
| Salt wash liquid | 0.4 | $\text{kg}\cdot\text{h}^{-1}$ | | | |
| Overall: | | | | | |
| Run time | 300 | min. | | | |
| Nickel sulfate produced | 20 | kg | | | |
| Ice produced | 80 | kg | | | |

The shape of the nickel sulfate crystals and the ice crystals after 5 residence times is comparable with those of the batch experiments. The nickel sulfate crystals are bar-shaped with a size of approximately 0.6×0.06 mm. The ice crystals are roughly spherical with a size of 0.3 mm. The nickel sulfate and ice crystals were filtered and washed on a belt filter. **Figure 2.10** depicts the nickel sulfate and unwashed ice crystals as they drop from the belt filter.



Figure 2.10 Nickel sulfate (left) and ice (right) on the belt filter.

The purity of the nickel sulfate (**Table 2.9**) is comparable to that from the batch process. The commercial nickel sulfate used for the preparation of the washing solution contains 239 mg/kg

***Eutectic Freeze Crystallization of Nickel Sulfate from an Industrial Stream: a Comparison with
Evaporative Crystallization***

sodium, while 17 mg/kg the sodium content of the nickel sulfate from the EFC process is much lower. The higher sodium content of the commercial nickel sulfate can be explained by less effective washing or the presence of the double salt that will be difficult to remove by washing. The magnesium content of the EFC nickel sulfate depends upon the magnesium concentration in the start solution and cannot be removed by washing, and the same holds true for the magnesium content of commercial nickel sulfate. The higher nickel sulfate content of commercial nickel sulfate can be explained by the fact that commercial nickel sulfate is a 6-hydrate and EFC nickel sulfate is a 7-hydrate. Therefore commercial nickel sulfate contains less water and has higher nickel sulfate content than the EFC nickel sulfate.

When EFC is compared with the current evaporative crystallization process for nickel sulfate there are various process improvements possible. First, replacement of evaporative crystallization by EFC may result in cost savings. The cost savings are the result of energy savings and a reduction of the recycle stream. This is challenging, however, because the risk and investment of replacing an existing process by a new process for the same product has to be balanced against the gain. Second, EFC can be used to treat the bleed stream from the crystallizer and thereby increase the production output and decrease the recycle stream. This option looks easier to implement because the risk is fairly small compared to complete replacement of the evaporation plant. An essential step to decrease the risk involved in introducing this new technology is the construction of a larger pilot plant.

Table 2.9 The effect of washing of the nickel sulfate crystals.

| | Ni | SO ₄ | Na | Mg | K | Ca | Si | Sr |
|------------------------------|-----|-----------------|-------|-----|-----|----|----|----|
| | wt% | | mg/kg | | | | | |
| Start solution | 8 | 16 | 4024 | 90 | 174 | 79 | 31 | 10 |
| Crystals after filtration | 21 | 34 | 404 | 172 | 15 | 3 | 2 | <1 |
| Crystals after washing | 22 | 35 | 17 | 173 | 12 | <1 | <1 | <1 |
| Commercial NiSO ₄ | 24 | 39 | 239 | 259 | 18 | <1 | <1 | 2 |

2.4 Conclusions

EFC is a promising new technology that was successfully tested on an industrial nickel sulfate stream. After batch testing at 1 liter scale in the laboratory the process was scaled up in a mobile pilot plant (crystallizer volume 200 liter). The heat transfer rate over the heat exchangers inside the crystallizer could be maintained at 9 kW/m². An ice and nickel sulfate (NiSO₄·7H₂O, morenosite) production rate of 16 and 4 kg/h respectively could be maintained easily. Filtration and washing of the ice and nickel sulfate crystals led to a high degree of purification. The ice crystals are sufficiently pure to be recycled into the plant. After washing the nickel sulfate crystal lattice contains magnesium as the major impurity. The magnesium content clearly depends upon the magnesium concentration in the start solution and cannot be removed by washing; the same can be concluded for the magnesium content of the commercial product.

The major impurity in the starting solution is sodium sulfate. The quaternary point and the two eutectic solubility lines for the Na₂SO₄/NiSO₄/H₂O ternary system were experimentally determined in order to investigate the limitations of the EFC process and to compare EFC with evaporative crystallization. These data show that a stream containing 3 wt% sodium sulfate and 43 wt% nickel sulfate is unsuitable for evaporative crystallization at 97 °C but can still be used in an EFC process. Recovery of about 70 % of the nickel sulfate is still possible before the sodium sulfate concentration in solution reaches 5 wt% and sodium sulfate starts crystalizing together with the nickel sulfate. This clearly shows that because EFC operates at another part of the phase diagram compared to evaporative crystallization an improved separation becomes possible.

Commercially available nickel sulfate is often a 6-hydrate and EFC nickel sulfate is a 7-hydrate. The recrystallization of the 7-hydrate into the 6-hydrate may lead to a purer product and can be investigated.

References

- Danish Environmental Protection Agency, 2008. The Risk Assessment Report on Nickel Sulphate.
- Genceli, F.E., Gärtner, R. and Witkamp, G.J., 2005. Eutectic freeze crystallization in a 2nd generation cooled disk column crystallizer for $\text{MgSO}_4 \cdot \text{H}_2\text{O}$ system. *J Cryst Growth*, 275(1-2): e1369-e1372.
- Gross, G.W. and Svec, R.K., 1997. Effect of ammonium on anion uptake and dielectric relaxation in laboratory-grown ice columns. *J Phys Chem B*, 101(32): 6282-6284.
- Himawan, C., Kramer, H.J.M. and Witkamp, G.J., 2006. Study on the recovery of purified $\text{MgSO}_4 \cdot 7\text{H}_2\text{O}$ crystals from industrial solution by eutectic freezing. *Sep Purif Technol*, 50(2): 240-248.
- Linke, W.F. and Seidell, A., 1965. Solubilities (of) Inorganic and Metal-Organic Compounds: a Compilation of Solubility Data from the Periodical Literature, 1-2. Princeton.
- Pascual, M.R. et al., 2010. A novel scraped cooled wall crystallizer: Recovery of sodium carbonate and ice from an industrial aqueous solution by eutectic freeze crystallization. *Chem Eng Res Des*, 88(9A): 1252-1258.
- Pascual, M.R. et al., 2008. Eutectic freeze crystallization for the recovery of Na_2CO_3 from an industrial solution in a newly developed scraped cooled wall crystallizer. In: M. Roelands (Ed.), 17th International Symposium on Industrial Crystallization. Elsevier, Maastricht, the Netherlands.
- Rohmer, R., 1939. Dehydrating magnesium sulphate in 7 mol/g of water by aqueous means. Intermediary hydrates. *Cr Hebd Acad Sci*, 209: 315-317.
- Soboleva, L.V., 2007. Solubility phase diagrams of $\text{Me}_2\text{SO}_4\text{-NiSO}_4\text{-H}_2\text{O}$ systems and the growth of $\text{Me}_2\text{Ni}(\text{SO}_4)_2 \cdot n\text{H}_2\text{O}$ crystals [Me = Na, Rb, Cs; n = 4, 6]. *Crystallogr. Rep.*, 52(6): 1104-1107.
- Stepakoff, G.L., Siegelman, D., Johnson, R. and Gibson, W., 1974. Development of a eutectic freezing process for brine disposal. *Desalination*, 15(1): 25-38.
- Swenne, D.A. and Thoenes, D., 1985. The eutectic crystallization of $\text{NaCl} \cdot 2\text{H}_2\text{O}$ and ice. *Journal of Separation Process Technology*, 6: 17-25.
- van der Ham, F., 1999. Eutectic Freezey Crystallization, PhD Thesis, Delft Univesity of Technology.
- van der Ham, F., Witkamp, G.J., de Graauw, J. and van Rosmalen, G.M., 1998. Eutectic freeze crystallization: Application to process streams and waste water purification. *Chem Eng Process*, 37(2): 207-213.



Chapter 3

Recrystallization of $\text{NiSO}_4 \cdot 7\text{H}_2\text{O}$ into $\text{NiSO}_4 \cdot 6\text{H}_2\text{O}$

Xiaoqian Lu, Jaap van Spronsen, F.Elif Genceli Güner, Geert-Jan Witkamp. Prepared for submission to Hydrometallurgy with Chapter 2.

Abstract

In order to develop new and improved separation processes for the hydrometallurgical industries recrystallization of $\text{NiSO}_4 \cdot 7\text{H}_2\text{O}$, obtained by eutectic freeze crystallization (EFC) from an industrial NiSO_4 solution, into $\text{NiSO}_4 \cdot 6\text{H}_2\text{O}$ was studied. The recrystallization proved to be a solvent mediated process. The uptake of Mg in the host lattice followed an isomorphous substitution mechanism with a partition coefficient D , which is defined as the concentration ratio of Mg and Ni in the crystal phase divided by the same ratio in the mother liquor, of about 0.5. Most of the impurities in the recrystallization step had a preference to end up in the solid phase and the uptake of most impurities increased with temperature.

3.1 Introduction

The hydrometallurgical industry concerns itself with the production of metals and metal derivatives from ore (Gupta, 2003). After mining, ores containing the required metal are leached with a specific solvent. In the leaching process also a wide range of other metals and impurities are removed from the ore. The resulting solution that contains the required metal together with the other compounds has to be purified further in order to separate the required metal from the other compounds. A variety of separation techniques are available for this purpose and form the basis of the hydrometallurgical industry. Important separation techniques are solvent extraction, crystallization and chemical treatments like basic precipitation. Continuous development of better and improved separation processes is necessary because high quality ores become depleted and lower quality ores containing more impurities have to be processed. In addition, society demands environmentally friendly processing involving recycling of metals, lower energy use and less pollution. Furthermore process improvement is also aimed at lowering the costs and will result in a higher margin on the product. EFC is a promising new crystallization technique, under development in the laboratory and proven at pilot scale for instance for magnesium sulfate and sodium carbonate (Genceli et al., 2005; Himawan and Witkamp, 2006; Pascual et al., 2010; Pronk et al., 2009; Vaessen et al., 2003; van der Ham, 1999; Van Spronsen et al., 2010). The metal salt product of EFC is usually a higher hydrate crystal form which can easily be recrystallized into a lower hydrate as an additional purification step. The purification of a salt by crystallization is hampered by possible incorporation of impurities into the crystallized product. There are different ways by which impurities can be incorporated into the product. The most important ones are isomorphous substitution, co-precipitation, interstitial incorporation, inclusions and entrapments of the liquid on and between the crystals.

Mother liquor on the surface of the crystals can generally be removed with careful washing. However in some cases, for instance when agglomerates of crystals are formed or when the crystals are leaflet shaped and form stacked packets, this can be very difficult.

Inclusions are formed when a crystal grows around a volume of mother liquor. Since the composition of the liquid inside the crystal is the same as the surrounding liquid the appearance of inclusions can be determined through analysis of trace impurities or when they are large enough, by microscopic inspection of the crystals (in **Figure 3.3** a small inclusion is visible in the NiSO_4 heptahydrate crystal).

Interstitial incorporation is the uptake of foreign ions in open spaces between the ions in the lattice. This means that interstitial incorporation is largely governed by the available empty space within the lattice and more indirectly by the crystallization conditions.

Co-precipitation occurs when next to the required salt a second salt crystallizes because the solubility of the second salt has been exceeded. The second salt may have a common ion with the main product. The two different crystals can be completely separate or can be intergrown together. In the latter case separation of the two crystal phases becomes impossible. An example of co-precipitation in EFC is the crystallization of sodium sulfate decahydrate and nickel sulfate heptahydrate as two separate crystal phases.

Isomorphous substitution is the replacement of an ion in the lattice of the crystal by a foreign ion. The amount of isomorphous substitution can be defined by the partition coefficient D:

$$D = \frac{([I])_{crystal}}{([I])_{mother\ liquor}} \cdot \frac{([H])_{mother\ liquor}}{([H])_{crystal}}$$

Where [I] is the concentration of the foreign ions and [H] is the concentration of the host ions. When $D > 1$ the foreign ions have a preference compared to the substituted host ions to be taken up into the crystal lattice. When $D < 1$ the foreign ions have a preference to remain in solution. The extent of isomorphous substitution is governed by the differences between the foreign ion and the host ion and by the kinetics of the crystallization process. It is clear that if the foreign ion differs in size or has a different charge as the host ion, incorporation of the foreign ion into the crystal lattice becomes more difficult. Other parameters that influence the amount of isomorphous substitution are differences in interaction of the host and foreign ion with other ions and water. These differences are caused by differences in the chemical nature of the host ion and foreign ions like polarizability, coordination preference, and dehydration free energy. For instance when a foreign ion is more strongly associated with the counter ion than the host ion, the partition coefficient can be larger than 1. The partition coefficient is not established at equilibrium conditions, as crystal growth and thereby the crystallization process cannot proceed at equilibrium so the kinetics also need be considered. At low crystal growth rates close to equilibrium the D value will be close to the thermodynamic value. At higher growth rates, foreign ions with a lower affinity for the counter ions ($D < 1$) will become more easily entrapped into the crystal lattice. This effect results in more uptake of foreign ions and a higher value for D. At a higher growth rate, foreign ions with a higher affinity for the counter ions ($D > 1$) have less time available for diffusion to the surface of the crystal and incorporation into the crystal lattice. This effect results in a lower value for D.

Aim of this investigation was to determine the distribution of impurities over the different phases in EFC of $\text{NiSO}_4 \cdot 7\text{H}_2\text{O}$ and in the subsequent recrystallization of $\text{NiSO}_4 \cdot 7\text{H}_2\text{O}$ into $\text{NiSO}_4 \cdot 6\text{H}_2\text{O}$. To obtain a trend for the calculation of the D- values average concentrations of trace impurities in the mother liquor between begin and end have been taken. A more accurate

value for batch experiments would require much more intensive sampling and working out an integral function as in (Witkamp, 1989).

3.2 Materials and methods

3.2.1 Materials

$\text{NiSO}_4 \cdot 7\text{H}_2\text{O}$ crystals were used from the EFC experiment described in Chapter 2 using NiSO_4 industrial solution from Umicore, except for experiment No. 5, where p.a. $\text{NiSO}_4 \cdot 6\text{H}_2\text{O}$ (Baker) was used to prepare $\text{NiSO}_4 \cdot 7\text{H}_2\text{O}$ crystals. Recrystallization and washing liquids were prepared from Baker p.a. $\text{NiSO}_4 \cdot 6\text{H}_2\text{O}$ which contains less than 0.01wt% impurity per element and from pure water of 18.2 M Ω .

3.2.2 Recrystallization Set-up

Recrystallization experiments were carried out in a three-necked round-bottom flask, which was immersed into an oil bath (Figure 3.1). The oil bath was placed on a hot plate from IKA WERKE equipped with a temperature sensor with an accuracy of 0.1 °C. The left-neck of the flask was connected to a short open bent tube to equilibrate pressure with the outside while limiting evaporation. A mechanical stirrer was inserted through the middle-neck. A PT-100 temperature sensor connecting to an ASL F250 precision thermometer with an accuracy of 0.01 °C was inserted through the right-neck of the flask.

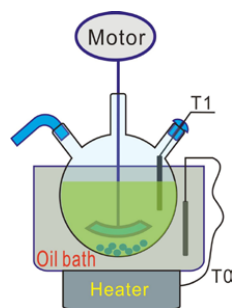


Figure 3.1 Schematic drawing of the experimental set-ups for recrystallization.

3.2.3 Analysis

The composition of the solid and liquid samples was determined with Inductively Coupled Plasma Optical Emission Spectrometry (ICP-OES) (Spectro). Impurities below the ppm level (mg/kg) were determined with high resolution inductively coupled plasma mass spectrometry (hrICP-MS)

(Thermo Instruments/Finnigan Element 2). The procedures, calibration, blank measurements are treated in Chapter 4. Pictures of $\text{NiSO}_4 \cdot 7\text{H}_2\text{O}$ salt and ice crystals were taken under a Nikon TMS microscope with a Nikon D700 camera attached. Samples of the recrystallized $\text{NiSO}_4 \cdot 6\text{H}_2\text{O}$ salt crystals were analyzed by JSM-5400 Scanning Electron Microscopy from Jeol Ltd. After EFC and recrystallization, crystal samples were analyzed by X-Ray Diffraction (XRD) using a D8 ADVANCE powder diffractometer from Bruker AXS Inc. with an accuracy of $\pm 0.01^\circ$ for 2θ over the whole angular range.

3.2.4 Recrystallization experiments at different temperatures

Recrystallization experiments were performed at 40 °C, 50 °C, 60 °C, 70 °C, 80 °C and 90 °C. A saturated solution of NiSO_4 was prepared by adding excess p.a. NiSO_4 to pure water in a 1 liter Erlenmeyer flask equipped with a magnetic stirrer. The resulting slurry was stirred for 2 hours at the required temperature for the recrystallization experiment. The stirrer of the recrystallization vessel was started and the temperature of the heating bath was regulated at the temperature for recrystallization. The saturated NiSO_4 solution was carefully decanted into the recrystallization vessel keeping undissolved NiSO_4 crystals in the Erlenmeyer flask and keeping the recrystallization vessel at the required temperature. Next, NiSO_4 7-hydrate crystals from the EFC experiment were added to the recrystallization vessel. After stirring overnight at the required temperature the NiSO_4 crystals were filtered over a glass filter and washed three times with saturated p.a. NiSO_4 solution.

3.2.5 Recrystallization experiments with reuse of mother liquor

The mother liquor of the recrystallization experiment at 50°C was added to the recrystallization vessel keeping the temperature at 50°C in order to prevent crystallization of NiSO_4 . Next about 100 to 200 grams of NiSO_4 7-hydrate crystals were added to the recrystallization vessel. After stirring 48 hours at 50 °C the NiSO_4 crystals were filtered over a glass filter and washed three times with saturated p.a. NiSO_4 solution. The mother liquor was used again in a recrystallization experiment at 50 °C. This process was repeated 4 times. In the final experiment p.a. $\text{NiSO}_4 \cdot 7\text{H}_2\text{O}$ salt obtained by EFC from p.a. $\text{NiSO}_4 \cdot 6\text{H}_2\text{O}$ (Baker) was added to the five times recycled recrystallization liquid.

3.3 Results and discussion

3.3.1 Recrystallization of $\text{NiSO}_4 \cdot 7\text{H}_2\text{O}$ at different temperatures and times

The binary phase diagram of nickel sulfate and water (Figure 3.2) shows that the transition point of $\text{NiSO}_4 \cdot 7\text{H}_2\text{O}$ into $\text{NiSO}_4 \cdot 6\text{H}_2\text{O}$ occurs around 30 °C.

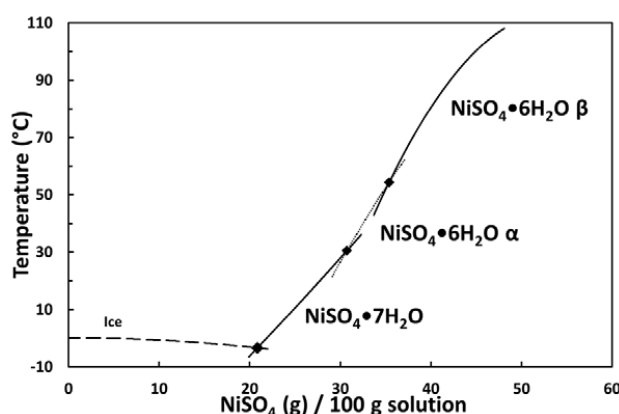
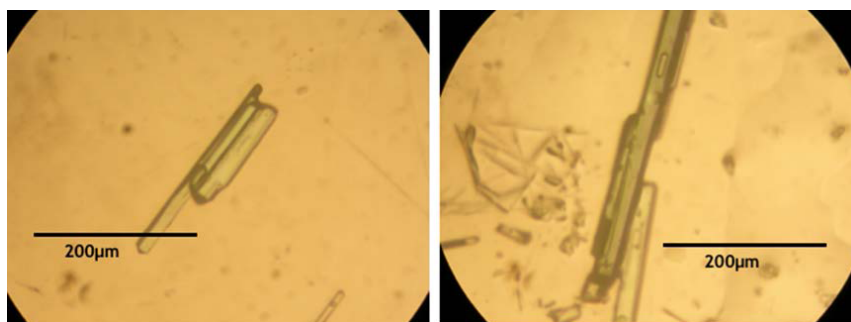
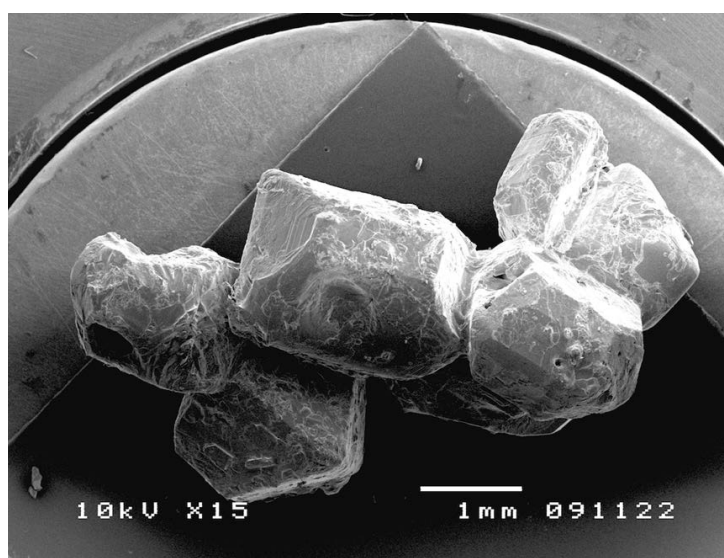


Figure 3.2 Binary phase diagram of nickel sulfate/water (Rohmer, 1939).

In order to create enough driving force, the recrystallization experiments were performed at least 10 °C above the transition point (at 40 °C, 50 °C, 60 °C, 70 °C, 80 °C and 90 °C). The recrystallization process was followed by taking samples and studying the crystals under the microscope. The starting material for the experiments consisted of elongated $\text{NiSO}_4 \cdot 7\text{H}_2\text{O}$ crystals of typically 300 micron (Figure 3.3). Figure 3.4 shows the crystals from a recrystallization experiment at 50 °C. The product crystals have the regular shape of a tetragonal polymorph (Fron del and Palache, 1949) as expected for $\text{NiSO}_4 \cdot 6\text{H}_2\text{O}$. Based upon the totally altered shape of the newly formed crystals it was concluded that the recrystallization was solvent mediated. Another confirmation for this conclusion is that there is at least one impurity (i.e. Mg^{2+} ; Table 3.1) which was redistributed over the mother liquor and the newly formed solid phase after the transformation (Mg^{2+} ; Table 3.1).

Figure 3.3 $\text{NiSO}_4 \cdot 7\text{H}_2\text{O}$ crystals.Figure 3.4 SEM image of $\text{NiSO}_4 \cdot 6\text{H}_2\text{O}$ crystals.

The results of the recrystallization experiments at different temperatures are presented in **Table 3.1**. The table shows that the Mg^{2+} content of the recrystallized $\text{NiSO}_4 \cdot 6\text{H}_2\text{O}$ product is 5 to 10 times lower than the Mg^{2+} content of the starting material ($\text{NiSO}_4 \cdot 7\text{H}_2\text{O}$). The partition coefficient is below 1 which indicates that there is a slight preference for magnesium ions to stay in solution. At higher temperature the partition coefficient increases from about 0.5 to about 0.8. An explanation for this effect is that at higher temperature the recrystallization process proceeds faster and the magnesium ions have less time to be transported from the crystal surface into the solution. This results in more entrapment of magnesium ions into the crystal lattice.

Table 3.1 Mass balance and magnesium partition coefficients for the NiSO₄·7H₂O recrystallization experiments at different temperatures. RS: recrystallization solution

| T | NiSO ₄ ·7H ₂ O | | | RS | NiSO ₄ ·6H ₂ O | | | Mother liquor | | | D |
|----|--------------------------------------|-----|------|-------|--------------------------------------|-----|------|---------------|-----|------|------|
| °C | input | Mg | Mg | Input | yield | Mg | Mg | yield | Mg | Mg | |
| | g | ppm | mmol | G | g | ppm | mmol | g | ppm | mmol | |
| 40 | 188 | 276 | 2.14 | 440 | 80 | 45 | 0.15 | 531 | 80 | 1.75 | 0.58 |
| 50 | 129 | 394 | 2.09 | 710 | 156 | 27 | 0.17 | - | 72 | - | 0.34 |
| 60 | 151 | 335 | 2.08 | 525 | 143 | 32 | 0.19 | 514 | 54 | 1.14 | 0.61 |
| 70 | 186 | 335 | 2.57 | 491 | 143 | 53 | 0.31 | 516 | 86 | 1.83 | 0.70 |
| 80 | 162 | 321 | 2.14 | 296 | 127 | 66 | 0.34 | 315 | 126 | 1.63 | 0.93 |
| 90 | 219 | 286 | 2.58 | 301 | 134 | 65 | 0.36 | 339 | 132 | 1.84 | 0.71 |

The process conditions for the experiment with the smallest partition coefficient (50 °C recrystallization temperature) were chosen in order to study the recrystallization time. The results of these experiments are presented in **Table 3.2**. The table shows that after 1 hour of recrystallization all NiSO₄·7H₂O crystals have been recrystallized into NiSO₄·6H₂O. The X-ray diffraction data show that for half of the experiments the NiSO₄·6H₂O crystals also contain some NiSO₄·2H₂O crystals. This is probably caused by dehydration of the NiSO₄·6H₂O crystals after isolation during the drying process. The partition coefficient for Mg in all the experiments is around 0.48. This is in good agreement with the previous experiments.

Table 3.2 Partition coefficients and the crystal structure for recrystallization experiments at 50 °C at different time intervals.

| time(h) | D | Crystal Structure* |
|---------|------|--|
| 1 | 0.53 | NiSO ₄ ·6H ₂ O+ NiSO ₄ ·2H ₂ O |
| 3 | 0.46 | NiSO ₄ ·6H ₂ O+ NiSO ₄ ·2H ₂ O |
| 5 | 0.44 | NiSO ₄ ·6H ₂ O+ NiSO ₄ ·2H ₂ O |
| 10 | 0.46 | NiSO ₄ ·6H ₂ O |
| 24 | 0.52 | - |
| 48 | 0.46 | NiSO ₄ ·6H ₂ O |

*results obtained by X-ray diffraction.

3.3.2 Recrystallization of NiSO₄·7H₂O with reuse of mother liquor

The first recrystallization experiment was performed with nickel sulfate solution prepared from pure nickel sulfate. The resulting mother liquor from the first experiment was reused five times. In the last experiment NiSO₄·7H₂O with a low magnesium content produced from pure NiSO₄·6H₂O was used. The results are presented in **Table 3.3**.

Table 3.3 Mass balance of the $\text{NiSO}_4 \cdot 7\text{H}_2\text{O}$ recrystallization experiments with reuse of mother liquor.

| Exp no. | $\text{NiSO}_4 \cdot 7\text{H}_2\text{O}$ | | | | RS | $\text{NiSO}_4 \cdot 6\text{H}_2\text{O}$ | | | | mother liquor | | | D |
|---------|---|---------|-----------|------------|------------|---|---------|-----------|------------|---------------|-----------|------------|------|
| | input g | Ni % | Mg ppm | Mg mmol | input g | yield g | Ni % | Mg ppm | Mg mmol | yield g | Mg ppm | Mg mmol | Mg |
| 0 | 29.3 | 17.8 | 316 | 0.38 | 874 | 23.7 | 22.7 | 7 | 0.01 | 874 | 13 | 0.47 | 0.49 |
| 1 | 44.8 | 18.9 | 331 | 0.61 | 860 | 24.5 | 22.4 | 13 | 0.01 | 859 | 23 | 0.81 | 0.45 |
| 2 | 38.1 | 19.0 | 344 | 0.54 | 850 | 38.2 | 22.9 | 37 | 0.06 | 835 | 31 | 1.07 | 0.78 |
| 3 | 84.1 | 20.6 | 372 | 1.29 | 827 | 47.1 | 23.5 | 39 | 0.08 | 806 | 66 | 2.19 | 0.50 |
| 4 | 111 | 20.2 | 352 | 1.62 | 794 | 107 | 23.4 | 57 | 0.25 | 757 | 99 | 3.08 | 0.39 |
| 5 | | 19.6 | 7 | | | | 23.8 | 72 | | | 97 | | 0.44 |

RS: recrystallization solution: Experiment 0: RS made from p.a. $\text{NiSO}_4 \cdot 6\text{H}_2\text{O}$; experiment 1-5: RS is the mother liquor from the previous experiment; experiment 5: $\text{NiSO}_4 \cdot 7\text{H}_2\text{O}$ from p. a. $\text{NiSO}_4 \cdot 6\text{H}_2\text{O}$ by EFC

The magnesium concentration in solution and in $\text{NiSO}_4 \cdot 6\text{H}_2\text{O}$ as a function of the number of times the recrystallization solution was reused is presented in **Figure 3.5**. The figure shows that Mg accumulates in the mother liquor because in each cycle Mg is introduced into the mother liquor via the $\text{NiSO}_4 \cdot 7\text{H}_2\text{O}$. Correspondingly, the Mg concentration in the crystallized $\text{NiSO}_4 \cdot 6\text{H}_2\text{O}$ also increases.

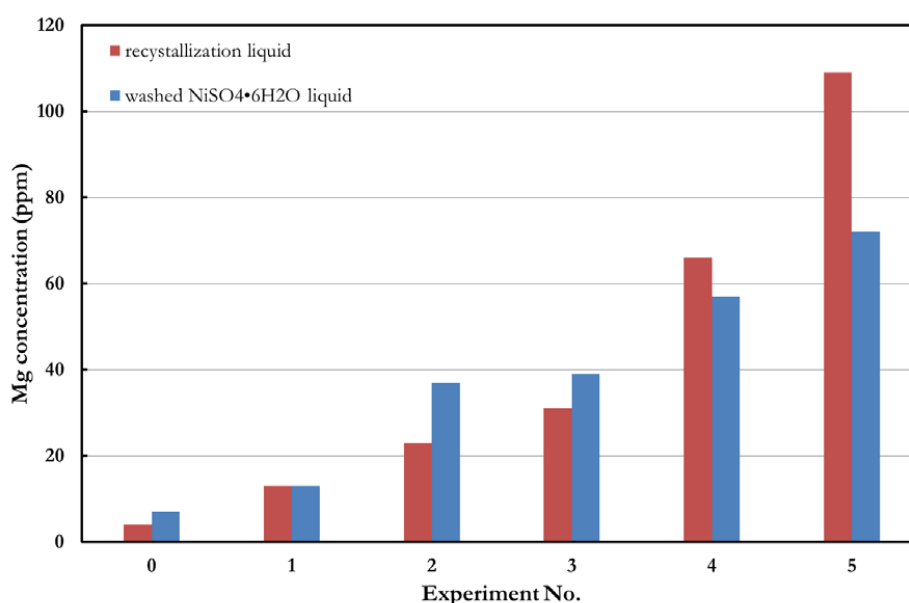


Figure 3.5 Mg concentration in the recrystallization solution and $\text{NiSO}_4 \cdot 6\text{H}_2\text{O}$ crystals as a function of the number of times the recrystallization solution is reused.

Using pure $\text{NiSO}_4 \cdot 7\text{H}_2\text{O}$ as a starting material, resulted in $\text{NiSO}_4 \cdot 6\text{H}_2\text{O}$ containing a substantial amount of Mg which can only have originated from the recycled mother liquor. This confirms that the recrystallization process is solvent mediated. The partition coefficient is independent upon the

Mg concentration in the start solution and independent upon the added source material NiSO₄•7H₂O, which shows that the uptake of Mg in the host lattice follows an isomorphous substitution mechanism. This is in agreement with findings by Balarew (Balarew, 1976). The partition coefficient is about 0.5 which is close to one. This shows that there is only a small preference for the lattice to incorporate the nickel ions instead of the foreign magnesium ions. This small difference can be explained by the similarities between the magnesium and nickel ions. Both ions have the same charge (+2) and the ionic radii are close to each other (Mg: 73 pm; Ni: 69 pm at coordination number (CN) of 6 (Shannon, 1976)). Also the interaction of the magnesium and nickel ions with the sulfate counter ion is of the same order of magnitude. A measure for the interaction between an ion and the counter ion is the solubility of the salt. The solubility of magnesium sulfate at 50 °C is 4.2 m which is comparable to that of nickel sulfate at 3.3 m (Mullin, 2001). The partition coefficient of 0.5 indicates a possibility for a purification process for nickel sulfate, if needed via fractionated crystallization, in which most of the magnesium ions are removed from the nickel sulfate product.

3.3.3 Distribution of trace impurities over the EFC and recrystallization process

From a scientific and economic perspective it is interesting to determine the fate of the other trace impurities in the EFC and recrystallization process and to study the effect of process variations on this distribution. As a first screening, of each EFC and recrystallization process stream samples were taken and analyzed by hrICP-MS. An overview of the main analytical data with respect to each process step is presented in **Table 3.4**. The error margins have not been determined exactly, the accuracy is estimated to range from 10% for for instance Mg²⁺ to over 50 % for trace compounds like Te⁴⁺.

The table shows that next to sodium and magnesium the starting solution contained appreciable levels of K, Li, Ca, Co, Cu, Sr, Zn, Fe, Al, B, Sb, and Se. All other impurities are below the ppm level.

Chapter 3

Table 3.4 Distribution of impurities over the EFC and recrystallization process in $\mu\text{g}/\text{kg}$ (ppb).

| Element | NiSO ₄ start sol. | NiSO ₄ 7-hydrate | EFC ML | NiSO ₄ Wash liquid | NiSO ₄ 6-hydrate | Recryst. ML |
|--------------------|---------------------------------|--------------------------------|------------|----------------------------------|--------------------------------|----------------|
| +1 | | | | | | |
| Na | 9,000,000 | 56,000 | 10,000,000 | 23,000 | 80,000 | 15,000 |
| K | 170,000 | 63,000 | 230,000 | - | 41,000 | - |
| Li | 3,700 | 1,700 | 4,300 | - | 1,500 | - |
| Rb | 300 | 200 | 340 | 10 | 180 | 1 |
| +2 | | | | | | |
| Mg | 300,000 | 600,000 | 330,000 | 4,800 | 19,000 | 12,000 |
| Ca | 64,000 | 87,000 | 81,000 | 18,000 | 75,000 | 4,200 |
| Co | 4,000 | 10,000 | 4,000 | 700 | 1,400 | 900 |
| Cu | 1,000 | 7,000 | 1,000 | 120 | 3,200 | 330 |
| Sr | 15,000 | 4,400 | 18,000 | 160 | 40 | 240 |
| Be | 200 | 1,800 | 200 | 190 | 1,500 | 180 |
| Ba | 300 | 1,700 | 300 | 100 | 140 | 30 |
| Zn | 1,200 | 1,400 | 1,000 | 900 | 2,000 | 360 |
| Ti | 700 | 1,200 | 1,300 | 140 | 2,000 | 100 |
| Mn | 100 | 700 | 120 | 50 | 270 | 100 |
| Hg | 110 | 630 | 90 | 70 | 510 | 60 |
| Zr | 50 | 430 | 50 | 40 | 340 | 40 |
| Sn | 30 | 240 | 30 | 10 | 200 | 5 |
| +3 | | | | | | |
| Fe | 6,500 | 30,000 | 8,100 | 1,400 | 21,000 | - |
| Al | 6,500 | 7,700 | 10,000 | 7,200 | 1,500 | 1,500 |
| B | 18,000 | 7,500 | 22,000 | - | 6,300 | - |
| Sb | 11,000 | 900 | 12,000 | 840 | 360 | 620 |
| Sc | 88 | 706 | 94 | 70 | 600 | 70 |
| Cr | 200 | 600 | 200 | 50 | 140 | - |
| As | 800 | - | 900 | 300 | 70 | 570 |
| Y | 34 | 272 | 36 | 30 | 230 | 30 |
| Rh | 100 | 70 | 120 | 10 | 50 | 10 |
| +4 | | | | | | |
| Se | 21,000 | 101,000 | 20,000 | 1,800 | 3,000 | 2,600 |
| Ge | 260 | 1,600 | 270 | 20 | 180 | 20 |
| Mo | 30 | 250 | 30 | 20 | 230 | 20 |
| Te | 150 | 450 | 180 | 10 | 20 | - |
| +5 | | | | | | |
| V | 80 | 370 | 70 | 40 | 320 | 40 |
| Nb | 30 | 260 | 40 | 30 | 220 | 30 |
| Lanthanides | | | | | | |
| La | 1.8 | 10.6 | 2.6 | 3.1 | 10.0 | 1.3 |
| Ce | 2.8 | 16.5 | 6.0 | 5.7 | 9.8 | 4.3 |
| Pr | 0.9 | 5.8 | 1.1 | 1.1 | 5.0 | 0.6 |
| Nd | 2.1 | 5.8 | 2.7 | 2.1 | 6.0 | 0.5 |
| Sm | 1.6 | 12.0 | 1.9 | 1.1 | 10.0 | 0.8 |
| Eu | 0.7 | 6.1 | 0.8 | 0.6 | 5.2 | 0.5 |
| Gd | 1.1 | 4.7 | 1.1 | 0.7 | 4.1 | 0.5 |
| Dy | 0.9 | 4.0 | 1.0 | 0.6 | 3.4 | 0.5 |
| Ho | 0.9 | 6.5 | 1.0 | 0.8 | 5.6 | 0.7 |
| Er | 1.3 | 8.9 | 1.4 | 1.0 | 9.1 | 1.0 |
| Yb | 0.9 | 5.4 | 1.0 | 0.8 | 7.6 | 0.6 |
| Lu | 10.0 | 80.0 | 10.0 | 10.0 | 70.0 | 10.0 |

EFC:

The partition coefficients as a function of the ionic radius for the EFC process step are presented in Figures 3.6, 3.7 and 3.8.

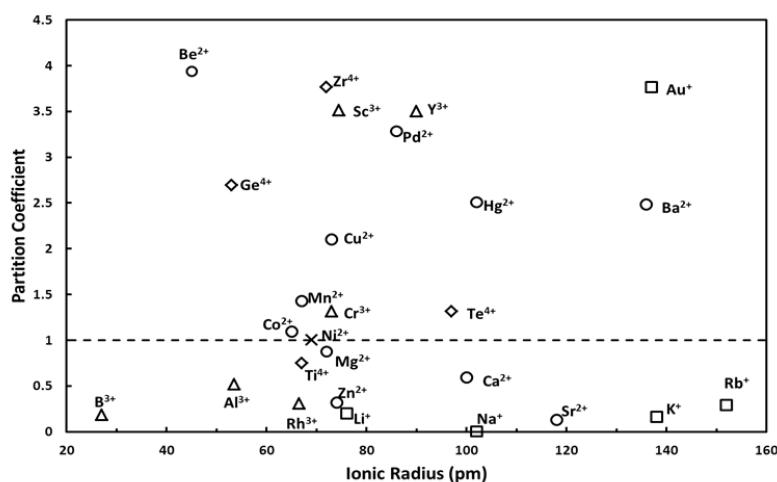


Figure 3.6 Partition coefficients of trace impurities as a function of ionic radius (coordination number=6) (Shannon, 1976) for EFC of $\text{NiSO}_4 \cdot 7\text{H}_2\text{O}$.

Figure 3.6 shows that the monovalent ions Li, Na, K, and Rb preferably remain in solution. This is expected because the high solubility of the sulfate salts makes co-precipitation unlikely and isomorphous substitution is seriously hampered by the difference in charge between the monovalent ions and Ni. With the divalent ions the story is more complex. Ca and Sr exhibit a preference to remain in solution. Possibly the effect of the much larger radius of Ca and Sr hampering isomorphous substitution is more important than the higher interaction of Ca and Sr with the counter ion as indicated by the much lower solubility of calcium sulfate and strontium sulfate. Barium has a preference to end up in the solid phase. Due to the very low solubility of barium sulfate and the much larger radius of the barium ions, making isomorphous substitution in the nickel sulfate lattice difficult, it is likely that the presence of most of the Ba in the solid phase is caused by co-precipitation. For Zn, Mg, Co, Cu, the charge, radius and solubility are comparable with Ni so it is expected that isomorphous substitution takes place. The partition coefficients of Mg and Co are indeed close to 1. The partition coefficients for Zn and Cu lie a little bit further from 1. The trivalent ions also show a more complex pattern. Al has a preference for the solution. This can be explained by the high solubility of the sulfate salt which makes co-precipitation unlikely and isomorphous substitution is seriously hampered by the difference in charge and radius between Al and Ni.

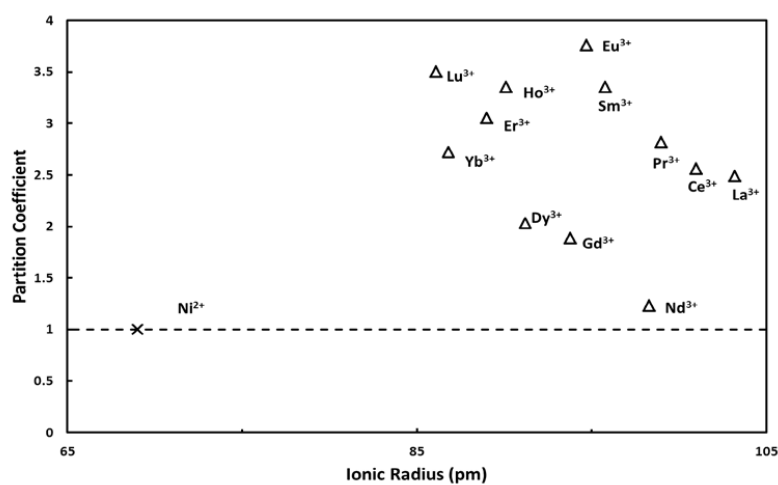


Figure 3.7 Partition coefficients of lanthanides as a function of ionic radius (coordination number =6) (Shannon, 1976) for EFC of $\text{NiSO}_4 \cdot 7\text{H}_2\text{O}$.

The trivalent lanthanides are almost the same in chemical properties. The most important difference is their ionic radius. Figure 3.7 shows that there is no clear relationship between the ionic radius and the partition coefficient. The partition coefficients of the lanthanides lie between 1 and 4 which indicates a slight preference of the lanthanides to incorporate in the solid phase. An explanation for the high uptake of lanthanides into the solid phase is the higher interaction of the lanthanides with the sulfate anion as reflected by the lower solubility of the lanthanide sulfates as compared to nickel sulfate.

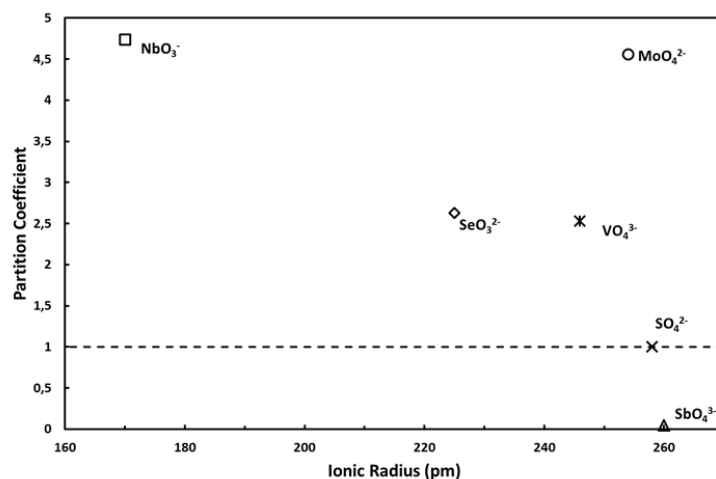


Figure 3.8 Partition coefficients of oxyanions as a function of ionic radius (coordination number=6) for EFC of $\text{NiSO}_4 \cdot 7\text{H}_2\text{O}$.

Although no speciation has been determined, it was expected that certain elements form oxyanions such as molybdate, selenite, vanadate and niobate. These show a preference to be incorporated in the solid phase (**Figure. 3.8**). Antimonate has a preference to remain in solution.

Recrystallization:

The partition coefficients as a function of the ionic radius and temperature for the recrystallization step are presented in **Figures 3.9, 3.10 and 3.11**.

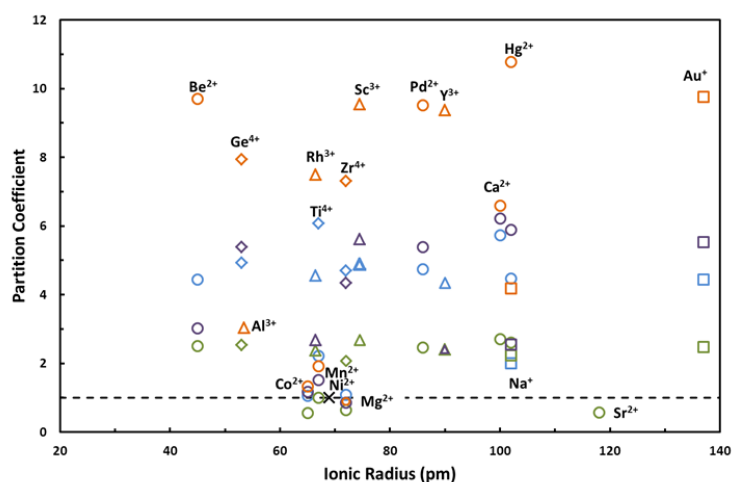


Figure 3.9 Partition coefficients of trace impurities as a function of ionic radius (coordination number=6) for recrystallization of $\text{NiSO}_4 \cdot 7\text{H}_2\text{O}$ into the $\text{NiSO}_4 \cdot 6\text{H}_2\text{O}$ form at different temperatures (40 °C-blue; 50 °C-green; 70 °C-purple; 80 °C-orange).

Figures 3.9, 3.10 and 3.11 show that most of the impurities present have a preference to become taken up by the crystal. A possible explanation for this is that at higher temperatures the solubility of nickel sulfate is higher than for many of the other salts, which correlates with a high D for impurities (Balarew, 1976). For ions with a comparable solubility, ionic radius and charge like Co, Mg and Mn where isomorphous substitution is the preferential mode of uptake the partition coefficient is about 1 as expected. **Table 3.4** shows that after recrystallization the concentration of Co, Mg, Cu has decreased significantly in the solid phase.

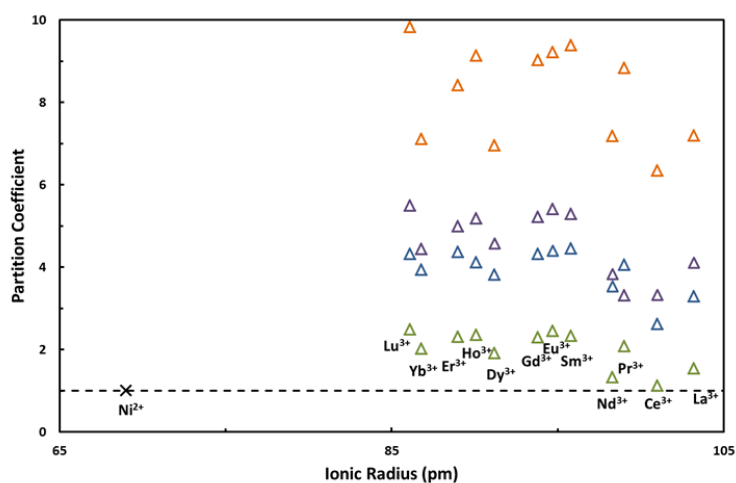


Figure 3.10 Partition coefficients of lanthanides as a function of ionic radius (coordination number=6) for recrystallization of $\text{NiSO}_4 \cdot 7\text{H}_2\text{O}$ into the $\text{NiSO}_4 \cdot 6\text{H}_2\text{O}$ form at different temperatures (40 °C-blue; 50 °C-green; 70 °C-purple; 80 °C-orange).

Figure 3.10 shows that for the lanthanides the partition coefficient increases with increasing temperature (with the exception of the experiment at 40 °C). This same effect is visible for other ions in **Figure 3.9**. A possible explanation for this is that the solubility of nickel sulphate increases with temperature whereas the solubility of the lanthanide sulfates decreases with temperature. A second factor that is of importance is the kinetics of the recrystallization process. At higher temperature the recrystallization process proceeds faster. This implies that at higher temperature impurities and nickel ions have less time to be transported through the solution and that D approaches 1. Given the fact that the D -value of Mg^{2+} does not change much with temperature, this kinetic effect is probably minor here.

Figure 3.11 shows that the expected oxyanions follow the same trend as in EFC: molybdate, selenite, vanadate and niobate have a preference to be incorporated in the solid phase. Antimonate has a preference to remain in solution.

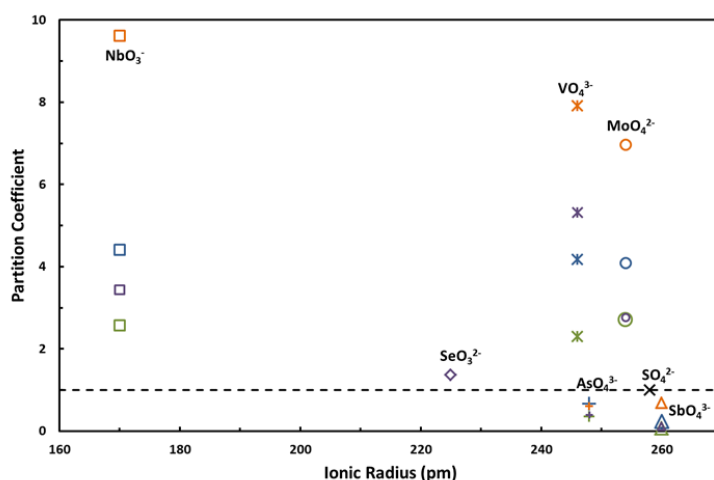


Figure 3.11 Partition coefficients of the oxyanions as a function of ionic radius (coordination number=6) for recrystallization of $\text{NiSO}_4 \cdot 7\text{H}_2\text{O}$ into the $\text{NiSO}_4 \cdot 6\text{H}_2\text{O}$ form at different temperatures (40 °C-blue; 50 °C-green; 70 °C-purple; 80 °C-orange).

In this first set of experiments an indication of the fate of the trace impurities over the different streams in the EFC process of $\text{NiSO}_4 \cdot 7\text{H}_2\text{O}$ and in the subsequent recrystallization into $\text{NiSO}_4 \cdot 6\text{H}_2\text{O}$ has been obtained. In order to get a more detailed picture more experiments have to be performed with the focus on continuous operation and a detailed study of the impact of relevant process parameters.

3.5 Conclusions

Recrystallization:

The completely altered shape of the crystals and the redistribution of ions like Mg over the solid and liquid phase show that the recrystallization of $\text{NiSO}_4 \cdot 7\text{H}_2\text{O}$ into $\text{NiSO}_4 \cdot 6\text{H}_2\text{O}$ is a solvent mediated process.

The partition coefficient for the main impurity Mg was independent upon the Mg concentration in the start solution and independent upon the source material, which shows that the uptake of Mg in the host lattice follows an isomorphous substitution mechanism.

Chapter 3

The partition coefficient of Mg in the recrystallization step is about 0.5.

The partition coefficients of the lanthanides increased with an increase in recrystallization temperature. A possible explanation for this effect is that the solubility of nickel sulphate increases with temperature whereas the solubility of the lanthanide sulfates decreases with temperature. This effect is not a fundamental effect.

Most of the impurities in the recrystallization step had a preference to remain in the solid phase. An explanation for this effect is that at higher temperatures the solubility of nickel sulfate is higher than for most of the other salts. For ions with a comparable solubility, ionic radius and charge like Co, Mg and Mn the partition coefficient is about 1 as expected.

EFC:

In the EFC process the monovalent ions Li, Na, K, and Rb and the trivalent ion Al preferably remain in solution because the high solubility of the sulfate salts makes co-precipitation unlikely and isomorphous substitution is hampered by the difference in charge and size.

The divalent ions Ca and Sr have a preference to remain in solution. Possibly the effect of the larger radius of Ca and Sr hampering isomorphous substitution is more important than the higher interaction of Ca and Sr with the counter ion as indicated by their lower solubility.

For Zn, Mg, Co, Cu, the partition coefficients are close to 1, as expected from the charge, radius and solubility that are comparable with Ni. It is expected that isomorphous substitution is an important process.

Barium has a preference to end up in the solid phase. Due to the very low solubility of barium sulfate and the much larger radius of the barium ions this is likely caused by co-precipitation.

An explanation for the high uptake of lanthanides into the solid phase is the higher interaction of the lanthanides with the sulphate anion as reflected by their lower solubility.

References

- Balarew, C., 1976. Isodimorphous cocrystallization in sulphate systems as a possibility of predicting the existence of crystal hydrates of the type $\text{MSO}_4 \cdot n\text{H}_2\text{O}$ ($M = \text{Mn}^{2+}, \text{Fe}^{2+}, \text{Co}^{2+}, \text{Ni}^{2+}, \text{Cu}^{2+}, \text{Ni}^{2+}, \text{Cu}^{2+}, \text{Zn}^{2+}, \text{Cd}^{2+}$). *Z. anorg. allg. Chem* 422(3): 283-288.
- Fron del, C. and Palache, C., 1949. Retgersite, $\text{NiSO}_4 \cdot 6\text{H}_2\text{O}$ a New Mineral. *Am Mineral*, 34(3-4): 188-194.
- Genceli, F.E., Gartner, R. and Witkamp, G.J., 2005. Eutectic freeze crystallization in a 2nd generation cooled disk column crystallizer for $\text{MgSO}_4 \cdot \text{H}_2\text{O}$ system. *J Cryst Growth*, 275(1-2): E1369-E1372.
- Gupta, C.K., 2003. *Chemical Metallurgy : Principles and Practice*. Wiley - VCH Verlag GmbH & Co. KGaA.
- Himawan, C. and Witkamp, G.J., 2006. Crystallization kinetics of $\text{MgSO}_4 \cdot 12\text{H}_2\text{O}$ from different scales of batch cooling scraped crystallizers. *Cryst Res Technol*, 41(9): 865-873.
- Mullin, J.W., 2001. *Crystallization*. Elsevier Butterworth-Heinemann.
- Pascual, M.R., Trambitas, D., Calvo, E.S., Kramer, H. and Witkamp, G.J., 2010. Determination of the eutectic solubility lines of the ternary system $\text{NaHCO}_3\text{-Na}_2\text{CO}_3\text{-H}_2\text{O}$. *Chem Eng Res Des*, 88(10A): 1365-1371.
- Pronk, P., Ferreira, C.A.I. and Witkamp, G.J., 2009. Prevention of fouling and scaling in stationary and circulating liquid-solid fluidized bed heat exchangers: Particle impact measurements and analysis. *Int J Heat Mass Tran*, 52(15-16): 3857-3868.
- Rohmer, R., 1939. Dehydrating magnesium sulphate in 7 mol/g of water by aqueous means. Intermediary hydrates. *Cr Hebd Acad Sci*, 209: 315-317.
- Shannon, R.D., 1976. Revised Effective Ionic Radii and Systematic studies of Interatomic Distances in Halides and Chalcogenides. *Acta Cryst.*, A32: 751-767.
- Vaessen, R., Seckler, M. and Witkamp, G.J., 2003. Eutectic freeze crystallization with an aqueous $\text{KNO}_3\text{-HNO}_3$ solution in a 100-L cooled-disk column crystallizer. *Ind Eng Chem Res*, 42(20): 4874-4880.
- van der Ham, F., 1999. *Eutectic Freezey Crystallization*, PhD Thesis, Delft Univesity of Technology.
- Van Spronsen, J. et al., 2010. Eutectic freeze crystallization from the ternary $\text{Na}_2\text{CO}_3\text{-NaHCO}_3\text{-H}_2\text{O}$ system A novel scraped wall crystallizer for the recovery of soda from an industrial aqueous stream. *Chem Eng Res Des*, 88(9A): 1259-1263.
- Witkamp, G.J., 1989. *Crystallization of Calcium Sulfate and Uptake of Impurities*. PhD thesis, Delft University of Technology.



Chapter 4

Analysis of NiSO_4 Samples by hrICP-MS

will be submitted as supporting material to the articles of Chapter 2/3.

Abstract

During our investigations on treating NiSO_4 containing industrial streams, EFC proved to be an efficient technique for the recovery of $\text{NiSO}_4 \cdot 7\text{H}_2\text{O}$ and pure water from an industrial nickel sulfate solution. The resulting $\text{NiSO}_4 \cdot 7\text{H}_2\text{O}$ could be further purified by recrystallization into $\text{NiSO}_4 \cdot 6\text{H}_2\text{O}$. In order to determine the fate of the trace impurities over the EFC and recrystallization process the trace impurities in each process stream were carefully determined by high resolution inductively coupled plasma-mass spectrometry (hrICP-MS). HrICP-MS was chosen because it makes determination of trace elements on the ppb level ($\mu\text{g}/\text{kg}$) possible. This chapter describes the development of the analytical procedure. The effect of the nitric acid concentration in the blanks, used for dilution of samples and standards and for flushing, proved to be minor. The memory effect was sufficiently diminished by prolonging the flushing sequence. Signal decline in the course of a measurement run was quantified and compensated for. Internal standards did not improve the accuracy and gave different results for different elements which could not be explained satisfactorily. Elements present in the blank solution and foreign elements present in the standards were determined. After taking all these factors into consideration the compositions of the NiSO_4 samples were determined.

4.1 Introduction

HrICP-MS is a method in elemental analysis for the determination of the total element composition. Its working principle of introducing a sample in a high energy plasma that breaks all the bonds of the chemical species in the sample makes the response of hrICP-MS independent of the chemical form of the elements under investigation (Ammann, 2007). So, hrICP-MS is suitable for multi-element and multi-isotope determination and is applicable in a broad range investigations in the environmental, clinical, pharmaceutical and industrial field (Cornelis et al., 2003). However, the optimal performance is not always achieved easily because the technique is still hampered by challenges that need to be met before a reproducible analysis is possible. For instance, spectral and non-spectral interferences (Agatemor and Beauchemin, 2011; Vanhaecke et al., 1995), contaminations, memory effects, matrix effects, quality of solvents and standards, back ground noise, and sample preparation method need to be optimized.

In this work, an analytical method, based on hrICP-MS was developed for the determination of trace impurities in streams from the recovery of NiSO₄·7H₂O from an industrial nickel sulfate solution by EFC and from the recrystallization of NiSO₄·7H₂O into NiSO₄·6H₂O. After improving the analytical procedure concerning the memory effect, signal decline, usage of internal standards and smaller factors like the nitric acid concentration in the blanks, the composition of the NiSO₄ samples were determined.

4.2 Materials and Methods

4.2.1 hrICP-MS Equipment

The hrICP-MS system used for the measurements was a Finnigan Element 2 (Thermo Finnigan Scientific Inc., Germany) (**Figure 4.1**). The Element 2 hrICP-MS consists of the following components (**Figure 4.2**):

Sample introduction system composes of a nebulizer and spray chamber. ICP torch and RF coil generate the argon plasma. Interface links the atmospheric pressure ICP ion source to the high vacuum mass spectrometer. Vacuum system provides high vacuum for ion optics, magnetic/electric sectors and detector. Ion optics guides the desired ions into the magnetic sector while assuring that neutral species and photons are discarded from the ion beam. Magnetic sector acts as a mass filter to sort ions by their mass. Electric sector analyzer is used for high resolution to remove interferences that can decrease the detection limit. Detector counts individual ions exiting the

magnetic/electric sectors. Data handling and system controller control all aspects of instrument control and data handling to obtain final concentration results.

The working principle of Element 2 hrICP-MS is as follows. A liquid sample is introduced by a peristaltic pump to a nebulizer that creates an aerosol of fine droplets using an argon flow of about 1L/min. These fine droplets pass through a spray chamber before they are allowed to enter the plasma. The function of the spray chamber is to allow a substantial number of the small droplets to enter the plasma while discarding the larger droplets which can create analytical problems. In the plasma, the liquid droplets, containing the sample matrix and the elements to be determined, are evaporated. As the atoms continue their travel through the argon plasma, they absorb more energy and eventually release one electron to form mainly singly charged ions that enter the interface region.

The interface connects the plasma and the ion lens system and through it the ions pass into the ion lens region. The interface consists of two inverted funnel-like devices called cones (sampler cone and skimmer cone, **Figure 4.3**). With a two-step pressure reduction, the ion beam undergoes substantial divergence as it exits the second cone, thus requiring additional focusing before the ion beam enters the magnetic sector. This additional focusing step functions as an extraction lens, where the ion beam is extracted and the non-ionized materials (neutrals and photons) are separated. As the ion beam passes the transfer optics, all of the non-ionized materials are removed. The transfer optics is also designed for focusing and positioning in order to keep the ion beam at the maximal intensity.

After the transfer optics the ion beam enters the magnetic sector through the entrance slit. On this entrance slit, there are three separated slits with different sizes. In the middle, there is the widest slit for low resolution (LR); the right one is the midsize one for medium resolution (MR) and the left one is the smallest one for high resolution (HR).

When the ion beam has passed the transfer optics and the entrance slit, it enters the magnetic sector, which is used to focus ions with diverging angles of motion from the entrance slit to the intermediate (beta) slit. After that the electric sector analyzer, focuses ions with diverging angles of motion from the beta slit on to the exit slit. It is dispersive with respect to ion energy only.



Figure 4.1 The hrICP-MS equipment.

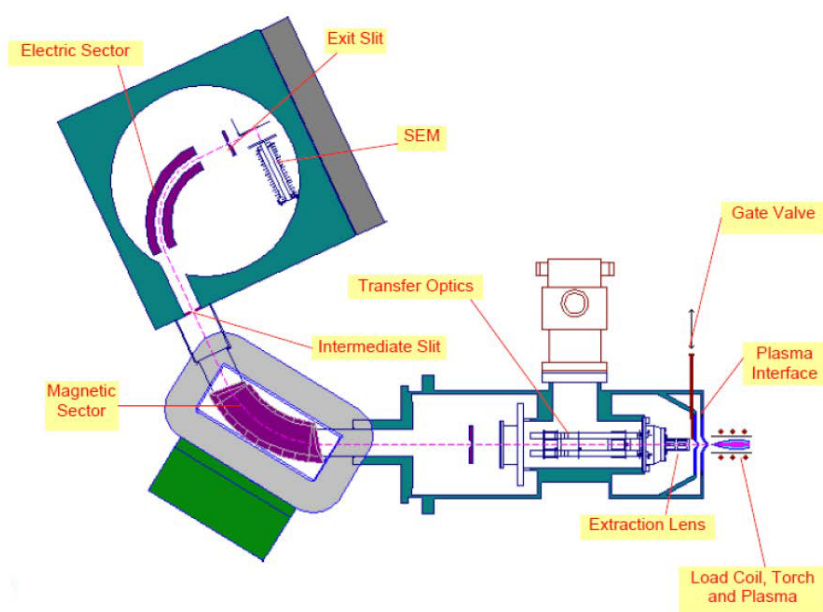


Figure 4.2 The components of Element 2 (ThermoFinnigan, 2008).

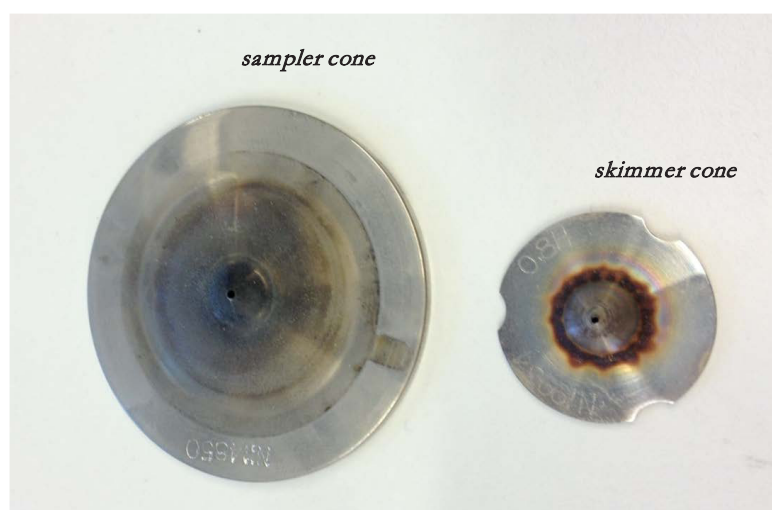


Figure 4.3 Photo of sample cone and skimmer cone of the plasma interface.

The ions exiting the mass spectrometer strike the active surface of the detector called conversion dynode and generate a measurable electronic signal. These signals are collected by counting and analog modes.

4.2.2 Preparation of blanks, standards and samples

Pure water was used from an PURELAB Utral device (ELGA). Nitric acid for trace metal analysis were obtained from J.T. Baker.

Blank solutions containing 3, 6 and 9 wt% nitric acid were prepared. The blank solution (3% nitric acid unless stated otherwise) was used for dilution of the samples and standards and as flushing solution to clean the measuring system. **Tables 4.1-4.6** show the composition of the standards used in the three runs. In the third run internal standard was added to the blanks, standards and samples. Concentrations are expressed as ppb, signifying micrograms per kg solution.

Run 1

Table 4.1 Element composition of standard s1-s24.

| s1-s4 | s11-s14 | s21-s24 |
|--|---|--|
| Li, Be, B, Na, Mg, Al, K, Ca, V, Cr, | Sc, Ti, Ge, Y, Zr, Nb Rh, Pd, Sn, Sb, Lu, Hf | La, Ce, Pr, Nd, Sm Eu, Gd, Dy, Ho, Er, Yb |
| Mn, Fe, Co, Ni, Cu, Zn, Ga, As, Se | W, Pt, Au, Hg | |
| Rb, Sr, Mo, Ag, Cd, Te, Ba, Tl, Pb, Bi, U | | |

Table 4.2 Concentration of elements in standard s1-s24.

| Standards' name | Concentration (unit: ppb) |
|-----------------|---------------------------|
| S1, S11, S21 | 1 |
| S2, S12, S22 | 10 |
| S3, S13, S23 | 100 |
| S4, S14, S24 | 1000 |

Run 2

Table 4.3 Composition of standard S1-S44 (unit: ppb).

| | S1 | S2 | S3 | S4 | S5 | S6 | S7 | S8 | S9 | S10 | S11 |
|----|-------|--------|-------|-------|-------|-------|-------|-------|-------|-------|-------|
| Li | 0.049 | 0.107 | 0.232 | 0.443 | 0.97 | 2.14 | 4.78 | 9.67 | 19.49 | 50.83 | 98.2 |
| Be | 0.507 | 1.116 | 2.419 | 4.609 | 10.05 | 22.24 | 49.70 | 100.6 | 202.9 | 529.0 | 1023 |
| B | 0.487 | 1.073 | 2.324 | 4.428 | 9.65 | 21.37 | 47.75 | 96.7 | 194.9 | 508.3 | 982 |
| Na | 0.046 | 0.102 | 0.221 | 0.420 | 0.92 | 2.03 | 4.53 | 9.17 | 18.50 | 48.23 | 93.2 |
| Mg | 0.050 | 0.111 | 0.239 | 0.456 | 0.99 | 2.20 | 4.92 | 9.96 | 20.09 | 52.38 | 101.3 |
| Al | 0.050 | 0.109 | 0.237 | 0.452 | 0.99 | 2.18 | 4.87 | 9.86 | 19.89 | 51.87 | 100.3 |
| K | 0.048 | 0.105 | 0.228 | 0.434 | 0.95 | 2.09 | 4.68 | 9.47 | 19.09 | 49.79 | 96.2 |
| Ca | 5.045 | 11.109 | 24.07 | 45.86 | 100.0 | 221.3 | 494.6 | 1001 | 2019 | 5264 | 10175 |
| V | 0.050 | 0.111 | 0.239 | 0.456 | 0.99 | 2.20 | 4.92 | 9.96 | 20.09 | 52.38 | 101.3 |
| Cr | 0.053 | 0.117 | 0.254 | 0.483 | 1.05 | 2.33 | 5.21 | 10.55 | 21.28 | 55.50 | 107.3 |
| Mn | 0.051 | 0.112 | 0.242 | 0.461 | 1.00 | 2.22 | 4.97 | 10.06 | 20.29 | 52.90 | 102.3 |
| Fe | 0.497 | 1.094 | 2.371 | 4.518 | 9.85 | 21.80 | 48.73 | 98.6 | 198.9 | 518.7 | 1002 |
| Co | 0.051 | 0.112 | 0.242 | 0.461 | 1.00 | 2.22 | 4.97 | 10.06 | 20.29 | 52.90 | 102.3 |
| Ni | 0.050 | 0.111 | 0.239 | 0.456 | 0.99 | 2.20 | 4.92 | 9.96 | 20.09 | 52.38 | 101.3 |
| Cu | 0.051 | 0.112 | 0.242 | 0.461 | 1.00 | 2.22 | 4.97 | 10.06 | 20.29 | 52.90 | 102.3 |
| Zn | 0.502 | 1.105 | 2.395 | 4.564 | 9.95 | 22.02 | 49.21 | 99.6 | 200.9 | 523.8 | 1010 |
| Ga | 0.050 | 0.111 | 0.239 | 0.456 | 0.99 | 2.20 | 4.92 | 9.96 | 20.09 | 52.38 | 101.3 |
| As | 0.507 | 1.116 | 2.419 | 4.609 | 10.05 | 22.24 | 49.70 | 100.6 | 202.9 | 529.0 | 1022 |
| Se | 0.512 | 1.127 | 2.442 | 4.654 | 10.15 | 22.46 | 50.19 | 101.6 | 204.9 | 534.2 | 1033 |
| Rb | 0.049 | 0.107 | 0.232 | 0.443 | 0.97 | 2.14 | 4.78 | 9.67 | 19.49 | 50.83 | 98.2 |
| Sr | 0.051 | 0.113 | 0.244 | 0.465 | 1.01 | 2.25 | 5.02 | 10.16 | 20.49 | 53.42 | 103.3 |
| Mo | 0.051 | 0.112 | 0.242 | 0.461 | 1.00 | 2.22 | 4.97 | 10.06 | 20.29 | 52.90 | 102.3 |
| Ag | 0.051 | 0.112 | 0.242 | 0.461 | 1.00 | 2.22 | 4.97 | 10.06 | 20.29 | 52.90 | 102.3 |
| Cd | 0.051 | 0.113 | 0.244 | 0.465 | 1.01 | 2.25 | 5.02 | 10.16 | 20.49 | 53.42 | 103.3 |
| Te | 0.051 | 0.113 | 0.244 | 0.465 | 1.01 | 2.25 | 5.02 | 10.16 | 20.49 | 53.42 | 103.3 |
| Ba | 0.052 | 0.114 | 0.247 | 0.470 | 1.02 | 2.27 | 5.07 | 10.26 | 20.69 | 53.94 | 104.3 |
| Tl | 0.051 | 0.112 | 0.242 | 0.461 | 1.00 | 2.22 | 4.97 | 10.06 | 20.29 | 52.90 | 102.3 |
| Pb | 0.050 | 0.111 | 0.239 | 0.456 | 0.99 | 2.20 | 4.92 | 9.96 | 20.09 | 52.38 | 101.3 |
| Bi | 0.051 | 0.113 | 0.244 | 0.465 | 1.01 | 2.25 | 5.02 | 10.16 | 20.49 | 53.42 | 103.3 |
| U | 0.050 | 0.111 | 0.239 | 0.456 | 0.99 | 2.20 | 4.92 | 9.96 | 20.09 | 52.38 | 101.3 |

Table 4.3 Composition of standard S1-S44 (unit: ppb) (continued).

| | S21 | S22 | S23 | S24 | S25 | S26 | S27 | S28 |
|-----|-------|-------|-------|-------|------|------|-------|-------|
| La | 0.105 | 0.238 | 0.453 | 1.043 | 2.26 | 4.85 | 9.23 | 99.7 |
| Ce | 0.107 | 0.243 | 0.461 | 1.063 | 2.30 | 4.94 | 9.41 | 101.6 |
| Pr | 0.106 | 0.241 | 0.457 | 1.054 | 2.28 | 4.90 | 9.33 | 100.7 |
| Nd | 0.106 | 0.241 | 0.459 | 1.057 | 2.29 | 4.91 | 9.36 | 101.0 |
| Sm | 0.107 | 0.243 | 0.462 | 1.066 | 2.31 | 4.96 | 9.43 | 101.9 |
| Eu | 0.105 | 0.238 | 0.453 | 1.043 | 2.26 | 4.85 | 9.23 | 99.7 |
| Gd | 0.106 | 0.240 | 0.456 | 1.052 | 2.28 | 4.89 | 9.31 | 100.5 |
| Dy | 0.105 | 0.239 | 0.455 | 1.049 | 2.27 | 4.88 | 9.28 | 100.2 |
| Ho | 0.105 | 0.239 | 0.455 | 1.048 | 2.27 | 4.87 | 9.27 | 100.1 |
| Er | 0.104 | 0.237 | 0.451 | 1.040 | 2.25 | 4.83 | 9.20 | 99.4 |
| Yb | 0.106 | 0.241 | 0.459 | 1.057 | 2.29 | 4.91 | 9.35 | 101.0 |
| | S31 | S32 | S33 | S34 | S35 | S36 | S37 | S38 |
| Sc | 0.109 | 0.249 | 0.463 | 1.072 | 2.25 | 5.01 | 9.55 | 103.9 |
| Ti | 0.108 | 0.247 | 0.459 | 1.062 | 2.23 | 4.97 | 9.47 | 103.0 |
| Ge | 0.107 | 0.243 | 0.452 | 1.046 | 2.19 | 4.89 | 9.32 | 101.4 |
| Y | 0.109 | 0.249 | 0.463 | 1.072 | 2.25 | 5.01 | 9.55 | 103.9 |
| Zr | 0.104 | 0.238 | 0.442 | 1.024 | 2.15 | 4.79 | 9.13 | 99.3 |
| Nb | 0.108 | 0.246 | 0.458 | 1.060 | 2.22 | 4.96 | 9.44 | 102.7 |
| Rh | 0.106 | 0.243 | 0.451 | 1.045 | 2.19 | 4.89 | 9.31 | 101.3 |
| Pd | 0.108 | 0.246 | 0.458 | 1.060 | 2.22 | 4.96 | 9.45 | 102.8 |
| Sn | 0.116 | 0.264 | 0.491 | 1.137 | 2.38 | 5.32 | 10.13 | 110.2 |
| Sb | 0.108 | 0.246 | 0.456 | 1.057 | 2.22 | 4.94 | 9.42 | 102.5 |
| Lu | 0.108 | 0.247 | 0.459 | 1.062 | 2.23 | 4.97 | 9.47 | 103.0 |
| Hf | 0.110 | 0.251 | 0.466 | 1.080 | 2.26 | 5.05 | 9.62 | 104.7 |
| W | 0.107 | 0.244 | 0.453 | 1.050 | 2.20 | 4.91 | 9.35 | 101.8 |
| Pt | 0.111 | 0.253 | 0.470 | 1.089 | 2.28 | 5.09 | 9.71 | 105.6 |
| Au | 0.130 | 0.296 | 0.551 | 1.276 | 2.67 | 5.97 | 11.37 | 123.7 |
| Hg | 0.109 | 0.248 | 0.460 | 1.066 | 2.24 | 4.99 | 9.50 | 103.4 |
| | S41 | S42 | S43 | S44 | | | | |
| Si | 1.101 | 2.369 | 5.186 | 9.862 | | | | |
| PO4 | 1.077 | 2.318 | 5.076 | 9.652 | | | | |
| SO4 | 1.068 | 2.298 | 5.032 | 9.568 | | | | |
| Cl | 1.068 | 2.298 | 5.032 | 9.568 | | | | |
| Br | 1.077 | 2.318 | 5.076 | 9.652 | | | | |

Run 3

Table 4.4 The composition of standards S101-S104 and S1-S4 (unit: ppb).

| Element | S101 | S102 | S103 | S104 | S1 | S2 | S3 | S4 |
|---------|-------|-------|-------|-------|-------|-------|-------|--------|
| Li | 0.459 | 1.033 | 2.296 | 4.594 | 24.08 | 53.35 | 119.6 | 239.6 |
| Be | 4.776 | 10.76 | 23.89 | 47.82 | 250.7 | 555.2 | 1245 | 2494 |
| B | 4.588 | 10.33 | 22.96 | 45.94 | 240.8 | 533.5 | 1196 | 2396 |
| Na | 0.435 | 0.981 | 2.178 | 4.360 | 22.86 | 50.63 | 113.5 | 227.4 |
| Mg | 0.473 | 1.065 | 2.366 | 4.735 | 24.82 | 54.98 | 123.3 | 247.0 |
| Al | 0.468 | 1.054 | 2.342 | 4.688 | 24.58 | 54.44 | 122.1 | 244.5 |
| K | 0.449 | 1.012 | 2.249 | 4.500 | 23.59 | 52.26 | 117.2 | 234.7 |
| Ca | 47.52 | 107.0 | 237.8 | 475.8 | 2494 | 5525 | 12391 | 24818 |
| V | 0.473 | 1.065 | 2.366 | 4.735 | 24.82 | 54.98 | 123.3 | 247.0 |
| Cr | 0.501 | 1.128 | 2.506 | 5.016 | 26.30 | 58.25 | 130.6 | 261.7 |
| Mn | 0.478 | 1.075 | 2.389 | 4.782 | 25.07 | 55.52 | 124.5 | 249.4 |
| Fe | 4.682 | 10.54 | 23.43 | 46.88 | 245.8 | 544.4 | 1220 | 2445 |
| Co | 0.478 | 1.075 | 2.389 | 4.782 | 25.07 | 55.52 | 124.5 | 249.4 |
| Ni | 0.473 | 1.065 | 2.366 | 4.735 | 24.82 | 54.98 | 123.3 | 247.0 |
| Cu | 0.478 | 1.075 | 2.389 | 4.782 | 25.07 | 55.52 | 124.5 | 249.4 |
| Zn | 4.729 | 10.65 | 23.66 | 47.35 | 248.2 | 549.8 | 1233 | 2469.6 |
| Ga | 0.473 | 1.065 | 2.366 | 4.735 | 24.82 | 54.98 | 123.3 | 247.0 |
| As | 4.776 | 10.76 | 23.89 | 47.82 | 250.7 | 555.2 | 1245 | 2494 |
| Se | 4.823 | 10.86 | 24.13 | 48.29 | 253.1 | 560.7 | 1257 | 2518 |
| Rb | 0.459 | 1.033 | 2.296 | 4.594 | 24.08 | 53.35 | 119.6 | 239.7 |
| Sr | 0.482 | 1.086 | 2.413 | 4.829 | 25.31 | 56.07 | 125.7 | 251.9 |
| Mo | 0.478 | 1.075 | 2.389 | 4.782 | 25.07 | 55.52 | 124.5 | 249.4 |
| Ag | 0.478 | 1.075 | 2.389 | 4.782 | 25.07 | 55.52 | 124.5 | 249.4 |
| Cd | 0.482 | 1.086 | 2.413 | 4.829 | 25.31 | 56.07 | 125.7 | 251.9 |
| Te | 0.482 | 1.086 | 2.413 | 4.829 | 25.31 | 56.07 | 125.7 | 251.9 |
| Ba | 0.487 | 1.097 | 2.436 | 4.875 | 25.56 | 56.61 | 127.0 | 254.3 |
| Tl | 0.478 | 1.075 | 2.389 | 4.782 | 25.07 | 55.52 | 124.5 | 249.4 |
| Pb | 0.473 | 1.065 | 2.366 | 4.735 | 24.82 | 54.98 | 123.3 | 247.0 |
| Bi | 0.482 | 1.086 | 2.413 | 4.829 | 25.31 | 56.07 | 125.7 | 251.9 |
| U | 0.473 | 1.065 | 2.366 | 4.735 | 24.82 | 54.98 | 123.3 | 247.0 |

Table 4.5 The composition of standards S111-S114 and S11-S14 (unit: ppb).

| Element | S111 | S112 | S113 | S114 | S11 | S12 | S13 | S14 |
|---------|-------|-------|-------|-------|-------|-------|-------|-------|
| Sc | 0.455 | 1.006 | 2.260 | 4.533 | 23.80 | 53.88 | 118.5 | 237.4 |
| Ti | 0.451 | 0.997 | 2.241 | 4.493 | 23.59 | 53.41 | 117.5 | 235.3 |
| Ge | 0.444 | 0.982 | 2.207 | 4.425 | 23.23 | 52.60 | 115.7 | 231.8 |
| Y | 0.455 | 1.006 | 2.261 | 4.535 | 23.81 | 53.90 | 118.6 | 237.5 |
| Zr | 0.435 | 0.961 | 2.161 | 4.333 | 22.75 | 51.50 | 113.3 | 226.9 |
| Nb | 0.449 | 0.994 | 2.235 | 4.482 | 23.53 | 53.28 | 117.2 | 234.7 |
| Rh | 0.443 | 0.980 | 2.203 | 4.418 | 23.20 | 52.52 | 115.6 | 231.4 |
| Pd | 0.450 | 0.995 | 2.236 | 4.484 | 23.54 | 53.30 | 117.3 | 234.9 |
| Sn | 0.482 | 1.067 | 2.398 | 4.809 | 25.25 | 57.16 | 125.8 | 251.9 |
| Sb | 0.448 | 0.992 | 2.230 | 4.471 | 23.47 | 53.15 | 116.9 | 234.2 |
| Lu | 0.451 | 0.997 | 2.241 | 4.493 | 23.59 | 53.41 | 117.5 | 235.3 |
| Hf | 0.458 | 1.013 | 2.278 | 4.568 | 23.98 | 54.29 | 119.5 | 239.2 |
| W | 0.445 | 0.985 | 2.214 | 4.440 | 23.31 | 52.78 | 116.1 | 232.6 |
| Pt | 0.462 | 1.022 | 2.298 | 4.607 | 24.19 | 54.76 | 120.5 | 241.3 |
| Au | 0.541 | 1.197 | 2.691 | 5.397 | 28.33 | 64.15 | 141.1 | 282.7 |
| Hg | 0.452 | 1.001 | 2.249 | 4.511 | 23.68 | 53.62 | 118.0 | 236.3 |

Table 4.6 The composition of standards S121-S124 and S21-S24 (unit: ppb).

| Element | S121 | S122 | S123 | S124 | S21 | S22 | S23 | S24 |
|---------|-------|-------|-------|-------|-------|-------|-------|-------|
| La | 0.843 | 0.437 | 2.176 | 4.354 | 23.05 | 50.69 | 113.6 | 228.1 |
| Ce | 0.859 | 0.446 | 2.218 | 4.438 | 23.49 | 51.66 | 115.8 | 232.5 |
| Pr | 0.852 | 0.442 | 2.199 | 4.399 | 23.29 | 51.21 | 114.8 | 230.5 |
| Nd | 0.854 | 0.443 | 2.205 | 4.412 | 23.35 | 51.36 | 115.1 | 231.1 |
| Sm | 0.861 | 0.447 | 2.223 | 4.448 | 23.55 | 51.78 | 116.1 | 233.0 |
| Eu | 0.843 | 0.437 | 2.175 | 4.352 | 23.04 | 50.66 | 113.6 | 228.0 |
| Gd | 0.850 | 0.441 | 2.193 | 4.388 | 23.23 | 51.09 | 114.5 | 229.9 |
| Dy | 0.848 | 0.440 | 2.188 | 4.378 | 23.17 | 50.96 | 114.2 | 229.3 |
| Ho | 0.846 | 0.439 | 2.185 | 4.371 | 23.14 | 50.89 | 114.1 | 229.0 |
| Er | 0.840 | 0.436 | 2.169 | 4.339 | 22.97 | 50.51 | 113.2 | 227.3 |
| Yb | 0.854 | 0.443 | 2.204 | 4.410 | 23.34 | 51.33 | 115.1 | 231.0 |

4.2.3 Measurement runs

Three runs of measurements were performed according to the settings in **Table 4.7**. The measurement sequence for these three runs is listed in **Table 4.8**. In the second run more blanks were added in between the other samples, the flushing time was longer and more standards were introduced with lower concentrations. In the third run internal standards were added.

Table 4.7 ICP-MS operating parameters (typical).

| Parameter | Value |
|--------------------------------|---|
| RF power | 1267 W |
| Plasma/Nebulizer gas flow rate | 1.119 L/min |
| Auxiliary gas flow rate | 0.70 L/min |
| Cooling gas flow rate | 16 L/min |
| Flush time | 3 min (1 st time) / 5 min (2 nd and 3 rd time) |
| Take up time for sample | 4 min |
| Analysis time | 7 min |

Table 4.8 The measurement sequence for NiSO₄ samples in three times.

| ICP-MS No. | Exp sample No. | Sample name | No. in fig. x-axis |
|------------------------------------|----------------|--|--------------------|
| Date of analysis: 29 October 2012 | | | |
| Blank1-2 | | | 1-2 |
| S1- S4 | | Standard series 1 | 3-6 |
| S11- S14 | | Standard series 2 | 7-10 |
| S21-S24 | | Standard series 3 | 11-14 |
| Blank3-4 | | | 15-16 |
| 201 | 3 | Unwashed salt crystal | 17 |
| 202 | 12 | Salt crystal after 3 rd washing | 18 |
| 203-207 | | | 19-23 |
| Blank5 | | | 24 |
| 208-234 | | | 25-51 |
| Blank6-7 | | | 52-53 |
| 235 | 1 | Bleed stream | 54 |
| 236 | 4 | Filtered mother liquor | 55 |
| 237 | 6 | Pure saturated NiSO ₄ solution | 56 |
| 238-244 | | | 57-63 |
| Blank8-9 | | | 64-65 |
| 245-260 | | | 66-81 |
| Blank10-12 | | | 82-84 |
| Date of analysis: 22 December 2012 | | | |
| Blank 101-103 | | | 1-3 |
| S1-S11 | | | 4-14 |
| Blank104-105 | | | 15-16 |
| S21-S28 | | | 17-24 |
| Blank 106-107 | | | 25-26 |
| S31-S38 | | | 27-34 |
| Blank 108 | | | 35-36 |
| S41-S44 | | | 37-40 |
| Blank 110-113 | | | 41-44 |
| BI 01 | | 3 wt% HNO ₃ blank 1 | 45 |
| BI 02 | | 3 wt% HNO ₃ blank 2 | 46 |
| BI 03 | | 6 wt% HNO ₃ blank 1 | 47 |
| BI 04 | | 6 wt% HNO ₃ blank 2 | 48 |
| BI 05 | | 9 wt% HNO ₃ blank 1 | 49 |
| BI 06 | | 9 wt% HNO ₃ blank 2 | 50 |

Chapter 4

Table 4.8 The measurement sequence for NiSO₄ samples in three times (continued).

| | | | |
|------------------------------------|----|--|---------|
| Blank 8-11 | | | 51-54 |
| 2 | 3 | Unwashed salt crystal | 55 |
| 4 | 10 | Salt crystal after 1 st washing | 56 |
| 6 | 11 | Salt crystal after 2 nd washing | 57 |
| 8 | 12 | Salt crystal after 3 rd washing | 58 |
| 11,13,16,19,21 | | | 59-63 |
| Blank 12-15 | | | 64-67 |
| 23,25,27,31,35,37 | | | 68-73 |
| Blank 16-19 | | | 74-77 |
| 39,41,43,45,48,49,50 | | | 78-84 |
| Blank 20-23 | | | 85-88 |
| 54,56,58,60,63,67,69,71 | | | 89-96 |
| Blank 24-27 | | | 97-100 |
| 73,75,77,79,81,84,86,88,90,91 | | | 101-110 |
| Blank 28-31 | | | 111-114 |
| 93,96,98,100,102,104,106,108 | | | 115-122 |
| Blank 32-36 | | | 123-127 |
| 1 | 1 | Bleed stream | 128 |
| 3 | 4 | Filtered mother liquor | 129 |
| 5 | 16 | Filter salt washing liquor 1 | 130 |
| 7 | 17 | Filter salt washing liquor 2 | 131 |
| 9 | 18 | Filter salt washing liquor 3 | 132 |
| 10 | 6 | Pure saturated NiSO ₄ solution | 133 |
| Blank 37-40 | | | 134-137 |
| 15,20,22,28,29,30,36,38,53 | | | 138-146 |
| Blank 41-44 | | | 147-150 |
| 55,57,61,62,64,70,72,74,82 | | | 151-159 |
| Blank 45-48 | | | 160-163 |
| 113 | 9 | Ice crystal after 3 rd washing | 164 |
| 112 | 8 | Ice crystal after 2 nd washing | 165 |
| 111 | 7 | Ice crystal after 1 st washing | 166 |
| 110 | 2 | Unwashed ice crystal | 167 |
| 114 | 13 | Filtered ice washing liquor 1 | 168 |
| 115 | 14 | Filtered ice washing liquor 2 | 169 |
| 116 | 15 | Filtered ice washing liquor 3 | 170 |
| 94,103 | | | 171-172 |
| Blank 49-52 | | | 173-176 |
| 12,14,17,18,24,26,32,34 | | | 177-184 |
| Blank 53-56 | | | 185-188 |
| 40,42,44,46,47,51,52 | | | 189-195 |
| Blank 57-60 | | | 196-199 |
| 59,65,66,68,76,78,80,83,85,87,89 | | | 200-210 |
| Blank 61-64 | | | 211-214 |
| 95,97,99,101,105,107,109 | | | 215-221 |
| Blank 65-67 | | | 222-224 |
| S101-S111 | | | 225-235 |
| Blank 68-69 | | | 236-237 |
| S121-S128 | | | 238-245 |
| Blank 70-71 | | | 246-247 |
| S131-S138 | | | 248-255 |
| Date of analysis: 28 February 2013 | | | |
| Blank 01-04 | | | 1-4 |
| S101-104, S1-4 | | | 5-12 |
| S111-S114, S11-S14 | | | 13-20 |

Table 4.8 The measurement sequence for NiSO₄ samples in three times (continued).

| | | | |
|---|----|--|---------|
| S121-124, S21-24 | | | 21-28 |
| Blank 05-11 | | | 29-35 |
| 401-405 | | | 36-40 |
| Measurement stopped automatically and later was restarted | | | |
| Blank 05-11 | | | 1-7 |
| 401 | 9 | Ice crystal after 3 rd washing | 8 |
| 402 | 15 | Filtered ice washing liquor 3 | 9 |
| 403 | 8 | Ice crystal after 2 nd washing | 10 |
| 404 | 14 | Filtered ice washing liquor 2 | 11 |
| 405 | 7 | Ice crystal after 1 st washing | 12 |
| 406 | 2 | Unwashed ice crystal | 13 |
| 407 | 13 | Filtered ice washing liquor 1 | 14 |
| Blank 12-18 | | | 15-21 |
| 301 | 6 | Pure saturated NiSO ₄ solution | 22 |
| 302 | | | 23 |
| 303 | 18 | Filter salt washing liquor 3 | 24 |
| 304 | | | 25 |
| 305 | 17 | Filter salt washing liquor 2 | 26 |
| Blank 19-25 | | | 27-33 |
| 306-309 | | | 34-37 |
| 310 | 16 | Filter salt washing liquor 1 | 38 |
| Blank 26-32 | | | 39-45 |
| S1012-1042,S1002-4002 | | | 46-53 |
| S1112-1142,S11002-14002 | | | 54-61 |
| S1212-1242,S21002-24002 | | | 62-69 |
| Blank 33-39 | | | 70-76 |
| 311-314 | | | 77-80 |
| 315 | 4 | Filtered mother liquor | 81 |
| 316 | 1 | Bleed stream | 82 |
| Blank 40-46 | | | 83-89 |
| 201 | | | 90 |
| 202 | 12 | Salt crystal after 3 rd washing | 91 |
| 203 | | | 92 |
| 204 | 11 | Salt crystal after 2 nd washing | 93 |
| Blank 47-53 | | | 94-100 |
| 205 | | | 101 |
| 206 | 10 | Salt crystal after 1 st washing | 102 |
| 207, 208 | | | 103-104 |
| Blank 54-60 | | | 105-111 |
| 209 | | | 112 |
| 210 | 3 | Unwashed salt crystal | 113 |
| 211,212 | | | 114-115 |
| Blank 61-67 | | | 116-122 |
| S1013-1043,S1003-4003 | | | 123-130 |
| S 1113-1143,S11003-14003 | | | 131-138 |
| S1213-1243,S21003-24003 | | | 139-146 |
| Blank 68-73 | | | 147-152 |

4.3 Results and Discussion

4.3.1 The effect of the HNO₃ concentration on the measurements

Blanks with 3 wt%, 6 wt% and 9 wt% HNO₃ concentration were tested in order to investigate the effect of the HNO₃ concentration on the hrICP-MS analysis results. There are four effects on the isotopic content with respect to the increasing HNO₃ concentration in the blank: an increasing, decreasing, stable or varying isotopic content. **Figure 4.4** gives a visual impression of these effects for four elements.

These effects can be explained by the effect that the intensity of isotopes between the water and nitric acid used for the preparation of the blank are different. When isotope intensity increases with an increasing HNO₃ content the element content in HNO₃ is higher than in the water and vice versa. When the intensity of isotopes between the water and nitric acid are the same there will be no effect of the increasing amount of nitric acid. **Table 4.9** shows the effect of the increasing concentration of HNO₃ for the elements.

Table 4.9 Effect of HNO₃ concentration on analysis results.

| Trend (vs. HNO ₃ concentration) | Elements |
|--|--|
| Increasing | Li, Cr, Mn, Fe, Cu, Zr, Nb, Rh, Pd, Cd, Sn, Sb, Er, Lu, Hf, W, Re, Os, Bi, |
| Decreasing | Be, B, Sc, V, Co, Zn, As, Mo, Cs, Pr, Nd, Sm, Gd, Hg, |
| Stable | Ge, Se, Br, In, Te, Eu, Tb, Dy, Ho, Tm, Yb, Ta, Ir, Pt, Au, Tl, |
| Varying | Na, Mg, Al, Ca, Ti, Ga, Rb, Sr, Y, Ru, Ag, Ba, La, Ce, Pb, U |

Based upon the results it was concluded that the HNO₃ concentration has an effect on the hrICP-MS measuring results but this effect is minor. If the impurities originated from the nitric acid, the signal would increase markedly when increasing the nitric acid concentration from 3 to 6 to 9%. This proves that the nitric acid is not more than water a source of impurities.

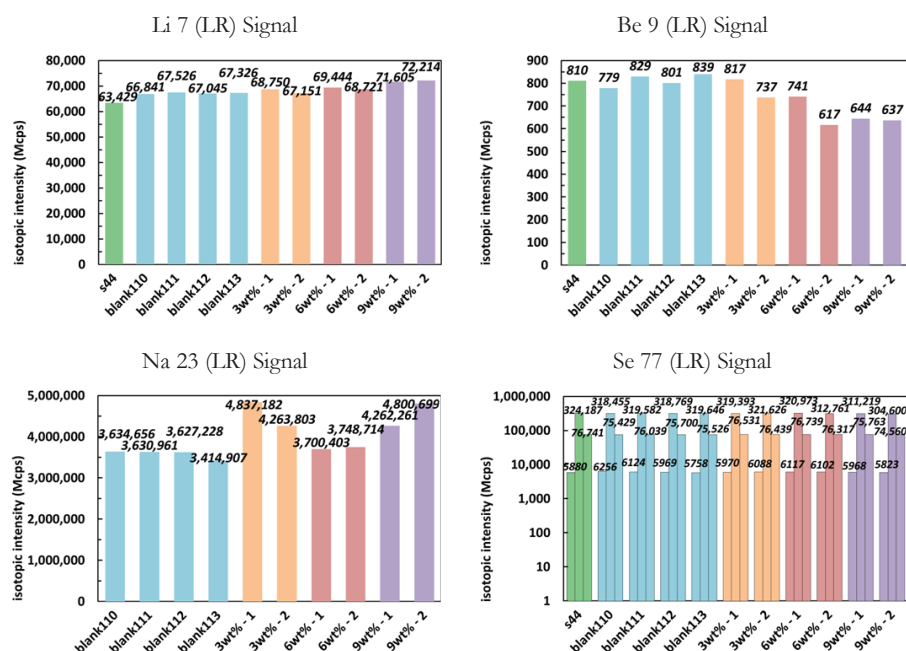


Figure 4.4 Impact of the increasing concentration of HNO₃ on the signal for four elements.

4.3.2 Diminishing the memory effect

If the first sample to be analyzed contains a much higher concentration of a certain element than the subsequent sample a carry-over might occur of residues from the first sample. This is named the memory effect.

Figure 4.5 shows a typical example of the memory effect with respect to the element Be in the first run. The last standard of the first standard series contains the highest element content. The following samples of the second standard series contain less of this element. Sample No. 6 is the last sample of the first series and contains 1000 ppb Be. Three minutes washing by the blank after sample No. 6 removed 99 wt% of Be, the remaining 1% Be ended up in sample 7. This is the memory effect. Further washing by the blanks until sample 14, gradually decreased the memory effect of Be to below the detection limit. So by washing long enough the memory effect can be completely eliminated.

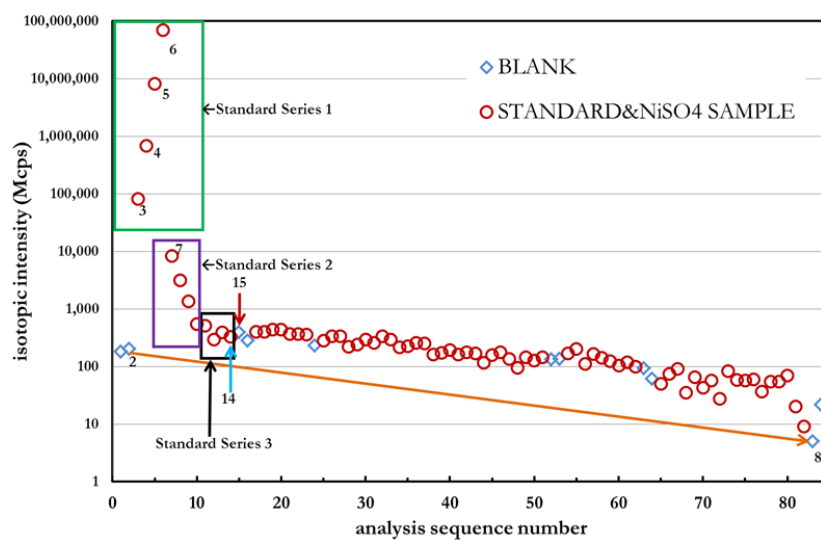


Figure 4.5 Memory effect in run 1; The highest standard (No. 6) contains 1000 ppb Be.

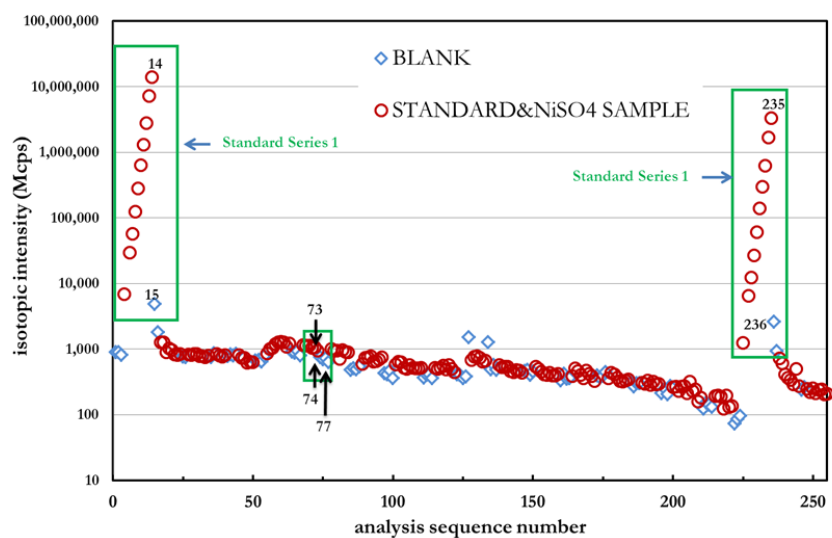


Figure 4.6 Memory effect in run 2; The highest standard (No. 14) contains 1000 ppb Be.

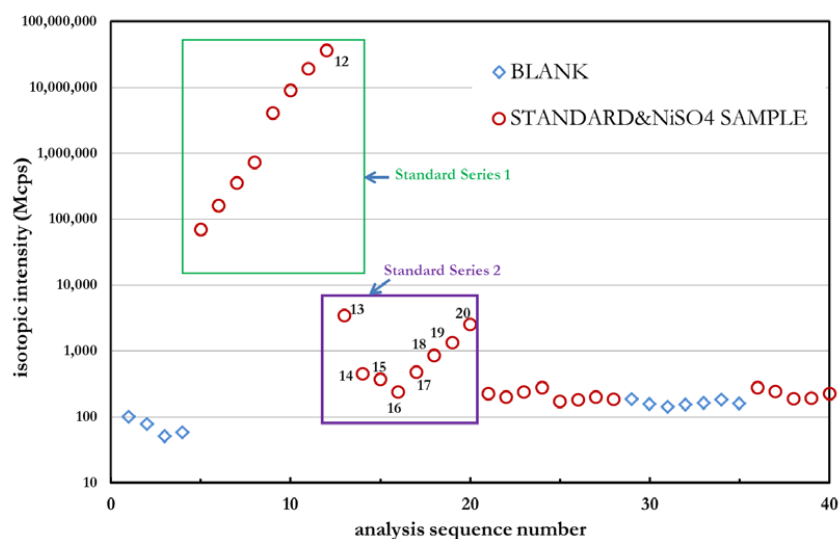


Figure 4.7. Memory effect in run 3; The highest standard contains 2500 ppb Be.

In order to diminish the memory effect to a tolerable level run 2 and 3 were performed with prolonged flushing with blank solution. Figures 4.6 and 4.7 show that in run 2 and 3 the memory effect is largely eliminated.

4.3.3 Corrections for signal decline

Signal decline in time is an unwanted phenomenon but cannot always be prevented completely. Origins of signal decline can be fouling along the line of analysis, or change in the equipment or in the environment. Figure 4.6 shows a gradual decline in element intensity of the blanks as function of the sequence number. It is signal decline. This agrees with the decline in signal of the samples and the standard solutions. The origin of signal decline is often difficult to find. In order to investigate signal decline and to possibly improve the accuracy of the measurements an internal standard (In115) was added to all the blanks, standards and samples in run 2 and 3. In run 3 next to In 115, Sc 45 and Y 89 were also used as internal standards. An example of the calibration curve for Li (7) with internal standard at the start of the run (green line) and at the end of the run (blue line) is presented in Figure 4.8.

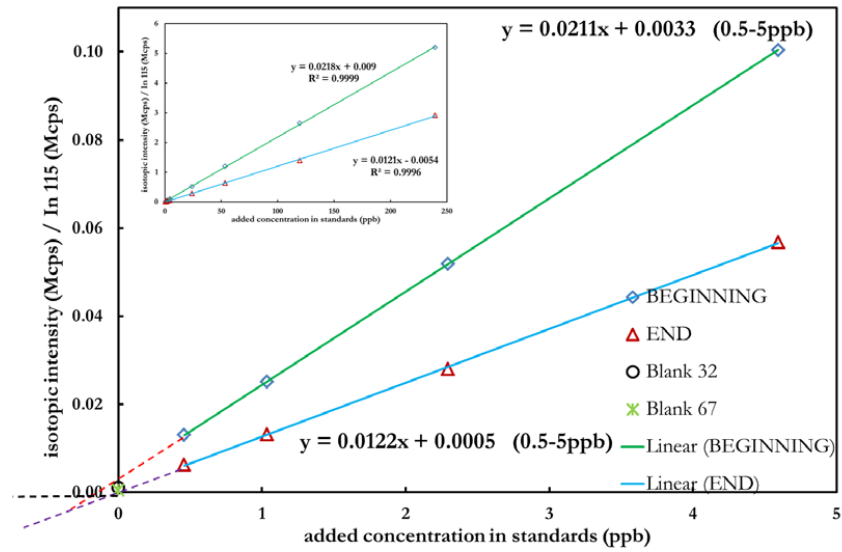


Figure 4.8. Calibration curves for Li (7) at the start (green line) and at the end of the run (blue line).

Sample correction calculation:

$$\text{intensity of sample(corrected)} = (\text{intensity of sample}) / (\text{intensity of In(115)}^*)$$

The signal decline effects for the different elements are collected in **Table 4.10**. The table shows the percentage of the starting signal that remains at the end of the run.

Run 2 signal decline without internal standard (IS): $\Delta_{2nd}^{2nd} = \frac{\text{signal (end)}}{\text{signal (beginning)}} \times 100\%$

Run 3 signal decline without IS: Δ_1^{3rd} ; with IS In115: Δ_2^{3rd} ; with IS Sc45: Δ_3^{3rd} ; with IS Y89: Δ_4^{3rd} .

Table 4.10 Percentage of the starting signal that remains at the end of the run for each element and for run 2 and 3. In the third run three different internal standards were used.

| | Δ_{2nd}^{2nd} | Δ_1^{3rd} | Δ_2^{3rd} | Δ_3^{3rd} | Δ_4^{3rd} |
|----|----------------------|------------------|------------------|------------------|------------------|
| Li | 4-28 | 55-67 | 48-57 | 74-82 | 50-56 |
| B | 16-19 | 73-85 | 64-72 | 98-107 | 66-71 |
| | 11-27 | 60-70 | 53-59 | 81-86 | 54-58 |
| Na | 33-42 | 75-103 | 63-90 | 96-135 | 63-91 |
| Mg | 18-28 | 78-86 | 69-72 | 104-110 | 69-73 |
| | 18-25 | 86-96 | 78-82 | 116-124 | 78-83 |
| | 17-22 | 96-106 | 84-89 | 127-133 | 84-90 |
| Al | 7-29 | 65-74 | 58-62 | 88-93 | 59-62 |
| K | 19-39 | 72-78 | 58-65 | 89-102 | 61-69 |
| Ca | 16-35 | 65-75 | 72-77 | 89-97 | 60-66 |
| La | 52-56 | 88-92 | 72-77 | 112-120 | 72-79 |
| Ce | 53-57 | 88-96 | 76-81 | 114-124 | 75-82 |
| Pr | 53-58 | 94-101 | 80-85 | 119-128 | 78-85 |

Table 4.10 Percentage of the starting signal that remains at the end of the run for each element and for run 2 and 3. In the third run three different internal standards were used (continued).

| | | | | | |
|----|--------|---------|---------|---------|----------|
| Nd | 52-58 | 102-107 | 87-90 | 131-127 | 86-90 |
| | 52-53 | 105-114 | 89-94 | 137-143 | 89-96 |
| | 50-55 | 110-115 | 93-97 | 139-147 | 91-98 |
| Sm | 48-56 | 111-119 | 95-100 | 141-163 | 92-101 |
| | 47-54 | 117-122 | 100-104 | 149-163 | 98-104 |
| | 46-48 | 118-128 | 101-105 | 150-165 | 98-107 |
| Eu | 46-50 | 122-128 | 104-107 | 154-164 | 102-107 |
| | 44-48 | 123-130 | 105-111 | 159-168 | 1106-110 |
| Gd | 42-49 | 115-124 | 97-105 | 148-158 | 98-105 |
| | 43-46 | 119-128 | 101-109 | 151-165 | 99-109 |
| | 41-47 | 121-130 | 103-110 | 155-173 | 104-110 |
| | 39-43 | 123-130 | 106-111 | 160-171 | 105-111 |
| Dy | 59-64 | 96-104 | 83-88 | 125-132 | 82-87 |
| | 59-64 | 101-106 | 85-90 | 129-137 | 86-90 |
| | 59-64 | 104-107 | 88-91 | 132-142 | 87-91 |
| Ho | 58-63 | 220-116 | 92-97 | 137-150 | 90-98 |
| Er | 56-62 | 111-117 | 94-99 | 142-154 | 93-102 |
| | 56-60 | 115-120 | 98-101 | 147-156 | 96-103 |
| | 56-60 | 114-122 | 97-103 | 145-159 | 95-104 |
| Yb | 51-61 | 121-131 | 103-108 | 155-163 | 103-110 |
| | 51-56 | 122-130 | 104-111 | 157-172 | 103-110 |
| | 47-56 | 125-132 | 106-110 | 159-170 | 104-111 |
| | 48-54 | 127-133 | 107-112 | 160-175 | 105-112 |
| Sc | 26-33 | 73-81 | 63-67 | 100 | - |
| Ti | 29-34 | 68-83 | 59-72 | 94-105 | - |
| | 11-29 | 77-89 | 67-76 | 104-115 | - |
| | 25-27 | 74-102 | 66-87 | 101-131 | - |
| Ge | 36-39 | 82-88 | 70-77 | 106-118 | - |
| | 35-46 | 92-168 | 78-149 | 117-228 | - |
| | 28-46 | 93-126 | 82-112 | 124-171 | - |
| | 33-236 | 106-251 | 88-223 | 132-341 | - |
| Y | 31-33 | 110-121 | 96-104 | 148-157 | - |
| Zr | 30-32 | 113-121 | 99-108 | 145-164 | - |
| | 41-45 | 75-82 | 67-79 | 101-121 | - |
| Nb | 39-41 | 78-87 | 69-73 | 107-111 | - |
| Rh | 31-32 | 112-119 | 97-104 | 147-154 | - |
| Pd | 31-45 | 63-82 | 55-69 | 86-103 | - |
| | 32-45 | 63-88 | 54-73 | 86-109 | - |
| Sn | 32-37 | 96-122 | 85-106 | 130-159 | - |
| | 31-37 | 103-127 | 92-107 | 140-163 | - |
| | 19-34 | 109-128 | 94-106 | 149-161 | - |
| | 30-35 | 107-128 | 95-109 | 145-164 | - |
| Sb | 42-51 | 84-93 | 73-79 | 114-117 | - |
| | 49-51 | 89-100 | 79-83 | 121-127 | - |
| Hf | 44-48 | 130-138 | 114-123 | 163-188 | - |
| | 44-46 | 132-139 | 113-122 | 171-186 | - |
| | 43-46 | 132-140 | 114-124 | 170-190 | - |
| | 42-44 | 131-136 | 112-120 | 166-184 | - |
| Lu | 47-52 | 127-134 | 110-116 | 165-178 | - |
| W | 39-42 | 124-132 | 109-117 | 156-179 | - |
| | 39-43 | 126-132 | 108-117 | 161-179 | - |
| | 59-62 | 95-106 | 84-88 | 129-134 | - |
| | 60-62 | 102-110 | 88-92 | 132-142 | - |
| Pt | 52-54 | 110-123 | 96-102 | 149-157 | - |
| | 52-53 | 113-124 | 100-103 | 150-161 | - |
| | 51-57 | 115-127 | 100-105 | 156-160 | - |
| Au | 24-104 | 36-121 | 33-100 | 66-149 | - |

Table 4.10 Percentage of the starting signal that remains at the end of the run for each element and for run 2 and 3. In the third run three different internal standards were used (continued).

| | | | | | |
|----|--------|---------|---------|---------|---------|
| Hg | 11-52 | 35-136 | 32-113 | 48-173 | - |
| | 13-51 | 40-132 | 35-110 | 54-170 | |
| | 9-49 | 34-136 | 30-116 | 46-175 | |
| | 12-48 | 39-136 | 35-115 | 53-176 | |
| Be | 18-24 | 55-64 | 50-54 | 76-79 | 50-53 |
| V | 24-32 | 65-75 | 59-63 | 87-92 | 59-62 |
| Cr | 18-31 | 98-113 | 60-68 | 91-102 | 61-68 |
| | 21-31 | 67-81 | 66-72 | 101-108 | 68-71 |
| Mn | 20-30 | 93-105 | 84-88 | 125-132 | 84-87 |
| Fe | 15-27 | 96-115 | 84-96 | 137-143 | 76-81 |
| Co | 25-33 | 65-76 | 58-64 | 88-95 | 59-63 |
| Cu | 14-31 | 74-94 | 62-79 | 100-119 | 67-78 |
| | 14-29 | 88-103 | 78-87 | 119-132 | 80-86 |
| Zn | 22-30 | 105-118 | 93-102 | 141-150 | 95-103 |
| | 21-26 | 110-119 | 93-100 | 142-151 | 96-101 |
| | 26-40 | 71-81 | 63-72 | 96-107 | 64-73 |
| Ga | 25-39 | 81-87 | 69-74 | 105-110 | 69-74 |
| | 29-39 | 88-99 | 78-83 | 117-124 | 79-82 |
| As | 29-392 | 102-164 | 89-145 | 134-222 | 89-149 |
| Se | 29-233 | 112-351 | 99-311 | 148-476 | 98-320 |
| | 24-28 | 113-158 | 98-113 | 151-174 | 98-117 |
| | 34-39 | 88-99 | 71-88 | 116-134 | 77-90 |
| Rb | 33-36 | 99-107 | 86-90 | 130-139 | 87-92 |
| Sr | 31-35 | 105-115 | 93-97 | 140-147 | 94-97 |
| | 27-32 | 105-123 | 93-103 | 143-157 | 96-102 |
| Mo | 34-38 | 78-97 | 69-82 | 106-124 | 71-81 |
| | 34-38 | 92-108 | 80-91 | 124-131 | 81-89 |
| Ag | 26-46 | 84-90 | 74-80 | 110-118 | 75-81 |
| | 27-45 | 89-97 | 80-88 | 118-125 | 80-89 |
| Cd | 32-43 | 102-110 | 90-95 | 134-141 | 90-94 |
| | 28-44 | 103-114 | 91-96 | 139-146 | 94-99 |
| | 26-42 | 111-119 | 96-104 | 145-154 | 96-103 |
| Te | 31-48 | 96-104 | 83-91 | 125-134 | 83-90 |
| | 42-47 | 98-106 | 85-91 | 127-136 | 84-91 |
| | 44-48 | 104-111 | 90-97 | 134-149 | 90-100 |
| | 43-47 | 109-124 | 97-110 | 141-168 | 97-113 |
| Ba | 33-39 | 112-127 | 101-107 | 153-160 | 101-105 |
| | 38-42 | 113-138 | 102-122 | 154-187 | 103-126 |
| | 29-37 | 116-125 | 102-106 | 154-162 | 103-107 |
| | 28-36 | 115-129 | 102-108 | 154-161 | 103-107 |
| Tl | 48-57 | 123-132 | 109-114 | 157-172 | 107-116 |
| | 45-52 | 122-133 | 110-114 | 161-175 | 109-118 |
| Pb | 27-52 | 120-133 | 106-115 | 161-171 | 109-113 |
| | 25-51 | 122-131 | 106-112 | 159-171 | 108-114 |
| | 25-48 | 120-133 | 105-115 | 159-171 | 109-114 |
| Bi | 442-49 | 122-134 | 110-115 | 160-173 | 110-115 |
| U | 70-76 | 105-114 | 92-98 | 138-145 | 93-99 |

Table 4.10 shows that with the use of internal standards signal decline remains within 50% of the measured value at the starting point. The table also shows that the internal standard compensates better for signal decline when the atomic mass of the element to be determined is close to the mass of the internal standard. The physical meaning for this effect is unclear. Because the internal standard gives different results with different elements the main conclusion was that use of internal standards did not result in an improvement.

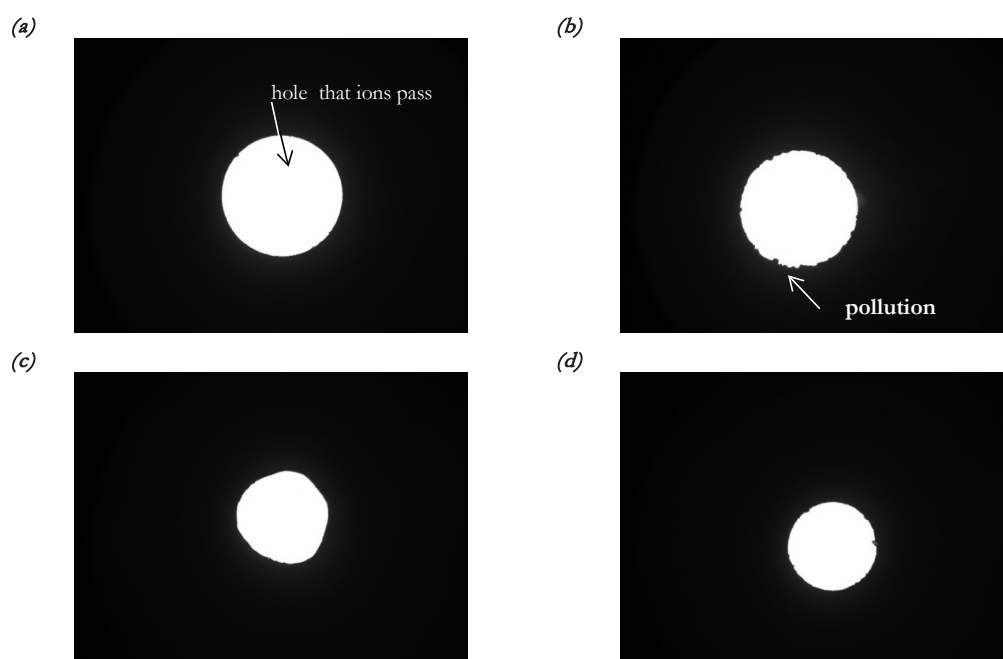


Figure 4.9 Photos of the central hole in the sampler and skimmer cones in the interface.

(a): Clean sampler cone.

(b): Contaminated sampler cone.

(c): Damaged Skimmer cone

(d): Contaminated skimmer cone

A possible origin of the signal decline for the experiments was gradual pollution of sampler / skimmer cones in the interface part. **Figure 4.9** shows photos of polluted cones taken after the analytical runs. The photos show only minor pollution meaning that pollution of the cones is not an explanation for signal decline.

4.3.4 Determination of elements present in the blanks

The elements present in the blanks are presented in **Table 4.11**. The element concentration was determined by adding different amounts of standard solution (standard addition). The added standard amounts ranged from the lowest (0.5ppb) to 1ppb, 10ppb and 100 ppb.

Table 4.11 Element content of the blanks (unit: ppb), calculated from different added standards results.

| element | Run 1 st | Run 2 nd | | | Run 3 rd | | | |
|---------|---------------------|---------------------|--------------|--------------|---------------------|---------------|-----------------|----------------|
| | | Beginning | | | beginning | | end | |
| | | ~1ppb | ~10ppb | ~100ppb | Without /In 115 | With /In 115 | Without /In 115 | With /In 115 |
| Li | 3.63 5.70 | 1.04 | 1.06 | 1.07 | -1.46 | 0.414 | -0.153 | -0.446 |
| B | 0.19 5.10 | 204 44.3 | 53.3 23.3 | 23.5 15.3 | -5.06 -20.1 | -4.79 9.17 | -9.31 1.10 | -12.1 -1.89 |
| Na | 75.0 | -6.67 | 24.3 | 36.0 | -28.3 | 25.1 | 33.2 | 31.9 |

Table 4.11 Element content of the blanks (unit: ppb), calculated from different added standards results (continued).

| | | | | | | | | |
|----|------|--------|--------|--------|--------|-------|--------|-------|
| Mg | 8.30 | 2.74 | 1.71 | 1.71 | -3.24 | 2.03 | 1.86 | 1.51 |
| | 12.5 | 2.49 | 1.68 | 1.76 | -2.94 | 1.73 | 1.55 | 1.20 |
| | 12.3 | 2.32 | 1.65 | 1.72 | -3.31 | 2.09 | 1.67 | 1.32 |
| Al | 10.5 | 2.75 | 4.20 | 4.45 | -5.30 | 3.92 | 3.48 | 3.07 |
| K | 50.1 | -4.37 | 44.3 | 68.1 | -33.4 | 29.8 | 34.1 | 32.8 |
| Ca | 5.96 | 40.4 | 24.4 | 23.4 | -136 | 28.2 | 5.84 | -24.6 |
| La | 5.53 | -0.005 | -0.044 | 0.122 | -1.07 | 1.53 | 1.41 | 1.48 |
| Ce | 5.42 | -0.004 | -0.044 | 0.139 | -1.12 | 1.60 | 1.60 | 1.68 |
| Pr | 5.53 | -0.004 | -0.033 | 0.178 | -0.870 | 1.33 | 1.47 | 1.55 |
| Nd | 6.74 | -0.006 | -0.027 | 0.167 | -0.575 | 1.03 | 1.04 | 1.11 |
| | 5.37 | -0.004 | -0.019 | -0.080 | -0.758 | 1.21 | 1.28 | 1.36 |
| | | -0.002 | -0.023 | 0.168 | -0.641 | 1.10 | 1.14 | 1.22 |
| Sm | 5.40 | -0.005 | -0.028 | 0.203 | -0.834 | 1.30 | 1.17 | 1.25 |
| | 6.41 | -0.009 | -0.021 | 0.211 | -1.34 | 1.82 | 1.12 | 1.19 |
| | 5.27 | -0.006 | -0.017 | 0.223 | -0.880 | 1.35 | 1.30 | 1.38 |
| Eu | 5.36 | -0.004 | -0.032 | 0.224 | -1.04 | 1.51 | 1.03 | 1.11 |
| | 5.59 | -0.003 | -0.039 | 0.283 | -0.897 | 1.35 | 1.12 | 1.20 |
| | | | | | | | | |
| Gd | 5.70 | -0.004 | -0.010 | 0.185 | -0.142 | 0.58 | 0.10 | 0.17 |
| | 5.54 | -0.009 | -0.026 | 0.207 | -0.611 | 1.07 | 0.86 | 0.93 |
| | 5.48 | -0.003 | -0.023 | 0.242 | -1.03 | 1.50 | 0.82 | 0.902 |
| | 5.49 | -0.010 | -0.030 | 0.242 | -1.00 | 1.47 | 1.61 | 1.69 |
| Dy | 5.27 | -0.003 | -0.024 | 0.227 | -0.337 | 0.78 | 1.36 | 1.44 |
| | 5.87 | -0.006 | -0.027 | 0.225 | -1.08 | 1.54 | 1.49 | 1.56 |
| | 5.63 | -0.003 | -0.034 | 0.224 | -1.73 | 2.21 | 1.54 | 1.62 |
| Er | 5.53 | -0.006 | -0.028 | 0.280 | -1.16 | 1.63 | 1.45 | 1.52 |
| | 6.08 | -0.007 | -0.030 | 0.273 | -0.922 | 1.38 | 1.37 | 1.44 |
| | 5.47 | -0.006 | -0.030 | 0.274 | -0.542 | 0.993 | 1.40 | 1.47 |
| Yb | 5.20 | -0.006 | -0.024 | 0.293 | -1.30 | 1.78 | 1.95 | 2.03 |
| | 6.07 | -0.005 | -0.025 | 0.306 | -1.55 | 2.03 | 1.18 | 1.25 |
| | 5.86 | -0.005 | -0.106 | 0.452 | -1.33 | 1.81 | 1.54 | 1.61 |
| | 5.67 | -0.004 | -0.069 | 0.405 | -1.45 | 1.93 | 1.29 | 1.37 |
| Ho | 5.61 | -0.004 | 0.021 | 0.208 | -1.31 | 1.78 | 1.49 | 1.56 |
| Sc | 2.13 | 0.060 | 0.018 | -0.388 | -10.5 | 11.1 | 8.73 | 10.5 |
| Ti | 0.95 | 0.569 | 0.480 | 0.288 | -0.259 | 0.568 | -0.255 | 0.759 |
| | 0.92 | 0.604 | 0.497 | 0.289 | -0.205 | 0.509 | -0.593 | 0.388 |
| | 1.38 | 0.108 | 0.063 | -0.067 | -0.225 | 0.530 | -0.408 | 0.589 |
| Ge | 5.88 | 0.225 | 0.186 | 0.051 | -1.46 | 1.77 | 0.252 | 1.26 |
| | 6.34 | 0.256 | 0.218 | 0.050 | -1.12 | 1.43 | 1.05 | 2.11 |
| | 5.92 | 0.034 | -0.005 | -0.112 | -0.244 | 0.541 | -0.266 | 0.727 |
| | | 0.050 | 0.024 | 0.005 | -1.17 | 1.49 | 2.02 | 3.17 |
| Y | 4.04 | 0.001 | -0.043 | -0.198 | -11.9 | 12.6 | 10.7 | 12.8 |
| Zr | 3.73 | 0.015 | -0.014 | -0.206 | -0.337 | 0.632 | 0.248 | 1.22 |
| | 2.65 | 0.019 | -0.016 | -0.172 | 0.058 | 0.233 | -0.841 | 0.09 |
| Nb | 4.26 | 0.006 | -0.046 | -0.189 | -0.587 | 0.895 | -0.152 | 0.84 |
| Rh | 5.17 | 0.003 | -0.037 | -0.035 | -1.06 | 1.37 | 0.419 | 1.43 |
| Pd | 1.94 | 0.010 | -0.081 | -0.195 | -1.26 | 1.58 | 0.174 | 1.20 |
| | 1.87 | 0.002 | -0.103 | -0.221 | -1.11 | 1.42 | -0.447 | 0.52 |
| Sn | 6.40 | 0.063 | 0.032 | -0.103 | -1.38 | 1.72 | 1.22 | 2.36 |
| | 3.33 | 0.059 | 0.037 | 0.035 | -1.53 | 1.87 | 0.834 | 1.96 |
| | 6.78 | 0.190 | 0.149 | 0.032 | -1.93 | 2.28 | 0.986 | 2.11 |
| | 3.91 | 0.059 | 0.016 | 0.081 | -1.37 | 1.71 | 0.447 | 1.57 |
| Sb | 4.05 | 0.037 | 0.011 | -0.047 | -0.895 | 1.20 | 0.075 | 1.08 |
| | 6.53 | 0.005 | -0.018 | -0.028 | -0.903 | 1.21 | 0.036 | 1.05 |
| Hf | 3.73 | -0.003 | -0.040 | 0.020 | -1.14 | 1.46 | 0.449 | 1.50 |
| | 3.26 | -0.007 | -0.042 | 0.009 | -1.06 | 1.37 | 0.370 | 1.43 |
| | 3.08 | -0.006 | -0.040 | 0.002 | -1.21 | 1.54 | 0.908 | 1.98 |
| | 5.06 | -0.006 | -0.042 | 0.018 | -1.00 | 1.31 | 0.866 | 1.94 |

Table 4.11 Element content of the blanks (unit: ppb), calculated from different added standards results (continued).

| | | | | | | | | |
|----|-------|-------|--------|--------|--------|--------|--------|--------|
| Lu | 4.81 | 0.001 | 0.069 | -0.057 | -0.717 | 1.02 | 0.441 | 1.47 |
| W | 3.68 | 0.003 | -0.022 | 0.032 | -1.00 | 1.31 | 0.321 | 1.34 |
| | 3.98 | 0.001 | -0.026 | 0.066 | -1.15 | 1.47 | 1.16 | 2.22 |
| | 4.19 | 0.007 | -0.035 | 0.007 | -0.94 | 1.25 | 0.103 | 1.11 |
| | 3.84 | 0.005 | -0.035 | 0.007 | -0.99 | 1.29 | 0.165 | 1.18 |
| Pt | 3.58 | 0.008 | -0.029 | 0.055 | -1.44 | 1.76 | 0.471 | 1.54 |
| | 4.43 | 0.007 | -0.027 | 0.075 | -1.28 | 1.60 | 0.462 | 1.53 |
| | 3.77 | 0.007 | -0.037 | 0.095 | -1.92 | 2.25 | 0.935 | 2.02 |
| Au | -1.66 | 0.392 | -0.463 | -2.68 | 8.49 | -13.1 | -20.5 | -20.3 |
| Hg | 9.56 | 0.058 | -0.257 | -0.340 | -0.133 | 0.436 | -1.12 | -0.190 |
| | 6.83 | 0.051 | -0.252 | -0.335 | -1.67 | 1.98 | 0.817 | 1.83 |
| | 7.00 | 0.058 | -0.264 | -0.338 | 0.178 | 0.121 | -0.993 | -0.054 |
| | 6.55 | 0.047 | -0.257 | -0.393 | -1.77 | 2.09 | 0.936 | 1.95 |
| Be | 5.64 | 0.019 | -0.384 | -1.15 | -15.4 | 4.65 | -5.57 | -8.53 |
| V | 4.47 | 0.010 | -0.021 | -0.252 | -1.08 | 0.039 | -0.894 | -1.17 |
| Cr | 6.51 | 2.233 | 1.79 | 1.47 | -2.31 | 1.11 | 0.241 | -0.086 |
| | 4.82 | 0.199 | 0.164 | 0.203 | -0.969 | -0.154 | -0.368 | -0.684 |
| Mn | 5.66 | 0.095 | 0.056 | -0.010 | -1.62 | 0.523 | 0.015 | -0.288 |
| Fe | | 150 | 75.0 | 66.9 | -50.3 | 36.9 | 28.0 | 24.3 |
| Co | 6.81 | 0.024 | -0.014 | 0.081 | -1.47 | 0.373 | -0.146 | -0.451 |
| Cu | 11.3 | 2.52 | 2.30 | 2.61 | -3.76 | 2.48 | 2.000 | 1.63 |
| | 18.7 | 2.40 | 2.28 | 2.72 | -4.25 | 2.93 | 2.710 | 2.351 |
| Zn | 10.3 | 2.34 | 1.80 | 5.08 | -24.9 | 13.3 | 12.8 | 9.49 |
| | 10.1 | 2.37 | 1.97 | 2.17 | -32.1 | 20.4 | 20.3 | 17.0 |
| | | 2.44 | 1.99 | 7.09 | -20.9 | 9.63 | 9.98 | 6.685 |
| Ga | 8.67 | 0.017 | -0.008 | 0.237 | -1.96 | 0.846 | 0.423 | 0.108 |
| | 6.45 | 0.001 | -0.019 | 0.220 | -2.46 | 1.30 | 0.686 | 0.367 |
| As | 5.57 | 0 | -0.413 | 0.403 | -10.7 | 0.023 | 2.34 | -0.790 |
| Se | 12.0 | 3.86 | 3.29 | 4.18 | -13.6 | 2.69 | 8.91 | 5.63 |
| | | 65.5 | 54.8 | 57.4 | -39.2 | 26.5 | 24.4 | 20.8 |
| | | 36.6 | 32.7 | 33.0 | -15.4 | 4.44 | 2.47 | -0.615 |
| Rb | 5.90 | 0.068 | 0.025 | 0.054 | -0.761 | -0.255 | -0.096 | -0.385 |
| Sr | 5.50 | 6.23 | 4.39 | 4.31 | -1.15 | 0.065 | -0.212 | -0.517 |
| | 5.19 | 0.329 | 0.180 | 0.195 | -1.24 | 0.145 | -0.030 | -0.336 |
| Mo | 4.94 | 0.009 | -0.014 | -0.106 | -0.727 | -0.330 | -0.545 | -0.841 |
| | | 0.016 | 0.004 | -0.084 | -1.63 | 0.542 | -0.433 | -0.730 |
| Ag | 8.93 | 0.021 | -0.024 | 0.277 | -1.68 | 0.570 | 0.894 | 0.570 |
| | 8.36 | 0.019 | -0.013 | 0.366 | -1.76 | 0.657 | 0.953 | 0.626 |
| Cd | 11.5 | 0.016 | -0.011 | 0.035 | -2.50 | 1.36 | 1.46 | 1.14 |
| | 12.3 | 0.033 | 0.020 | 0.493 | -2.15 | 0.999 | 1.06 | 0.751 |
| | 6.51 | 0.050 | 0.016 | 0.573 | -2.01 | 0.869 | 1.01 | 0.702 |
| Te | 12.8 | 0.014 | 0.000 | 0.145 | -1.56 | 0.460 | 0.310 | 0.001 |
| | 11.5 | 0.178 | 0.149 | 0.181 | -1.02 | -0.049 | 0.103 | -0.204 |
| | 11.7 | 2.35 | 2.02 | 2.001 | -2.05 | 0.938 | 1.35 | 1.03 |
| | | 4.49 | 4.01 | 4.03 | -2.42 | 1.28 | 1.79 | 1.47 |
| Ba | 6.33 | 0.088 | 0.077 | 0.016 | -1.85 | 0.731 | 0.221 | -0.089 |
| | 7.56 | 14.0 | 9.86 | 9.71 | -1.65 | 0.533 | 0.658 | 0.344 |
| | 5.88 | 0.091 | 0.069 | 0.185 | -1.54 | 0.423 | 0.658 | 0.345 |
| | | 0.074 | 0.041 | 0.056 | -1.53 | 0.425 | 0.060 | -0.249 |
| Tl | 7.45 | 0.005 | -0.037 | 0.531 | -1.18 | 0.074 | 0.955 | 0.624 |
| | 8.61 | 0.006 | -0.043 | 0.356 | -1.52 | 0.424 | 0.662 | 0.350 |
| Pb | 8.35 | 0.241 | 0.308 | 0.844 | -2.54 | 1.37 | 1.71 | 1.37 |
| | 8.78 | 0.245 | 0.313 | 0.862 | -2.61 | 1.44 | 1.95 | 1.62 |
| | 10.5 | 0.248 | 0.285 | 0.725 | -2.07 | 0.952 | 1.09 | 0.769 |
| Bi | 11.5 | 0.007 | -0.047 | 0.404 | -1.91 | 0.781 | 1.17 | 0.846 |
| U | 5.77 | 0.005 | 0.011 | 0.119 | -0.89 | -0.159 | 0.106 | -0.198 |

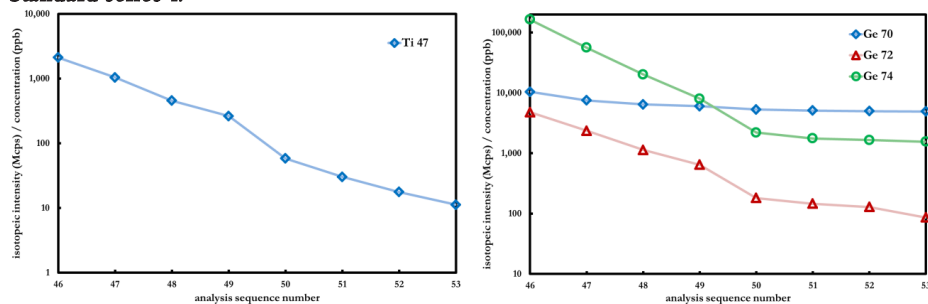
4.3.5 Determination of foreign elements present in the standards

Next to the blanks, also the standards may contain element impurities. The impurity content of the standards was determined as follows. In the measurement series of standards containing the same elements, the concentration of the standard was stepwise increased. If the standard contained a foreign element the concentration of this foreign element would also increase stepwise. When the ratio between the isotopic intensity of the contamination and the concentration of the standard is plotted against the sample number, a horizontal line between the samples will be the result when the contamination is present in the standard (**Figure 4.10** Ge70). A declining line indicates that the contamination of the standard solution with the foreign element is caused by the memory effect and/or by the presence of the foreign element in the blank (**Figure 4.10** Li7, Ti47, Au197). An initially declining line that becomes horizontal indicates that the memory effect of previous samples causes the initial decline and the horizontal part is indicative for contamination of the standard with the foreign element (**Figure 4.10** Ge74, Ag107, Ag109). The concentration of the foreign elements present in the standard series is collected in **Table 4.12**.

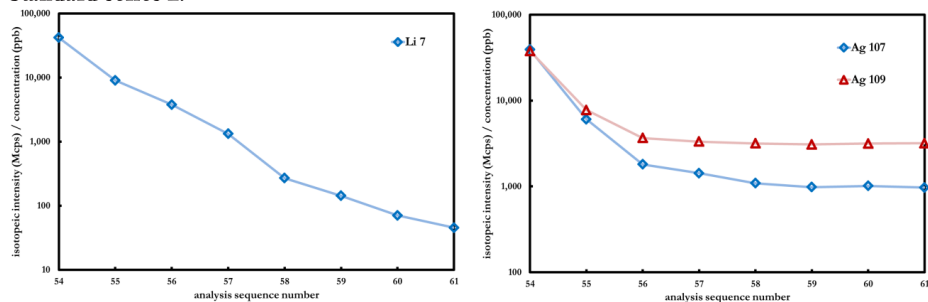
Table 4.12 Concentration of foreign elements present in the standard series (after dilution, unit: ppb).

| element | Standard Series 1 | Standard Series2 | Standard Series 3 |
|---------|-------------------|------------------|-------------------|
| K | | 2600 | |
| V | | 0.4 | |
| Cr | | 2 | |
| Ga | | | 8 |
| Ge | 50 | | 20 |
| Zr | 4 | | |
| Nb | 0.5 | | |
| Mo | | 0.2 | |
| Rh | 0.6 | | |
| Pd | 5 | | |
| Ag | | 4 | |
| Cd | | 8 | |
| Sn | 40 | | |
| Sb | 3.5 | | |
| Ba | | 0.7 | |
| La | | 1.5 | |
| Sm | 1.8 | | |
| Eu | 1 | | |
| Gd | 1 | | |
| Lu | | | 0.2 |
| Hf | | | 1 |
| W | | | 1 |

Standard series 1:



Standard series 2:



Standard series 3:

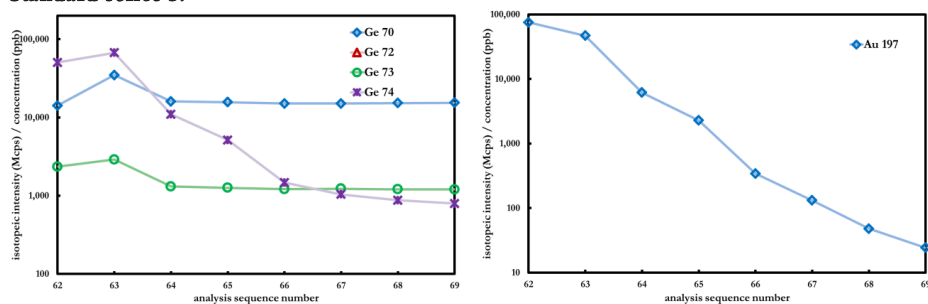


Figure 4.10 Isotopic intensity of foreign elements divided by the standard concentration as a function of standard sample number.

4.3.6 Determination of the composition of the NiSO_4 samples

Figures 4.11-4.13 show for 3 elements how the composition of the NiSO_4 samples was determined. The two dotted pink lines are the calibration curves for the element at the beginning and end of the run. The green dotted lines represent lines of equal concentration at different sequence numbers (runtimes) and are drawn between the equal concentration points on both calibration curves. The concentrations in each NiSO_4 sample were read directly from the green lines indicating the concentrations of the element in the standards. The results were used in the previous chapters.

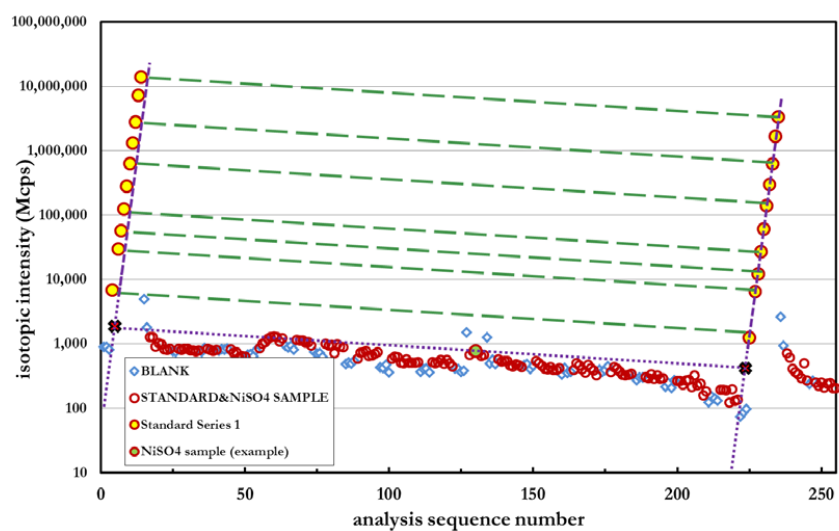


Figure 4.11 Determination of the Be content in the sample.

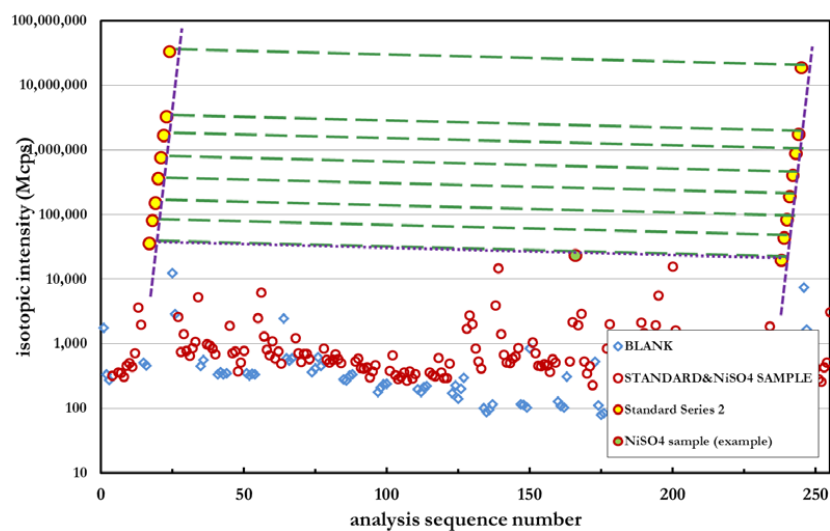


Figure 4.12 Determination of the La content in the sample.

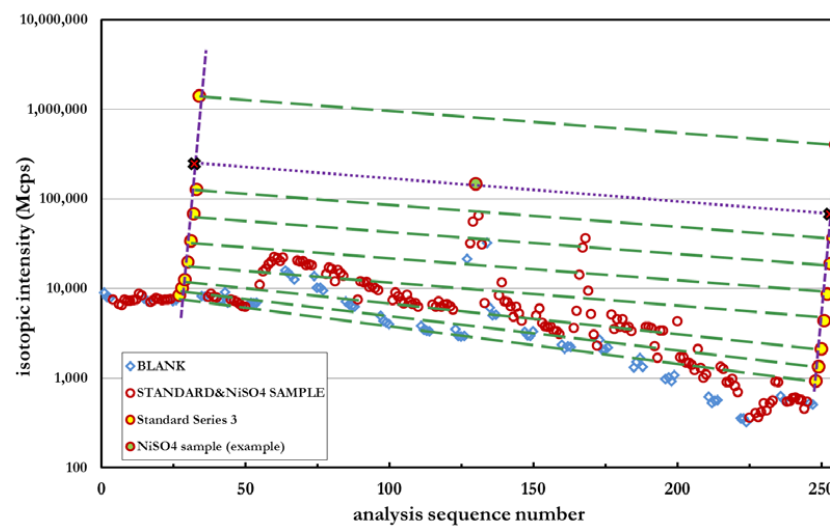


Figure 4.13 Determination of the Ti content in the sample.

4.4 Conclusions

1. HNO_3 concentration has an effect on the hrICP-MS measuring results by analysis of 3 wt%, 6 wt% and 9 wt% HNO_3 content blanks, but this effect is minor. Based upon the results it was concluded that the HNO_3 concentration has an effect on the hrICP-MS measuring results but this effect is minor. If the impurities originated from the nitric acid, the signal would increase markedly when increasing the nitric acid concentration from 3 to 6 to 9%. This proves that the nitric acid is not more than water a source of impurities. We can easily draw a conclusion that since the low detect limit of hrICP-MS, a much high quality water is essential if very accurate analysis results were needed.
2. Since the common memory effect phenomenon exists, the flushing step is necessary and important. A much long time and more times of flushing steps is ideal by consideration of the time-efficiency and chemical-consumption.
3. An obvious signal decline was observed for standards, and the reason for this decline is supposed by the pollution of sampler / skimmer cones in the interface part. Because the diameter of the cones were smaller than the normal size, and less sample droplets can pass this cones to enter detecting system, the detected signal is less and the final analysis results are correspondingly less too.
4. Since the low detect limit in our hrICP-MS, a detect contamination in blanks and standards were obtained. These results first proved the high detected performance of hrICP-MS, and secondly indicated the much accurate results need to eliminate all the potential existing factors from exterior part of analysis.

References

- Agatemor, C. and Beauchemin, D., 2011. Matrix effects in inductively coupled plasma mass spectrometry: A review. *Anal Chim Acta*, 706(1): 66-83.
- Ammann, A.A., 2007. Inductively coupled plasma mass spectrometry (ICP MS): a versatile tool. *Journal of Mass Spectrometry*, 42(4): 419-427.
- Cornelis, R., Caruso, J., Crews, H. and Heumann, K., 2003. *Handbook of Elemental Speciation: Techniques and Methodology*. John Wiley & Sons, Ltd.
- ThermoFinnigan, 2008. *Thermo Finnigan ELEMENT 2 User Guide*.
- Vanhaecke, F., Boonen, S., Moens, L. and Dams, R., 1995. Solid Sampling Electrothermal Vaporization Inductively-Coupled Plasma-Mass Spectrometry for the Determination of Arsenic in Standard Reference Materials of Plant-Origin. *J Anal Atom Spectrom*, 10(2): 81-87.



Chapter 5

Desalination of Oil Coproduced Water by Eutectic Freeze Crystallization

Presented at 9th European Congress of Chemical Engineering, 21-24 April 2013, the Hague, the Netherlands.

Xiaoqian Lu, F.Elif Genceli Güner, Essam El-Sayed, Ali Alodwani, Jaap van Spronsen, Geert-Jan Witkamp. Prepared for submission to Desalination.

Abstract

Together with the production of oil an ever increasing amount of saline water is produced. This produced water contains a variety of compounds like inorganic salts, organics, naturally occurring radioactive materials and chemicals used for the production of oil. Development of new and improved technologies to diminish this stream will greatly reduce the environmental burden caused by disposal of this stream. Eutectic freeze crystallization, a new technology currently under development in the laboratory, was tested on produced water from Kuwait. At the eutectic point of $-23\text{ }^{\circ}\text{C}$ ice and $\text{NaCl}\cdot 2\text{H}_2\text{O}$ crystallized simultaneously. The ice product after washing and melting contained about 100 mg/kg sodium chloride and 10 mg/kg of Ca and Mg. Inclusions of mother liquor in the ice crystals were below 0.05 wt%. After filtration and washing of the $\text{NaCl}\cdot 2\text{H}_2\text{O}$ crystals more than 99 % of the impurities were left in the filtrate except for Br. Bromide was partially taken up into the crystal lattice. Inclusions of mother liquor in the $\text{NaCl}\cdot 2\text{H}_2\text{O}$ crystals were below 0.1 wt%. The process was scaled up in a 10 liter scraped wall crystallizer. As an additional purification step the $\text{NaCl}\cdot 2\text{H}_2\text{O}$ crystals were recrystallized into anhydrous NaCl. Next to potable water and highly pure sodium chloride, bromine is possibly an interesting product that can be recovered economically from this quality produced water. Further investigations of the EFC process with respect to relevant process parameters and scaling up are needed in order to determine if EFC is a viable option to recover valuable products from oil co-produced water.

5.1 Introduction

Along with the production of oil saline water is produced. This produced water partly originates from the underground formation and is the largest volume waste stream associated with oil production. For example in 1993 oil companies were producing two barrels of water for each barrel of oil (AlAnezi et al., 2013). The composition and volume of the produced water varies throughout the lifetime of the reservoir but the general trend is that with the ageing of the reservoir the production of water increases substantially with respect to the production of oil. The composition of the produced water varies widely depending upon the origin (**Table 5.1**) (AlAnezi et al., 2013; Himawan et al.).

Table 5.1 Composition of oil field brines from different locations.

| Major ions | Typical oil field brines from North America | Brines from Kuwait oilfields | |
|-----------------|---|------------------------------|--------------|
| | | Rawdatayn | Sabriyah |
| | ppm | | |
| Na | 12000-15000 | 11700-204000 | 9800-275000 |
| Ca | 1000-120000 | 2200-99000 | 2600-78000 |
| Mg | 500-25000 | 1600-29000 | 1400-28000 |
| K | 30-4000 | 1500-17000 | 800-19000 |
| Sr | 5-5000 | 70-500 | 80-640 |
| Ba | 0-1000 | 0-18 | 0-7 |
| Li | 1-50 | 0-5 | 0-7 |
| SO ₄ | - | 330-3000 | 45000-135000 |

Major constituents are inorganic salts. Minor constituents are hydrocarbons (from the oil), sulfides, naturally occurring radioactive materials (NORM) and chemicals used in the oil production process. Disposal of this waste stream is an ongoing concern as environmental regulations become stricter and the stream becomes larger. The best way to dispose the waste stream is largely determined by the composition of the stream and by the location of origin. Disposal methods that are currently being used are reinjection in suitable layers and discharge into pits. Both methods are problematic because of pollution of the environment and because there is a risk of polluting water aquifers used for the production of potable water. In order to diminish these problems another way of looking at produced water is helpful. One way is to look at produced water as a process stream that contains valuable materials that can be recovered. The first one that comes to mind is water. Recovery of water from produced water greatly diminishes the produced water stream. The purified water can be used for consumption and agriculture. Valuable salts can be isolated and sold.

An interesting situation exists in the oil producing countries in the Middle East. In these countries a large part of the water for consumption is prepared from seawater by multistage flash distillation (MSF) and to a lesser extent by reverse osmosis (RO). This leads to the destruction of marine life and pollution of the marine environment with highly saline solutions containing chemicals like anti-

scalants and anti-foaming agents. Instead of using seawater for the production of water, produced water from the oil industries can be used for the production of water. For example in Kuwait oil production in 2011 was about $0.6 \text{ M m}^3/\text{d}$ (AlAnezi et al., 2013). Based upon the ratio above this relates to $1.2 \text{ M m}^3/\text{d}$ produced water. This is almost equal to the $1.4 \text{ M m}^3/\text{d}$ of water produced for consumption by MSF (Darwish and Al-Najem, 2005). The recovery of water from produced water has been investigated using RO (Cakmakci et al., 2008) and electro dialysis (Sirivedhin et al., 2004). These two technologies can only be used for salt concentrations below 5 %. Above 5 % salt concentration water can be recovered by evaporation or by cooling crystallization. When the salt concentration increases above the saturation level evaporative crystallization and eutectic freeze crystallization (EFC) come into view. Evaporative crystallization is a widely applied mature technology. EFC is a technology that is currently being developed in the laboratory. The working of EFC can be explained with the use of the binary phase diagram of sodium chloride and water (Figure 5.1).

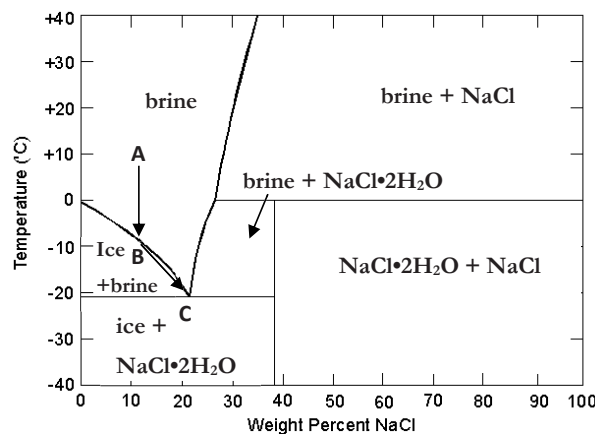


Figure 5.1 NaCl/water binary phase diagram (Ken Muldrew and McGann).

When a solution of sodium chloride in water with a concentration of less than 23 % is cooled down, ice will crystallize when the temperature crosses the phase line in the phase diagram (A→B). The ice that crystallizes is pure and does not contain substantial amounts of sodium chloride. Because the density of the ice is lower than the density of the solution it will start to float. The crystallization of ice will cause an increasing sodium chloride concentration in solution. Upon further cooling more ice will crystallize and the temperature will keep decreasing because the increasing salt concentration causes melting point depression (B→C). Upon reaching -21.3°C the solution is saturated with sodium chloride (23 %) and sodium chloride dihydrate starts to crystallize. The density of the sodium chloride dihydrate crystals is higher than the solution causing the salt crystals to sink to the bottom. Upon further cooling ice and salt crystallize simultaneous and the

temperature in the solution remains constant because the salt concentration in solution remains constant. This point in the phase diagram is called the eutectic point. In a continuous process sodium chloride solution is fed into the crystallizer. In the crystallizer ice and salt are formed at the eutectic temperature. After crystallization, ice and sodium chloride dihydrate slurry are removed from the crystallizer separated and isolated by filtration. The sodium chloride dihydrate can be recrystallized into sodium chloride anhydrate by increasing the temperature above the peritectic point of 0 °C.

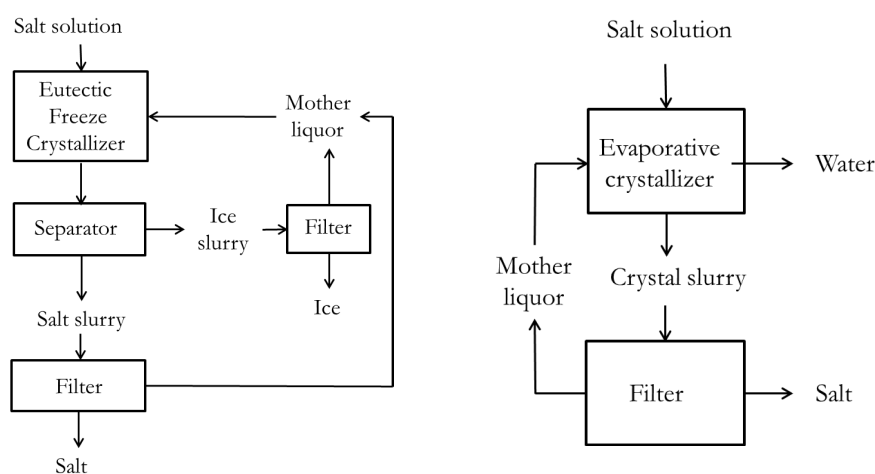


Figure 5.2 Flow sheet EFC (left) and evaporative crystallization (right).

A comparison between EFC and evaporative crystallization is difficult because evaporative crystallization is a mature technology and EFC has been demonstrated in industry. Advantages of EFC over evaporative crystallization are less energy consumption because crystallization of ice consumes less energy than evaporation of water. Corrosion is less because the operating temperature is much lower. The crystallization proceeds much more controlled because local high supersaturation at the evaporation point is avoided. Scaling in the equipment can be less severe or even non-existent. Advantages of evaporative crystallization are an excellent separation between water and concentrate. In order to reach the same water quality in an EFC process thorough washing of the ice is essential or an RO unit can be used for the molten ice. Less unit operations are needed for evaporative crystallization. An EFC process needs a separation step for the ice/salt slurry and an isolation step for the ice (**Figure 5.2**).

EFC can be performed with direct cooling (Barduhn and Manudhane, 1979; Stepakof.Gl et al., 1974) or with indirect cooling. A disadvantage of direct cooling is that refrigerants like cfk's or

hydrocarbons end up in the environment. A solution for this problem is the use of CO₂ as refrigerant (Vaessen et al., 2000). For indirect cooling scraped wall heat exchangers were developed (Pascual et al., 2010). Possible applications that were investigated at the laboratory were the purification of brackish waters (Stepakof.Gl et al., 1974) and the production of various salts like copper sulfate (Pronk, 2006; van der Ham, 1999; van der Ham et al., 2004), magnesium sulfate (Himawan et al., 2006) and sodium carbonate (Van Spronsen et al., 2010).

Aim of this research is to test if EFC can be applied on produced water. A produced water stream from the Kuwait oil industries was obtained and carefully investigated with respect to the presence of useful products. Next, EFC experiments were performed at 1 liter scale and the quality of the products obtained was determined. Finally the process was scaled up to 10 liter in a cooled scraped wall crystallizer operating in batch mode.

5.2 Materials and methods

5.2.1 Materials

Produced water was obtained from KISR. Sodium chloride p.a. was obtained from Sigma Aldrich.

5.2.2 Set up 1 liter batch experiments

The EFC experiments were performed in a 1 liter plastic beaker equipped with an agitator (**Figure 5.3**). The crystallizer was placed inside a jacketed vessel with the jacket connected to a TLC 80/11 cooling machine from Tamson Instruments B.V. with a cooling capacity of 10 kW at 0 °C and an accuracy of 0.5 %. The crystallizer was cooled indirectly with methanol between the wall of the crystallizer and the jacketed vessel. During the experiment the crystallizer was covered with an isolated lid. Temperature was measured with three PT-100 sensors connected to an ASL F250 precision thermometer with an accuracy of ± 0.01 °C. Two temperature sensors were placed in the solution inside the crystallizer, while the third temperature sensor was placed in the methanol between the crystallizer and the jacketed vessel. The temperature data were recorded with a Labview data acquisition system.

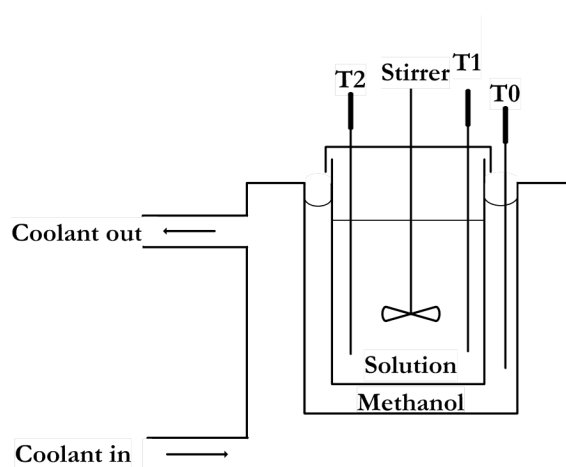


Figure 5.3 Scheme of 1 liter set-up.

5.2.3 Experimental procedure 1 liter batch experiments

1 liter of produced water was added to the crystallizer. The agitator was started at 200 rpm and the temperature measurement and data acquisition system were started. Next the cooling machine was started with a temperature set point of -27°C . After crystallization of ice and salt the stirrer was stopped. The salt was allowed to settle at the bottom and the ice was allowed to float to the surface of the crystallization mixture. The ice crystals were filtered over a glass filter at 0°C and washed repeatedly with pure water of 0°C . The salt crystals were filtered below 0°C to prevent recrystallization of $\text{NaCl}\cdot 2\text{H}_2\text{O}$ into NaCl anhydrate and were washed with saturated sodium chloride solution with a temperature of -6°C . The crystallization process was followed by studying samples from the crystallizer under the microscope. Samples of liquid and solid phases were collected and analyzed by ICP-OES.

5.2.4 Set up 10 liter scraped wall crystallizer

The 10 liter scraped wall crystallizer that was used to perform the EFC experiments is depicted in **Figure 5.4**. The scraped wall crystallizer was connected to a Lauda PUK 90 SW cooling unit with an accuracy of $\pm 0.1^{\circ}\text{C}$. The temperature of the solution inside the crystallizer was measured at the top (1 sensor) and at the bottom (2 sensors) with an ASL F250 precision thermometer equipped with PT-100 temperature sensors with an accuracy of $\pm 0.01^{\circ}\text{C}$. In order to be able to calculate the heat transfer the temperature of the coolant going in and out of the crystallizer and the coolant flow rate was measured. The data were collected by a Labview data acquisition program.

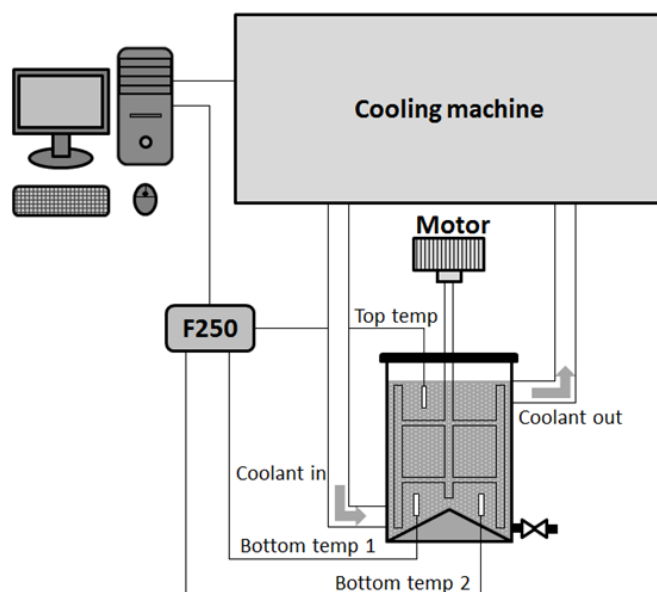


Figure 5.4 Scheme of 10 liter set-up.

5.2.5 Experimental procedure experiments in 10 liter scraped wall crystallizer

10 liter produced water was added to the crystallizer. The scraper, the temperature measurement and data acquisition system were started. Next the cooling machine was started with a temperature set point of -27°C . After crystallization of ice and salt the stirrer was stopped. The salt was allowed to settle at the bottom and the ice was allowed to float to the surface of the crystallization mixture. The ice crystals were filtered over a glass filter at 0°C to prevent melting and washed repeatedly with pure water of 0°C . The salt crystals were filtered over a glass filter below 0°C to prevent recrystallization of $\text{NaCl}\cdot 2\text{H}_2\text{O}$ into NaCl anhydrate and were washed with saturated sodium chloride solution with a temperature of -6°C . Samples of liquid and solid phases were collected and analyzed by ICP-OES.

5.2.6 Recrystallization of $\text{NaCl}\cdot 2\text{H}_2\text{O}$ into NaCl in a 0.6 liter stirred crystallizer

A saturated sodium chloride solution prepared from p.a. sodium chloride and pure water at 25°C was added to a 600 ml stirred crystallizer. The temperature was maintained at 25°C by a hot plate from IKA WERKE. $\text{NaCl}\cdot 2\text{H}_2\text{O}$ crystals from an EFC experiment were added to the sodium chloride solution. After 2 hours of stirring at 25°C the salt crystals were filtered and washed with

saturated sodium chloride solution. Samples of liquid and solid phases were collected and analyzed by ICP-OES.

5.3 Results and discussion

5.3.1 Analysis of produced water, product opportunities

The analysis of the produced water from Kuwait is presented in **Table 5.2**.

Table 5.2 Composition of produced water from Kuwait (mg/kg).

| Element | Na | Cl | Ca | K | Mg | Br | SO ₄ | Sr | B |
|---------|-------|--------|-------|------|------|-----|-----------------|-----|----|
| Content | 46000 | 120000 | 16500 | 3600 | 2400 | 890 | 530 | 430 | 37 |

Table 5.2 shows that the produced water contains about 16 % NaCl and 2.5 % impurities. Ca, K, Mg and Sr are the main cationic impurities, and Br and SO₄ are the main anionic impurities. Other impurities are below the detection limit of the ICP-OES. Based upon this analysis we can see that next to water bromine is an interesting product that can be obtained from this stream. Bromine is mainly used as a fire retardant in plastics and the market for bromine is steadily increasing over the years. A small amount of bromine is produced from sea water. Sea water contains about 60 ppm of bromide which is 15 times less than this particular stream. About 50 % of the world production of bromine is produced in the USA and is recovered from produced water (Arkansas Geological Survey 2012). This produced water contains about 4000 mg/kg bromide. Based upon these figures it can be concluded that concentrating the produced water stream from Kuwait with a factor of four will result in a stream from which bromine can be isolated on a commercial basis. Another valuable compound is potassium but the concentration is too low for commercial recovery. The analytical results in **Table 5.2** show that sodium chloride is the major component and it is expected to crystallize first in an EFC process. The economic value of sodium chloride is largely dependent upon the purity. Low quality sodium chloride is always produced locally because transportation costs are prohibitive. The case may be different if a high quality sodium chloride (impurities below the mg/kg level) suitable for electrolysis can be produced.

5.3.2 Crystallization experiments in the 1 liter crystallizer

The binary phase diagram of sodium chloride/water (**Figure 5.1**) predicts that after cooling the solution to about -17 °C ice crystals will start to crystallize. Furthermore about 30 % of the solution has to be crystallized as ice before the eutectic point is reached and sodium chloride NaCl·2H₂O

will start crystallizing. In order to determine the phase behavior of the produced water, 1 liter of produced water was added to the 1 liter crystallizer. The agitator was started at a speed of 280 rpm and the cooling machine was started with a set point of -27°C . The temperature inside the crystallizer as a function of time is depicted in **Figure 5.5**.

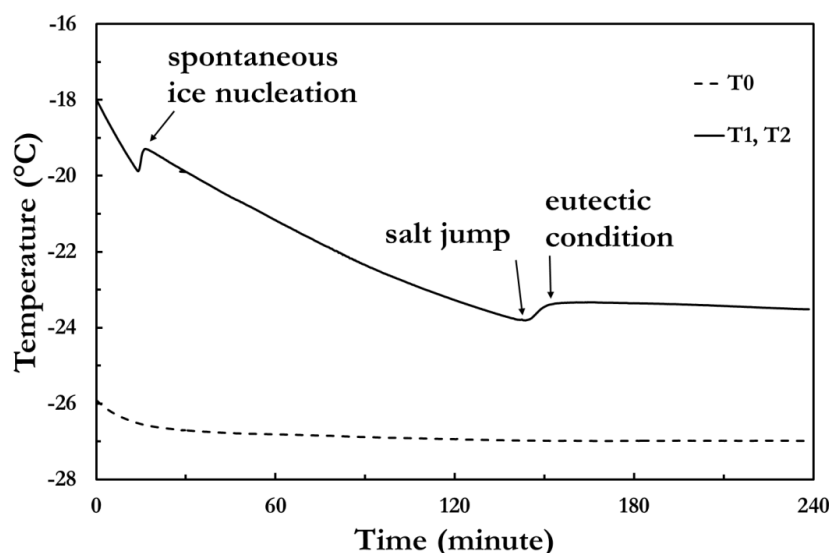


Figure 5.5 Temperature inside the crystallizer as a function of time. T1 and T2 are the temperatures inside the crystallizer, T0 is the temperature of the methanol between the crystallizer and the jacketed vessel.

The figure shows that after 20 minutes cooling there was a temperature jump from -19.88°C to -19.30°C indicating the nucleation and growth of ice crystals. Upon further cooling the temperature inside the crystallizer decreased at a lower rate because part of the heat transfer was used for crystallization of the ice. After 150 minutes of cooling there was a temperature jump from -23.81°C to -23.34°C indicating the nucleation and growth of $\text{NaCl}\cdot 2\text{H}_2\text{O}$ crystals. After nucleation of the salt the eutectic point in the phase diagram was reached. The temperature inside the crystallizer was 2 degrees below the eutectic point of the pure system. The lower eutectic point is explained by melting point depression due to the presence of the impurities in solution. Upon further cooling the temperature inside the crystallizer kept decreasing at a very slow rate because over time the concentration of the impurities in the solution kept increasing. After 240 minutes the experiment had to be stopped because the crystallizer was completely filled up with a thick slurry of ice crystals and a small amount of $\text{NaCl}\cdot 2\text{H}_2\text{O}$ crystals. The thickness of the slurry made separation of ice and $\text{NaCl}\cdot 2\text{H}_2\text{O}$ impossible.

In order to be able to isolate the $\text{NaCl} \cdot 2\text{H}_2\text{O}$ crystals from the produced water, a more concentrated solution was needed. It was decided to use the 10 liter scraped wall crystallizer to pre-concentrate the produced water by freeze crystallization. After crystallization, the ice was removed from the produced water by filtration over a glass filter. The composition of the concentrated solution is presented in **Table 5.3**.

1 liter of concentrated produced water was added to the 1 liter crystallizer. Stirring was started at a speed of 280 rpm and the cooling machine was started with a set point of -27°C . **Figure 5.6** depicts the temperature inside the crystallizer as a function of time.

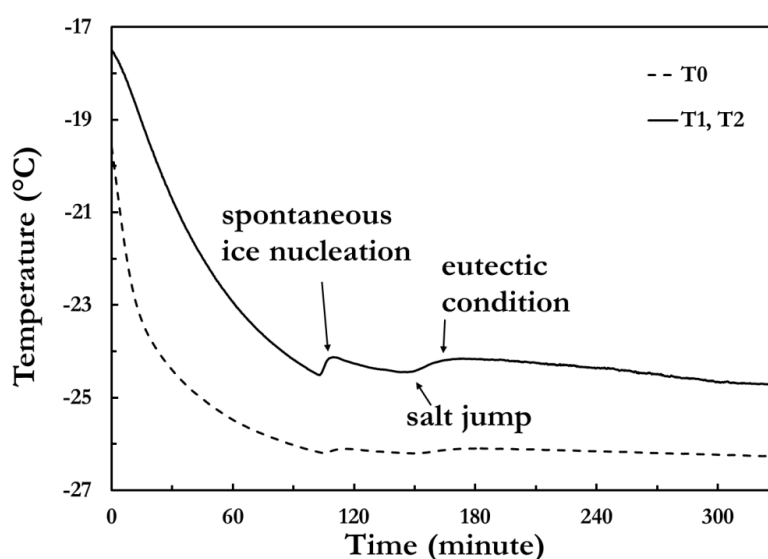


Figure 5.6 Temperature inside the crystallizer as a function of time. T1 and T2 are the temperatures inside the crystallizer; T0 is the temperature of the methanol.

As shown in this figure, nucleation and growth of ice crystals started at -23.60°C . Upon further cooling, $\text{NaCl} \cdot 2\text{H}_2\text{O}$ crystallized at -24.38°C and the temperature increased to -23.58°C . 3 hours after the nucleation of $\text{NaCl} \cdot 2\text{H}_2\text{O}$ the stirrer was stopped. **Figure 5.7a** shows the $\text{NaCl} \cdot 2\text{H}_2\text{O}$ crystals at the bottom of the crystallizer and the ice crystals floating in the top part of the solution. The ice crystals are roughly circular with an average size of about 0.1 mm (**Figure 5.7b**). The salt crystals have hexagonally shape with an average size of 0.15 mm (**Figure 5.7c**).

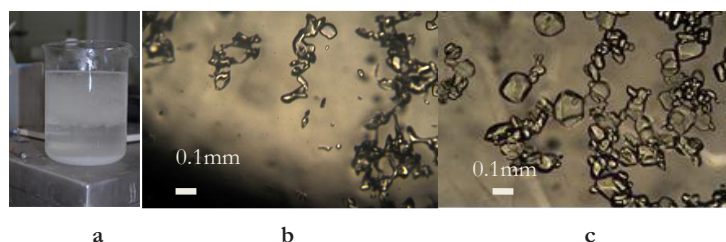


Figure 5.7. a: Ice and salt product slurry, b: Ice crystals, c: salt crystals.

After decanting the ice slurry, the ice crystals were isolated by filtration over a glass filter and washed two times with pure water of 0 °C. The analytical results are presented in **Table 5.3**. These data show that the ice crystals are substantially pure. The ice product after washing and melting contained about 100 mg/kg sodium chloride and 10 mg/kg of Ca and Mg. All other impurities were below the detection limit (<1 mg/kg). The calcium concentration in washed ice product was 2000 times lower than in solution. This meant that inclusions of mother liquor in the ice crystals were below 0.05 wt%. Also literature indicates that ice crystallization is extremely selective with respect to impurity uptake. Most of impurities present in the molten ice were expected to be residual mother liquor.

Table 5.3. Effect of washing upon the quality of the ice crystals.

| | Na | Cl | Ca | K | Mg | Br | SO ₄ | Sr | B |
|----------------------|-------|--------|-------|------|------|------|-----------------|-----|----|
| Ice crystals | mg/kg | | | | | | | | |
| unwashed | 39000 | 76000 | 10800 | 2270 | 1770 | 550 | 214 | 250 | 19 |
| 1 st wash | 105 | <50 | 29 | <1 | 4 | <1 | <1 | <1 | <1 |
| 2 nd wash | 117 | <50 | 11 | <1 | 9 | <1 | <1 | <1 | <1 |
| Mother liquor | 48000 | 160000 | 23000 | 4690 | 3950 | 1120 | 460 | 550 | 41 |

The NaCl·2H₂O crystal slurry was filtered over a glass filter and the crystals were washed with saturated NaCl solution at -6 °C. The ICP-OES results are presented in **Tables 5.4** and **5.5**. From these data it was concluded that more than 99% of the impurities remain in the filtrate and do not significantly build up into the NaCl·2H₂O product except for Br and K. Bromine partially builds into the crystal lattice of the NaCl·2H₂O crystals, for potassium this was less clear since the washing liquid contained also a significant amount of K. For K we concluded that most of it remained in the filtrate. The calcium concentration in washed NaCl·2H₂O was 1000 times lower than in solution. This meant that inclusions of mother liquor in the NaCl·2H₂O crystals were below 0.1 wt%. Mg, SO₄, Sr and B impurities inside the crystal were on a low level below the detection limit.

Table 5.4 Composition of the start solution, mother liquor (ML) and washing liquid (WL).

| | Na | Cl | Ca | K | Mg | Br | SO ₄ | Sr | B |
|----------|-----|----|-------|------|------|------|-----------------|-----|----|
| | % | | mg/kg | | | | | | |
| Solution | 4.8 | 17 | 21000 | 4330 | 3580 | 1040 | 419 | 500 | 38 |
| ML | 4.8 | 16 | 23000 | 4690 | 3950 | 1120 | 461 | 550 | 41 |
| WL | 7 | 20 | 4 | 74 | <1 | 21 | 7 | <1 | <1 |

Table 5.5 Effect of washing on the impurity content of the NaCl·2H₂O crystals (mg/kg).

| salt | Na | Cl | Ca | K | Mg | Br | SO ₄ | Sr | B |
|----------------------|----|----|-------|-----|-----|-----|-----------------|----|----|
| | % | | mg/kg | | | | | | |
| Unwashed | 18 | 29 | 752 | 481 | 136 | 493 | 80 | 19 | <1 |
| 1 st Wash | 16 | 29 | 222 | 236 | 40 | 406 | 204 | 5 | <1 |
| 2 nd Wash | 17 | 24 | 36 | 127 | <1 | 440 | <1 | <1 | <1 |
| 3 rd Wash | 17 | 25 | 30 | 126 | <1 | 457 | <1 | <1 | <1 |

5.3.3 Crystallization experiments in the 10 liter scraped wall crystallizer

In order to test the effect of scaling up upon the product quality and to test if scale formation on the heat exchanging surface could be controlled and removed by scraping, EFC of the saline water was tested in a 10 liter scraped wall crystallizer. After addition of 10 liter of concentrated produced water to the crystallizer the scraper was started at 10 rpm and the cooling machine was started with a temperature set point of the coolant of -27 °C. **Figure 5.8** depicts the temperature inside the crystallizer as a function of time. The figure is the same as for the 1 liter experiment (**Figure 5.6**). Ice crystallized at -23.00 °C and salt crystallized at -24.08 °C. Scraping of the wall of the crystallizer with a ΔT of 3 °C over the heat exchanger was possible. After 3 hours of NaCl·2H₂O crystallization the scraper was stopped. 1 liter of NaCl·2H₂O slurry was collected from the bottom of the crystallizer. The NaCl·2H₂O crystals were isolated by filtration and washed with saturated sodium chloride solution. The results of the ICP-OES analysis are presented in **Tables 5.6** and **5.7**. The quality of the NaCl·2H₂O crystals was comparable to the crystals obtained from the 1 liter experiments.

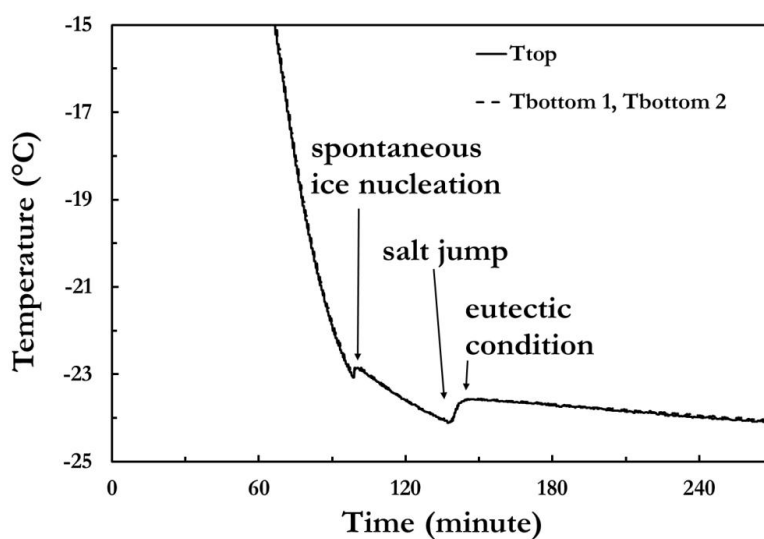


Figure 5.8 Temperature profile for eutectic freeze crystallization in 10 liter setup.

Table 5.6 Composition of the starting solution, mother liquor (ML) and washing liquid

| | Na | Cl | Ca | K | Mg | Br | SO ₄ | Sr | B |
|----------|-----|----|-------|------|------|------|-----------------|-----|----|
| | % | | mg/kg | | | | | | |
| Solution | 4.3 | 15 | 19900 | 2500 | 3300 | 930 | 380 | 490 | 35 |
| ML | 4.1 | 16 | 24600 | 2800 | 4100 | 1200 | 480 | 640 | 46 |
| wash | 7.2 | 17 | 11 | 72 | 2 | 16 | <1 | <1 | 2 |

Table 5.7 Effect of washing on the impurity content of the NaCl·2H₂O crystals.

| salt crystals | Na | Cl | Ca | K | Mg | Br | SO ₄ | Sr | B |
|----------------------|----|----|-------|------|-----|-----|-----------------|-----|----|
| | % | | mg/kg | | | | | | |
| unwashed | 11 | 26 | 3300 | 1440 | 630 | 455 | 83 | 102 | 11 |
| 1 st wash | 16 | 38 | 151 | 155 | 28 | 338 | 1 | 5 | 4 |
| 2 nd wash | 16 | 38 | 21 | 100 | 3 | 294 | <1 | <1 | 4 |
| 3 rd wash | 16 | 39 | 21 | 103 | 3 | 259 | <1 | <1 | 4 |

5.3.4 Recrystallization experiments in a 0.6 liter recrystallizer

Above the peritectic point of 0 °C NaCl·2H₂O will recrystallize into NaCl. This recrystallization is necessary to transform the NaCl·2H₂O obtained from the EFC process into a salt that can be stored and transported at room temperature. The recrystallization is also an opportunity for an extra purification of the salt. In order to get an impression of the effect of the recrystallization on the purity of the product, experiments were carried out in a 600 milliliter crystallizer at 25 °C. Washed NaCl·2H₂O crystals from an EFC experiment were added to saturated sodium chloride

(p.a.) solution at 25 °C. After stirring the crystal slurry at 175 rpm for 2 hours the NaCl crystals were filtered, washed with saturated NaCl solution and dried. The results of the ICP analysis are presented in **Tables 5.8** and **5.9**. Bromine partitioned between the solution and the NaCl crystals in a 1:2 ratio. The behavior of the other ions was difficult to determine because the purity of the NaCl·2H₂O crystals approached that of the NaCl (p.a. quality) used for the preparation of the recrystallization solution and the washing liquid. **Figure 5.9** shows that the NaCl crystals have a cubic shape with an average size of about 40 μm .

Table 5.8 Composition of the start solution, mother liquor (ML) and washing liquid (WL).

| | Na | Cl | Ca | K | Mg | Br | SO ₄ | Sr | B |
|----------|----|----|-------|----|-----|----|-----------------|----|---|
| | % | | mg/kg | | | | | | |
| solution | 7 | 17 | 6 | 66 | 1 | 13 | <1 | <1 | 2 |
| ML | 7 | 17 | 6 | 61 | 1 | 27 | <1 | <1 | 2 |
| WL | 7 | 17 | 2 | 54 | 0.3 | 8 | <1 | <1 | 2 |

Table 5.9 Effect on the product quality of recrystallization of NaCl·2H₂O into NaCl and washing of the final product.

| NaCl | Na | Cl | Ca | K | Mg | Br | SO ₄ | Sr | B |
|------------------------|----|----|-------|-----|-----|-----|-----------------|-----|---|
| | % | | mg/kg | | | | | | |
| NaCl·2H ₂ O | 16 | 39 | 20 | 103 | 3 | 259 | <1 | 0.6 | 4 |
| unwashed | 22 | 50 | 9 | 111 | 1 | 21 | <1 | 0.2 | 5 |
| 1 wash | 20 | 48 | 5 | 93 | 1 | 14 | <1 | 0.1 | 5 |
| 2 wash | 22 | 51 | 3 | 81 | 0.4 | 12 | <1 | 0.1 | 5 |
| 3 wash | 20 | 47 | 11 | 72 | 2 | 13 | <1 | 0.2 | 5 |
| Dry salt | 28 | 64 | 16 | 79 | 3 | 15 | <1 | 0.5 | 5 |

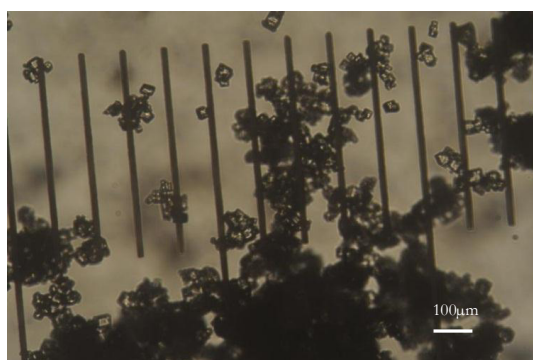


Figure 5.9 NaCl crystals after recrystallization.

5.4 Conclusions

A representative sample of produced water from Kuwait oil production was analyzed by ICP-OES and shown to consist of about 16 % NaCl and 2.5 % of other impurities, of which Ca (1.6 %), K (3600 mg/kg), Mg (2400 mg/kg), Br (900 mg/kg), SO₄ (500 mg/kg), Sr (400 mg/kg) and B (40 mg/kg) were the main ones. Other impurities were below the detection limit. Investigations into the economic value of this stream show that pure water is an interesting product because potable water is scarce in the Middle East and is currently being produced by MSF and RO. Also the bromide content is possibly high enough for economic recovery. In the USA bromine is recovered from produced water containing 4000 mg/kg bromide. The economic value of sodium chloride depends upon the quality. Low quality sodium chloride is mainly produced locally because transportation costs are prohibitive. The case may be different if a high quality sodium chloride (impurities below the mg/kg level) suitable for electrolysis can be produced.

Recovery of valuable products from this stream by EFC was tested. First the produced water was pre-concentrated (about 25 %) by freeze concentration in order to be able to isolate salt in the batch experiments (in a continuous EFC process, freeze concentration is not necessary). Next, batch EFC of the pre-concentrated solution was performed at 1 liter scale. The ice crystals were isolated by filtration and washed with pure water. The ice crystals after washing and melting contain about 100 ppm sodium chloride and 10 ppm of Ca and Mg. Inclusions of mother liquor in the ice crystals are below 0.05 wt%. The NaCl·2H₂O crystals were filtered and washed with saturated sodium chloride solution. More than 99 % of the impurities were left in the filtrate except for Br and K. Bromine partially built up into the crystal lattice, for potassium this was less clear since the washing liquid contained also a significant amount of K. Most of the K however remained in solution. Inclusion of mother liquor in the NaCl·2H₂O crystals is below 0.1 wt%. Mg, SO₄, Sr and B impurities inside the crystal are on a low level below the detection limit. With the exception of the high bromide content the quality of the NaCl·2H₂O is comparable to that of p.a. NaCl. The NaCl·2H₂O salt crystals have hexagonal shape with an average size of 0.15 mm. The EFC process was scaled up to a batch 10 liter scraped wall crystallizer. A maximum delta T of 3.5 °C between the cooling liquid and the NaCl·2H₂O/ice slurry could be maintained. The quality of the NaCl·2H₂O was comparable to the NaCl·2H₂O from the 1 liter experiments.

Recrystallization of the NaCl·2H₂O crystals into NaCl anhydrate was performed. The NaCl crystals had a cubic shape with an average size of 40 µm. The purification process was difficult to assess because the purity of the NaCl·2H₂O crystals was comparable to the p.a. quality used for the preparation of the recrystallization solution and the washing liquid.

Desalination of Oil Coproduced Water by Eutectic Freeze Crystallization

The batch EFC experiments show that from produced water valuable products can be obtained like pure water and pure NaCl. The local situation will determine if a commercial process is feasible. In order to be able to make better cost calculations and compare them with evaporative crystallization a more thorough study of all parameters involved in the EFC and recrystallization process is necessary. Some examples of important aspects to investigate are continuous operation (a commercial process will be continuous) and scaling up to larger scale. Also EFC of produced waters from different origin and composition have to be studied.

References

- Arkansas Geological Survey 2012. http://www.geology.ar.gov/energy/brine_resources.htm
- AlAnezi, K., Belkharchouche, M., Alali, S. and Abuhaimed, W., 2013. Produced water characterization in Kuwait and its impact on environment. *Desalin Water Treat*, 51(1-3): 302-306.
- Barduhn, A.J. and Manudhane, A., 1979. Temperatures required for eutectic freezing of natural-waters. *Desalination*, 28(3): 233-241.
- Cakmakci, M., Kayaalp, N. and Koyuncu, I., 2008. Desalination of produced water from oil production fields by membrane processes. *Desalination*, 222(1-3): 176-186.
- Darwish, M.A. and Al-Najem, N., 2005. The water problem in Kuwait. *Desalination*, 177(1-3): 167-177.
- Himawan, C., Kramer, H.J.M. and Witkamp, G.J., 2006. Study on the recovery of purified $\text{MgSO}_4 \cdot 7\text{H}_2\text{O}$ crystals from industrial solution by eutectic freezing. *Separation and Purification Technology*, 50(2): 240-248.
- Ken Muldrew and McGann, L.E., *Cryobiology*
- Pascual, M.R. et al., 2010. A novel scraped cooled wall crystallizer: Recovery of sodium carbonate and ice from an industrial aqueous solution by eutectic freeze crystallization. *Chem Eng Res Des*, 88(9A): 1252-1258.
- Pronk, P., 2006. Fluidized Bed Heat Exchangers to Prevent Fouling in Ice Slurry Systems and Industrial Crystallizers, PhD Thesis, Delft University of Technology.
- Sirivedhin, T., McCue, J. and Dallbauman, L., 2004. Reclaiming produced water for beneficial use: Salt removal by electrodialysis. *J Membrane Sci*, 243(1-2): 335-343.
- Stepakof, G.I., Siegelma, D., Johnson, R. and Gibson, W., 1974. Development of a eutectic freezing process for brine disposal. *Desalination*, 15(1): 25-38.
- Vaessen, R.J.C., van der Ham, F. and Witkamp, G.J., 2000. Eutectic freeze crystallization using CO_2 clathrates. *Ann Ny Acad Sci*, 912: 483-495.
- van der Ham, F., 1999. Eutectic Freeze Crystallization, PhD Thesis, Delft University of Technology.
- van der Ham, F., Seckler, M.M. and Witkamp, G.J., 2004. Eutectic freeze crystallization in a new apparatus: the cooled disk column crystallizer. *Chem Eng Process*, 43(2): 161-167.
- Van Spronsen, J. et al., 2010. Eutectic freeze crystallization from the ternary $\text{Na}_2\text{CO}_3\text{-NaHCO}_3\text{-H}_2\text{O}$ system: A novel scraped wall crystallizer for the recovery of soda from an industrial aqueous stream. *Chem Eng Res Des*, 88(9A): 1259-1263.

Chapter 6

Eutectic Freeze Crystallization as a Tool for Separation of Shale Gas Produced Water into Pure Ice and Salt

Abstract

The development of new and better treatment technologies for flow back water and produced water from shale gas production is essential for the societal acceptance of shale gas exploitation. Eutectic freeze crystallization (EFC) as a new separation technology was tested at 10 liter scale on a synthetic solution mimicking flow back water from the Marcellus shale. Batch EFC of this solution resulted in a slurry of ice and a mixture of salts. The ice and salts were separated by gravitation. The ice crystals were filtered and washed repeatedly with water and were deemed sufficiently pure for recycling in the shale gas process. The eutectic points of BaCl_2 (-20.6 °C), NaCl (-24.3 °C) and SrCl_2 (-33 °C) were determined for this specific composition. The phase information can be used to design the optimum EFC process. For example a continuous single stage EFC process is possible that operates at the lowest eutectic point (calcium chloride; -55 °C) and transforms the solution completely in pure ice and a mixture of salts reflecting the starting composition. The batch experiment was scaled up to a 200 scraped wall crystallizer. A heat transfer of 4 kW/m² over the heat exchanger could be maintained and no excessive scaling was observed.

6.1 Introduction

In the last ten years the development of technology for the economic recovery of shale gas from tight shale in the USA has led to a large increase in estimated global gas reserves of about 40 % (Rahm and Riha, 2012). These tight shales are not only found in the USA but are widespread throughout the world. Because gas is considered to be less polluting than oil and coal, the recovery of shale gas is a rapidly growing industry. The technological development that made this possible was a combination of horizontal drilling and hydraulic fracturing (fracking). Tight shale, in opposite to for instance sandstone, does not release gas readily. Fracking the shale rock with fracking fluid at high pressure opens up existing cracks and creates new cracks. The fracking fluid contains proppants like sand that fills up the cracks and keeps them open after fracking. The horizontal drilling and fracking combined creates a much larger surface area than only vertical drilling and fracking. Through this larger surface area enough gas is released from the shale for commercial exploitation. Because the shale needs to be fracked a much higher number of wells is needed compared to conventional gas production. For each well about 15000 m³ of water is used to prepare the fracking fluid. The fracking fluid contains mainly proppant (sand) and in lower concentrations gelling agents and other chemicals related to the composition of the shale and to protect the equipment. After fracking, water flows back from the well. The first 14 days after fracking this water is named flow back water, after 14 days it is named produced water. For the Marcellus shale the amount of flow back water is about 25 % of the water used for fracking; for other shales it can be up to 70 % (Haluszczak et al., 2013; Hayes, 2009). **Figure 6.1** shows that initially the amount of flow back water is high and that it gradually drops over time. The total amount of dissolved solids (TDS) in the flow back water increases over time (**Figure 6.2**).

Table 6.1 Average concentration of the major constituents in the influent and flow back water from 5 wells (d,e,f,g,g) from the Marcellus shale (Hayes, 2009).

| | influent | day 1 | day 5 mg/L | day 14 | Day 90 |
|-----|----------|-------|---------------|--------|--------|
| TDS | 1920 | 36000 | 75000 | 136000 | 210000 |
| Cl | 800 | 21000 | 52000 | 88000 | 127000 |
| Na | 450 | 10900 | 23300 | 35100 | 44800 |
| Ca | 90 | 2100 | 6500 | 12000 | 18000 |
| Sr | 6* | 380 | 1180 | 2200 | 3400 |
| Ba | 0.4* | 290 | 875 | 1970 | 2800 |
| Mg | 20 | 190 | 600 | 1100 | 1600 |
| Br | 65* | 186 | 493 | 834 | 1011 |
| K | 25 | 95 | 215 | 300 | 500 |
| TOC | 320 | 150 | 76 | 30 | 150 |

* The presence of these traces is probably caused by recycling produced water in the influent.
TOC: Total Organic Carbon

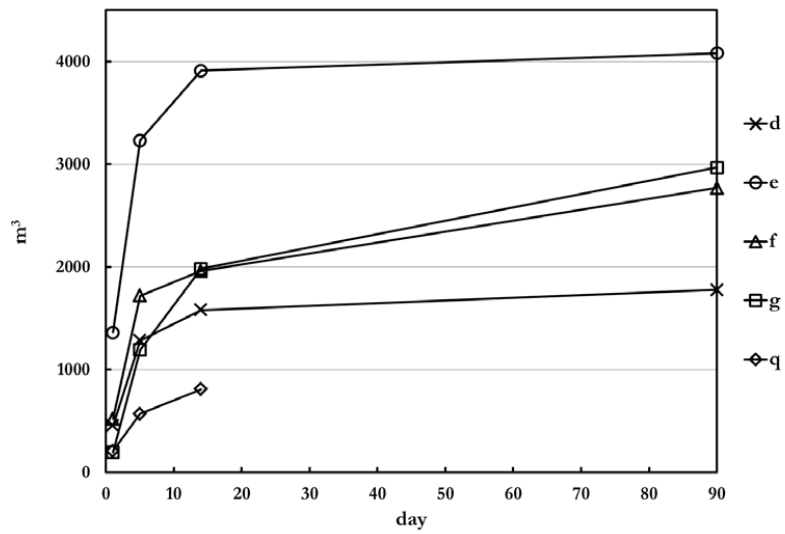


Figure 6.1 Cumulative amount of produced water as a function of time for five wells (d,e,f,g,q) from the Marcellus shale (Hayes, 2009).

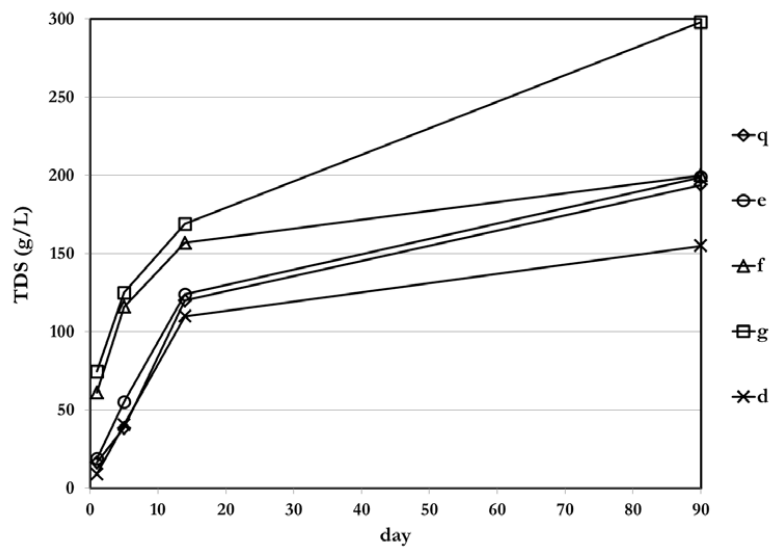


Figure 6.2 TDS (Total Dissolved Solids) of produced water as a function of time for five wells from the Marcellus shale (Hayes, 2009).

Table 6.1 shows the composition of influent and flow back waters from the Marcellus shale. Typical elements present in the solution at high concentrations are Cl, Ba, Sr, Mg, Br, Ca and Na. Furthermore the flow back water contains naturally occurring radioactive materials (NORM, ^{226}Ra and ^{228}Ra) in the order of 200 to 600 Bq/L (Warner et al., 2013). Environmental friendly disposal

or treatment of this stream is essential for the success of shale gas development. It is clear that the stream as such cannot be discharged to the surface water. Injection into underground layers is practiced but is only possible if suitable layers are present which is often not the case. Reuse for the next fracking job is an attractive option but the fracking fluid should be low in salinity for optimal performance. Also mixing of sulfate containing influent water with flow back water containing barium, strontium or calcium may lead to excessive scaling. Part of the flow back water, after proper dilution, can probably be reused in this way. Chemical treatment is also practiced. Ba, Sr, Ca and NORM are precipitated as their sulfates by the addition of sodium sulfate. After filtration the resulting brine, consisting mainly of sodium chloride, is discharged into the environment. The filter cake goes to a regulated landfill. At some locations the flow back water is concentrated by evaporation. The distilled water is reused in the preparation of fracking fluid and the concentrated brine is chemically treated (Veil, 2010).

Because all of the technologies mentioned above have drawbacks and the scale of the shale gas exploration is increasing rapidly there is further need for economically sound and environmentally safe treatment processes for produced water. Reverse osmosis (Mondal et al., 2008), forward osmosis (FO) (Hickenbottom et al., 2013) and electro dialysis (Sirivedhin et al., 2004) are being investigated as suitable technologies but suffer from severe drawbacks like fouling of membranes and a small window of operation. RO works only for diluted solutions and FO has a saline solution as an end product that has to be evaporated.

One of the options that looks promising and is currently being developed is eutectic freeze crystallization (EFC). EFC works as follows. A diluted salt solution is cooled down. According to the phase diagram (**Figure 6.3**) pure ice will start crystallizing after the temperature crosses the phase line (ice line, A->B). The salt concentration will start to increase because water is transformed into ice. Ice will keep crystallizing and the temperature will keep decreasing until the solution is saturated with salt (B->C). At this temperature pure salt will start crystallizing together with the ice and the temperature will remain constant because the concentration in solution remains constant. This point is named the eutectic point. In particular for this shale gas produced water due to the presence of other salts that accumulate in the left solution, the temperature gradually decreases with time until the eutectic condition of the accumulated other salt is reached.

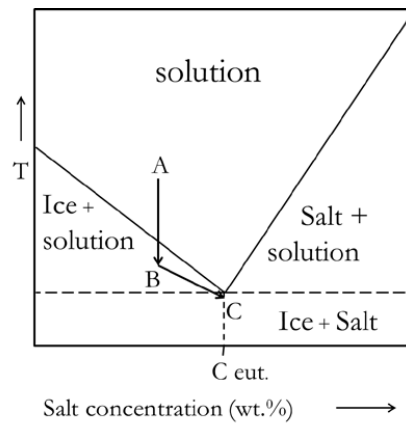


Figure 6.3 EFC in a general binary phase diagram for water and salt.

A continuous process operates at the eutectic point at constant temperature. The ice and salt can be easily isolated separately because ice has a lower density and the salt has a higher density than the solution. The concentration of impurities in the solution that are not taken up in the crystal lattice will increase and cause a lowering of the eutectic temperature due to freeze point depression.

The performance of EFC can be compared to evaporative concentration/crystallization that is already being used for the treatment of flow back water. Advantages of EFC as compared to evaporative crystallization are that the production of ice consumes less energy than the evaporation of water (Van der Ham, 1999). Corrosion is much less because EFC operates at a much lower temperature. There is possibly less scaling because EFC operates at a different part in the phase diagram.

EFC crystallizers with scraped heat exchangers aimed at high heat transfer rates have been developed (Pascual et al., 2010). EFC with direct cooling in the crystallizer was also investigated (Stepakof.Gl et al., 1974). The use of a hydrocarbon like propane as coolant for this application is a good option. EFC was already investigated on laboratory scale for the isolation of sodium chloride from diluted brines (Swenne and Thoenes, 1985) and for the isolation of copper sulfate (van der Ham et al., 1999). On pilot plant scale EFC was tested for the recovery of magnesium sulfate (Himawan et al., 2006) and for the recovery of soda from an industrial stream (Van Spronsen et al., 2010).

Aim of this investigation was to test if EFC is a viable option for the treatment of flow back water/produced water. Because flow back water largely varies with respect to composition, a synthetic solution was prepared containing the elements that are generally found in the highest concentration

in most of the flow back water (Table 6.2). With this solution EFC experiments were performed at 10 liter scale and 200 liter scale.

6.2 Materials and Methods

6.2.1 Materials

$\text{CaCl}_2 \cdot 2\text{H}_2\text{O}$, $\text{MgCl}_2 \cdot 6\text{H}_2\text{O}$, $\text{SrCl}_2 \cdot 6\text{H}_2\text{O}$, $\text{BaCl}_2 \cdot 2\text{H}_2\text{O}$, KCl and NaCl of p.a. quality were obtained from Sigma Aldrich. Appropriate amounts of salts were dissolved in water to reach the concentrations mentioned in Table 6.2. Trace elements mentioned in Table 6.4 were obtained from Sigma Aldrich.

Table 6.2 composition of the solution used for EFC

| Element | Na | Ca | Ba | Sr | Mg | K |
|---------------------|----|-----|-----|-----|------|------|
| Concentration (wt%) | 5 | 2.3 | 1.5 | 0.7 | 0.18 | 0.03 |

6.2.2 10 liter scraped wall crystallizer set up

The 10 liter scraped wall crystallizer that was used for the experiments is presented in Figure 6.4. The scraped wall crystallizer was cooled with a Lauda PUK 90 SW cooling unit with an accuracy of ± 0.1 °C. Data were collected by a Labview data acquisition program. The temperature of the solution inside the crystallizer was measured with PT-100 temperature sensors with an accuracy of ± 0.01 °C connected to an ASL F250 precision thermometer.

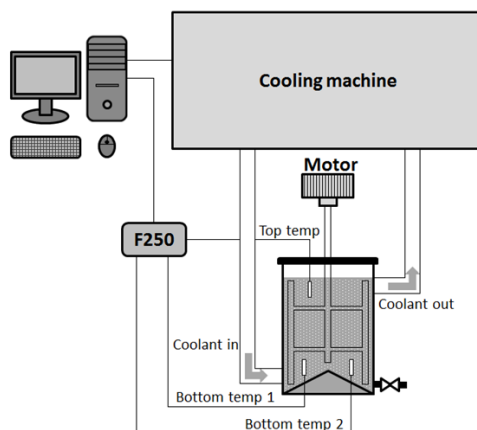


Figure 6.4 Scheme of 10 liter set-up.

6.2.3 200 liter scraped wall crystallizer set up

A drawing of the 200 litre scraped cooled wall crystallizer is presented in **Figure 6.5a**. The crystallizer contains two heat exchanger modules stacked on top of each other. One module (**Figure 6.5b**) consists of two vertical concentric cylinders that are scraped on both sides. The heat exchangers have a total surface area of 0.76 m². The heat exchangers are connected to a cooling machine with a 10 kW cooling capacity at 0 °C which uses freezium™ (43 % potassium formate in water) as a coolant and was supplied by Tamson Instruments B.V. The temperature of the cooling liquid is controlled with an accuracy of 0.1 °C. The temperature of the cooling liquid and the temperature within the crystallizer are measured with an accuracy of ± 0.01 °C by PT-100 sensors connected to an ASL F250 precision thermometer with a resolution of ± 0.001 °C. All equipment was well isolated. For automatic data acquisition a Labview system was used.

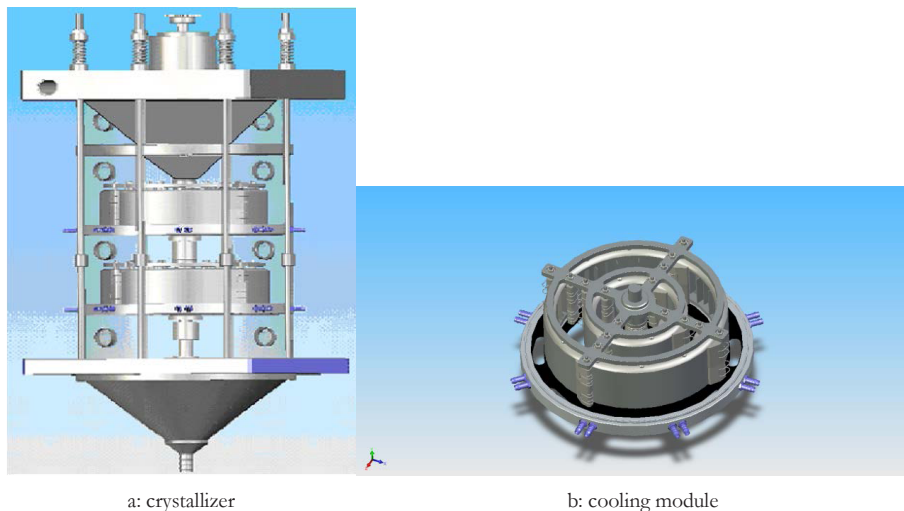


Figure 6.5 200 liter crystallizer.

6.2.4 Experimental procedure EFC experiment with isolation of salt and ice

The 10 liter crystallizer was filled up with 10 liter salt solution (composition according to **Table 6.2**). First, the scraper and the Labview data acquisition system were started. Second, the cooling machine was started. The temperature of the cooling liquid was set at -28 °C, 7 degrees below the eutectic point of pure sodium chloride solution (-21.3 °C). After cooling down and crystallization of a fair amount of ice and salt crystals the scraper was stopped. Because the agitation was stopped ice crystals floated to the top and salt crystals sank to the bottom of the crystallizer. Salt slurry was taken from the bottom of the crystallizer and filtered over a glass filter at -6 °C. The salt crystals

were washed repeatedly with a saturated sodium chloride solution of -6°C . Ice slurry was taken from the top of the crystallizer and filtered over a glass filter at -6°C . The ice crystals were washed repeatedly with water of 0°C . In order to follow the crystallization process samples were taken and studied under the microscope in the cold room at -6°C . Samples of ice, salt and liquids were taken and the composition was determined with ICP-OES.

6.2.5 Experimental procedure EFC experiment with sampling of the liquid phase

The 10 liter crystallizer was filled up with 10 liter salt solution (composition as presented in **Table 6.2**). First, the scraper and the Labview data acquisition system were started. Second, the cooling machine was started. The temperature set point of the cooling liquid was lowered stepwise. As the temperature inside the crystallizer reached -8°C the scraper was stopped and a gas inlet tube closed off with a glass filter was lowered into the solution. The open end of the gas inlet tube was connected to a sampling system and a vacuum pump. A sample of solution was taken from the crystallizer by applying vacuum on the sampling system. The glass filter was necessary to keep crystals inside the crystallizer and to sample only solution. After sampling the gas inlet tube was taken from the crystallizer. The scraper and the cooling was started. After reaching -18°C another sample was taken according to the procedure above. From this temperature on small steps of around 0.5°C were taken in between sampling. In order to prevent freezing of the scraper to the wall the temperature of the cooling liquid was increased just before sampling and lowered again after sampling. As the crystallizer slowly filled up with crystals the crystal slurry became too thick to stir. At this moment a last sample was taken and the experiment was stopped and all equipment was emptied and cleaned. The samples were analyzed with IC.

A new solution of 10 liter was made with the same composition as the last sample. The new solution was added to the 10 liter crystallizer and the experiment was continued according to the procedure above.

6.2.6 Experimental procedure 200 liter scraped wall crystallizer

The 200 liter crystallizer was filled up with 200 liter salt solution (composition as presented in **Table 6.2**). The scrapers and the Labview data acquisition system were started. Next the cooling machine was started. The temperature set point of the cooling machine was lowered stepwise keeping the temperature difference between the solution and the set point 7°C .

6.3 Results and discussion

In order to study the feasibility of EFC for the complete recovery of salts and pure water from produced water, EFC experiments were performed with a synthetic solution.

In the first experiment the synthetic solution was cooled down in the 10 liter scraped wall crystallizer with a temperature set point of the cooling liquid of $-28\text{ }^{\circ}\text{C}$. The temperature profile of a typical experiment is depicted in **Figure 6.6**.

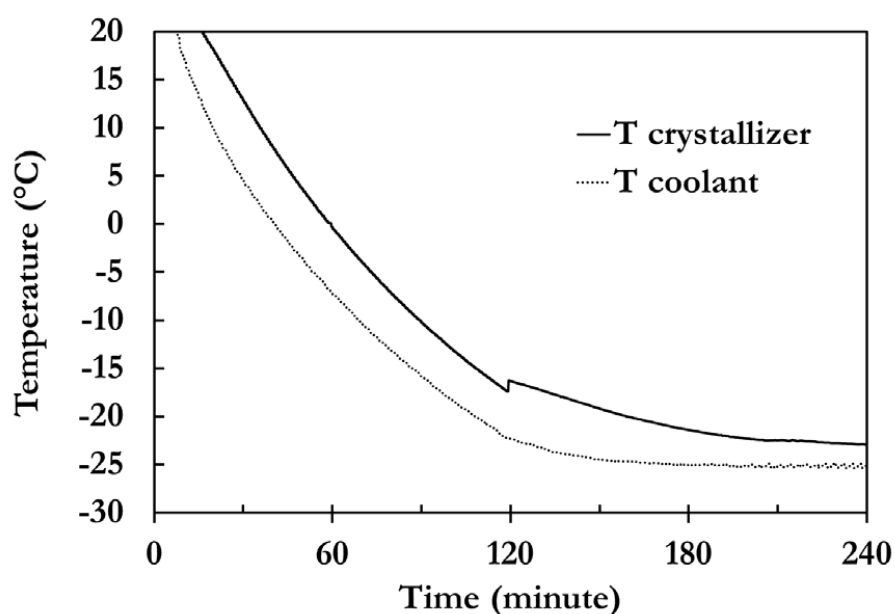


Figure 6.6 Cooling profile and temperature inside the crystallizer as a function of time.

Ice nucleation for this experiment was observed to happen around $-17\text{ }^{\circ}\text{C}$. The temperature jump at this point was caused by the released heat of crystallization of a significant amount of ice due to high supersaturation. The size of the jump is dependent upon the supersaturation at the start of nucleation. For some experiments no significant temperature jump was detected because nucleation started already at low supersaturation. Salt crystallization occurred at $-23.4\text{ }^{\circ}\text{C}$ without a perceptible temperature jump, indicating that a eutectic point was reached. Because the salt sample contained both sodium chloride and barium chloride it was not yet clear if the eutectic point was the sodium chloride point, the barium chloride point or that both points coincided for this solution. Upon further cooling ice and salt crystallized simultaneously. Because sodium chloride, barium chloride and ice crystallized from solution the concentration of the other salts in solution increased

slowly. This increase in salt concentration led to a gradual decrease of the temperature due to freeze point depression. At -23.4 °C salt slurry was taken from the bottom of the crystallizer, filtered and washed three times with saturated sodium chloride solution. The salt samples were analyzed with ICP-OES (**Table 6.3**).

Table 6.3 Effect of washing of the salt and ice crystals.

| | Ba | Na | Ca | Sr | K | Mg | Cl |
|---------------------------------|--------|-------|-------|------|-----|------|--------|
| | mg/kg | | | | | | |
| Start solution | 15000 | 57000 | 25000 | 8300 | 675 | 2100 | 150000 |
| Mother liquor | 5870 | 47700 | 27500 | 9010 | 720 | 990 | 149000 |
| Salt | | | | | | | |
| Salt before wash | 156000 | 77000 | 7800 | 2880 | 390 | 710 | 215000 |
| Salt after 1 st wash | 151000 | 91000 | 1950 | 860 | 150 | 180 | 231000 |
| Salt after 2 nd wash | 159000 | 97000 | 1030 | 570 | 100 | 100 | 256000 |
| Salt after 3 rd wash | 150000 | 94000 | 410 | 310 | 60 | 40 | 237000 |
| Ice | | | | | | | |
| Ice before wash | 8220 | 21580 | 11390 | 3740 | 0 | 990 | 88000 |
| Ice after 1 st wash | 1120 | 2560 | 460 | 160 | 20 | 40 | 7800 |
| Ice after 2 nd wash | 240 | 560 | 110 | 50 | 10 | 10 | 1700 |

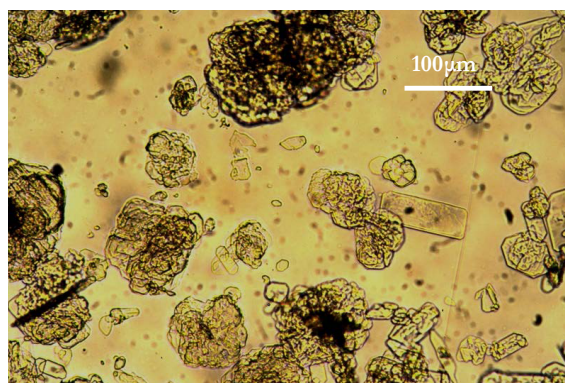


Figure 6.7 Salt crystals at -23.4 °C.

From **Table 6.3** it follows that the salt isolated mainly consisted of sodium chloride with some barium chloride. Because the washing liquid was saturated sodium chloride solution the amount of barium chloride in the crystals was difficult to determine. A photo of the salt crystals (**Figure 6.7**) showed that indeed most of the crystals resembled the block shaped barium chloride crystals. With three washing steps 90 % of Ca, Mg, K, and Sr were removed from the crystals. It was concluded that there was no large buildup of impurities in the salt crystals.

At the same temperature (-23.4 °C) ice slurry was taken from the top of the crystallizer, filtered and washed two times with ultra-pure water. The ice samples were analyzed by ICP-OES (**Table 6.3**).

Figure 6.8 shows that the ice crystals are irregular shaped with rounded sides, the typical hexagonal shapes were not observed perhaps due to ripening.

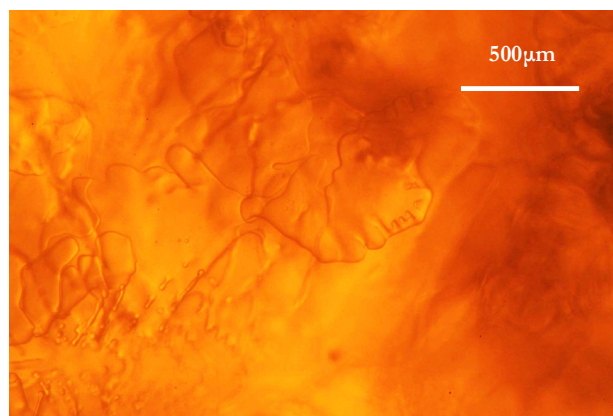


Figure 6.8 Ice crystals at -35 °C.

Table 6.3 shows that after 2 times washing 90 % of the impurities were removed from the ice crystals.

Produced water contains various trace elements next to the elements mentioned above. In order to test the impact of trace impurities upon the quality of the ice crystals the EFC experiment above was repeated with a selection of trace elements added to the starting solution (**Table 6.4**). No deviations relating to the crystallization process were observed to occur. The ice crystals were filtered and washed 5 times with water. The results of the experiment are presented in **Table 6.4**.

Table 6.4 shows that all trace elements remained in solution and were removed from the surface of the ice crystals by washing. Based upon these results it was concluded that elements do not build up measurably into the crystal lattice of the ice.

The analytical results also indicated that inclusions of mother liquor into the ice were on a very low level.

Since the purpose of a commercial process is to recover most of the salt and ice, the amount of salt and ice formation as a function of temperature was experimentally determined. Starting point was the same synthetic solution used for the first experiment. This solution was cooled down in the 10 liter crystallizer. At temperature intervals the scraper was stopped and a solution sample was taken through a glass filter from the crystal slurry. The composition of the solution was determined by Ion Chromatography (Mondal et al.) because IC is robust with respect to matrix effects. The concentration of the elements in solution as a function of temperature is presented in **Figure 6.9**. The cumulative concentration change as a function of temperature is presented in **Figure 6.10**.

Table 6.4 The effect of washing on the impurity content (in mg/kg) of the ice product.

| Element | Ba | Na | Ca | Sr | K | Mg | Cl | |
|--------------------------------|-------|-------|-------|------|------|------|--------|------|
| Start solution | 15000 | 57000 | 25000 | 8300 | 675 | 2100 | 150000 | |
| Ice after filtration | 10000 | 37050 | 15500 | 7055 | 820 | 1512 | 69000 | |
| Ice after 1 st wash | 7950 | 24510 | 9750 | 3486 | 405 | 777 | 40500 | |
| Ice after 2 nd wash | 2250 | 7410 | 3000 | 1079 | 94 | 231 | 12000 | |
| Ice after 3 rd wash | 1050 | 3420 | 1500 | 498 | 33 | 105 | 6000 | |
| Ice after 4 th wash | 450 | 1140 | 500 | 249 | 16 | 43 | 3000 | |
| Ice after 5 th wash | 150 | 570 | 250 | 83 | 7 | 21 | 1500 | |
| Element | Ag | Al | B | Bi | Cd | Co | Cr | Cu |
| Start solution | 7.8 | 16.7 | 16.1 | 14.5 | 13.7 | 14.5 | 13.8 | 14.4 |
| Ice after filtration | 9.1 | 10.4 | 10.8 | 10.2 | 8.6 | 8.8 | 8.6 | 9.7 |
| Ice after 1 st wash | 3.5 | 6.1 | 6.0 | 5.3 | 5.0 | 5.3 | 4.9 | 5.2 |
| Ice after 5 th wash | 0.1 | 0.8 | 0.3 | 0.0 | 0.1 | 0.2 | 0.1 | 0.1 |
| Element | Fe | Ga | In | Mn | Ni | Pb | Ti | Zn |
| Start solution | 13.9 | 14.2 | 18.1 | 23.3 | 13.2 | 15.8 | 14.8 | 15.1 |
| Ice after filtration | 8.4 | 8.9 | 13.3 | 14.5 | 7.9 | 9.0 | 10.3 | 8.4 |
| Ice after 1 st wash | 5.0 | 5.0 | 6.8 | 8.3 | 4.7 | 8.0 | 5.6 | 5.2 |
| Ice after 5 th wash | 0.1 | 0.1 | 0.2 | 0.2 | 0.1 | 0.1 | 0.1 | 0.8 |

Figures 6.9 and 6.10 show that ice crystallization had started at -18 °C because all salt concentrations started to increase at that point. At -20 °C the barium chloride concentration started to decrease significantly indicating the crystallization of barium chloride and the position of the eutectic point for BaCl₂ in this system. The barium chloride concentration at this point was 10 times below that of the eutectic concentration of the pure system (Tables 6.5 and 6.6). The much lower solubility of barium chloride is due to the common ion effect plus the effect of the other dissolved salts on the water activity.

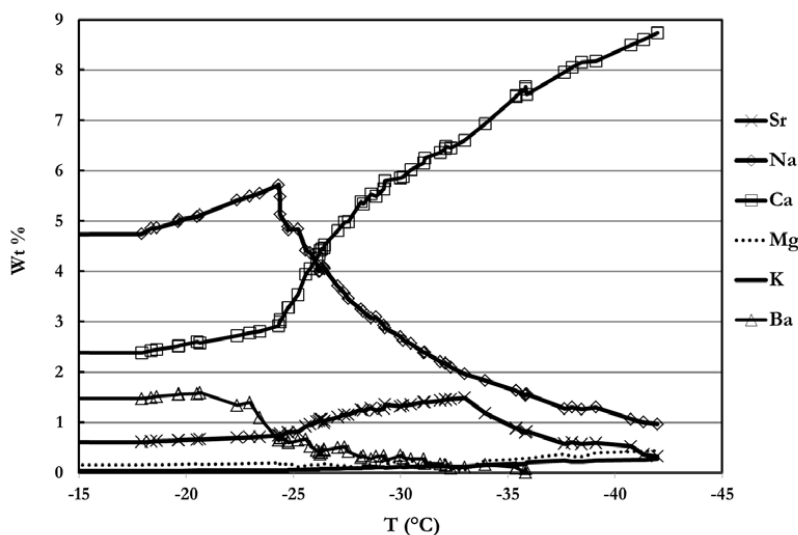


Figure 6.9 Composition of the solution as a function of temperature.

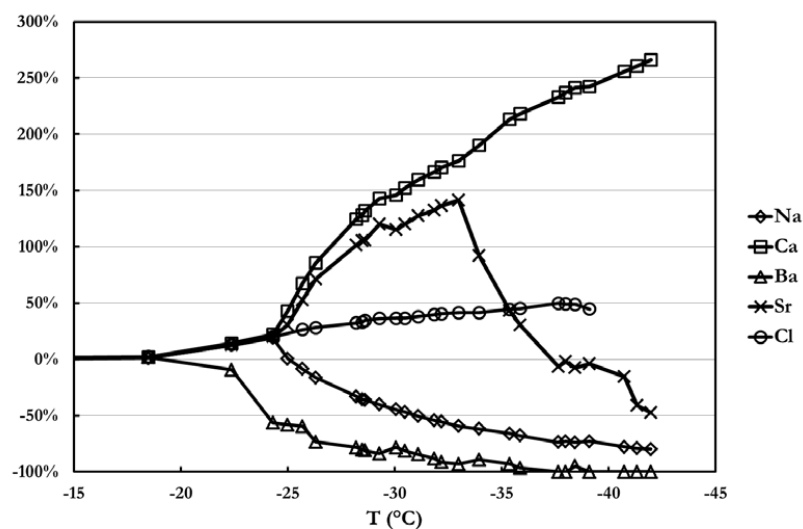


Figure 6.10 Cumulative concentration change (wt%) of each element as a function of temperature.

Table 6.5 Composition of the solution at different temperatures.

| T °C | NaCl | CaCl ₂ | BaCl ₂ | SrCl ₂ | MgCl ₂ | total |
|---------|------|-------------------|-------------------|-------------------|-------------------|-------|
| | wt% | | | | | |
| -20.6 | 13 | 7 | 2.4 | 1.2 | 0.7 | 24.3 |
| -24.3 | 13.7 | 7.6 | 1 | 1.34 | 0.73 | 24.3 |
| -33 | 5 | 18.2 | 0.25 | 1.1 | 0.9 | 25.4 |
| -42 | 2.5 | 23.8 | 0.07 | 0.5 | 1.7 | 28.6 |

Table 6.6 Eutectic temperature and composition of the binary systems.

| | NaCl | CaCl ₂ | BaCl ₂ | SrCl ₂ | MgCl ₂ |
|------------------------|-------|-------------------|-------------------|-------------------|-------------------|
| C _{eut.} (%) | 23.3 | 30 | 22.5 | 26 | 21.6 |
| T _{eut.} (°C) | -21.3 | -55 | -7.8 | -18.7 | -33.6 |

At -24.3 °C the eutectic point for sodium chloride was reached and sodium chloride started to crystallize from solution close to the eutectic point of the binary sodium chloride/water system (-21.3 °C). At -33 °C the eutectic point for strontium chloride was reached and strontium chloride started to crystallize from solution (**Figure 6.11**). The bar shaped crystals are strontium chloride, the large crystals with the rounded edges are sodium chloride and the small block shaped crystals are barium chloride. Low temperature X-ray diffraction might prove the crystal structure but was not within the scope of this research. The chance of formation of mixed salts is expected to be small because there is a tendency for a mixed salt to form single salts at lower temperature.

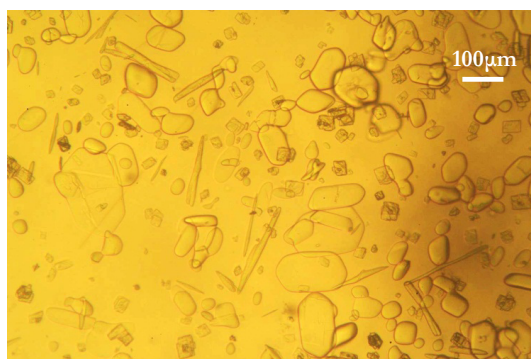


Figure 6.11 Salt crystals at -35 °C.

The composition of the starting solution determines the position of the eutectic points on the eutectic lines. If for instance the amount of barium chloride in the starting solution is increased the eutectic point for barium chloride will shift to a higher temperature. In a continuous process where the coolant is set to a given temperature, a changing composition of the flow back water will result in a different composition of the salt product. In that case the phase diagram of that specific solution can be used to predict the composition of the product. At -42 °C the solution contained 80 % calcium chloride and 20 % other salts. So the system was transformed from a solution containing mainly sodium chloride to a calcium chloride solution with minor impurities. As we can see from **Table 6.6**, the temperature upon further cooling will end up close to the eutectic point of pure calcium chloride just below -55 °C.

Figures 6.9 and 6.10 show that calcium chloride did not crystallize from solution so the calcium concentration in solution could be used to calculate the production of ice and salt as a function of temperature (**Figure 6.12**).

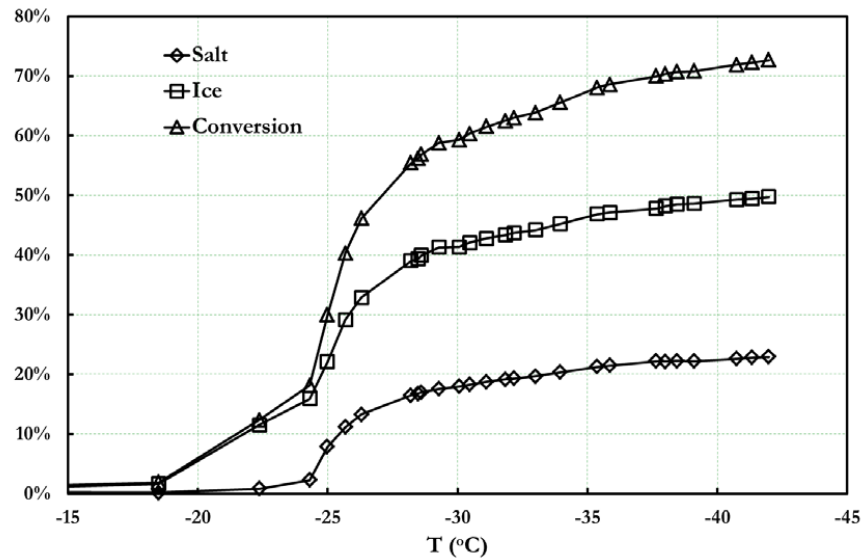


Figure 6.12 Conversion and the amounts of salts and ice produced as a function of temperature.

As can be seen from **Figure 6.12** with this specific composition 60 % of the starting solution can be recovered as salt and ice at -30 °C. In order to be able to recover 100 % the EFC process has to be run at -55 °C (the eutectic point of calcium chloride). Operating EFC at a higher temperature results in a lower conversion and a bleed stream that has to be processed further. Because at 100 % conversion all salts end up in the product the composition of the starting solution determines the composition of the salt recovered from a single stage EFC process. In this case varying concentrations of elements in the flow back water will have only a minor effect on the operating conditions of the EFC process because as long as an appreciable amount of Ca is present in the flow back water the process will run close to the eutectic point of calcium chloride.

The batch process with the synthetic solution described above was scaled up in a 200 liter scraped wall crystallizer. A heat transfer rate of 4 kW/m² over the heat exchangers could be maintained. No excessive scaling inside the crystallizer was observed.

From process point of view, different options to treat flow back water arise. The first one is freeze concentration of flow back water as an alternative for evaporative concentration. The resulting concentrated brine can be processed further. The second one is EFC of flow back water as an alternative for evaporative crystallization. In that case EFC can be run in single stage or in multiple stages making the isolation of separate salts possible. Another possibility is treatment of brine with

sodium sulfate to precipitate the divalent metals followed by separation of the solids and EFC of the resulting saline solution. An advantage of that option is that EFC will run at the eutectic point of sodium chloride at -21 °C (the eutectic point of sodium chloride) instead of the eutectic point of calcium chloride at -55 °C.

5 Conclusions

A synthetic solution mimicking flow back water from shale gas exploitation could be treated with freeze concentration and EFC. With freeze concentration the solution was transformed into pure ice and concentrated brine. The ice product was deemed sufficiently pure to be reused in fracking fluid. Because evaporative concentration is already applied on flow back water, freeze concentration of flow back water seems like an economically viable option. A batch EFC process transformed the stream into pure ice, a salt mixture and an optional bleed stream. The salt mixture was isolated by filtration and consisted mainly of barium chloride and some sodium chloride. The bleed stream contained the other salts. The batch process was scaled up in a 200 liter scraped wall crystallizer. A heat transfer rate of 4 kW/m² over the heat exchangers could be maintained. No excessive scaling inside the crystallizer was observed.

With the synthetic solution the eutectic points on the eutectic lines of BaCl₂ (-20.6 °C) NaCl (-24.3 °C) and SrCl₂ (-33 °C) were determined in an EFC batch experiment. At the end of the batch experiment the solution consisted of calcium chloride with minor impurities. The phase information from the batch experiment predicts that a single stage EFC process operating at the eutectic point of calcium chloride will result in the isolation of salt and ice without any bleed stream. In that case the salt composition of the product reflects the starting composition of the synthetic solution. Varying concentrations of elements in the flow back water will have only a minor effect on the EFC process. As long as an appreciable amount of Ca is present in the flow back water the process will run close to the eutectic point of calcium chloride. A multiple stage EFC process or a single stage EFC process at a higher temperature makes separation of different salt product fractions possible. The basic principle of EFC works for this type of process streams. Before industrial application is possible the EFC process has to be scaled up to further investigate relevant process steps like separation and filtration.

References

- Haluszczak, L.O., Rose, A.W. and Kump, L.R., 2013. Geochemical evaluation of flowback brine from Marcellus gas wells in Pennsylvania, USA. *Appl Geochem*, 28: 55-61.
- Hayes, T., 2009. Sampling and Analysis of Water Streams Associated with the Development of Marcellus Shale Gas <http://energyindepth.org/wp-content/uploads/marcellus/2012/11/MSCCommission-Report.pdf>.
- Hickenbottom, K.L. et al., 2013. Forward osmosis treatment of drilling mud and fracturing wastewater from oil and gas operations. *Desalination*, 312: 60-66.
- Himawan, C., Kramer, H.J.M. and Witkamp, G.J., 2006. Study on the recovery of purified MgSO₄ center dot 7H₂O crystals from industrial solution by eutectic freezing. *Sep Purif Technol*, 50(2): 240-248.
- Mondal, S., Hsiao, C.L. and Wickramasinghe, S.R., 2008. Nanofiltration/reverse osmosis for treatment of coproduced waters. *Environ Prog*, 27(2): 173-179.
- Pascual, M.R. et al., 2010. A novel scraped cooled wall crystallizer Recovery of sodium carbonate and ice from an industrial aqueous solution by eutectic freeze crystallization. *Chem Eng Res Des*, 88(9A): 1252-1258.
- Rahm, B.G. and Riha, S.J., 2012. Toward strategic management of shale gas development: Regional, collective impacts on water resources. *Environ Sci Policy*, 17: 12-23.
- Sirivedhin, T., McCue, J. and Dallbauman, L., 2004. Reclaiming produced water for beneficial use: salt removal by electrodialysis. *J Membrane Sci*, 243(1-2): 335-343.
- Stepakof, G.I., Siegelma, D., Johnson, R. and Gibson, W., 1974. Development of a Eutectic Freezing Process for Brine Disposal. *Desalination*, 15(1): 25-38.
- Swenne, D.A. and Thoenes, D., 1985. The eutectic crystallization of sodium chloride dihydrate and ice. *Journal of Separation Process Technology*, 6: 17-25.
- Van der Ham, F., 1999. PhD dissertation, Delft.
- van der Ham, F., Witkamp, G.J., de Graauw, J. and van Rosmalen, G.M., 1999. Eutectic freeze crystallization simultaneous formation and separation of two solid phases. *J Cryst Growth*, 198: 744-748.
- Van Spronsen, J. et al., 2010. Eutectic freeze crystallization from the ternary Na₂CO₃-NaHCO₃-H₂O system A novel scraped wall crystallizer for the recovery of soda from an industrial aqueous stream. *Chem Eng Res Des*, 88(9A): 1259-1263.
- Veil, J.A., 2010. Water Management Technologies Used by Marcellus Shale Gas Producers. http://fracfocus.org/sites/default/files/publications/water_management_in_the_marcellus.pdf.
- Warner, N.R., Christie, C.A., Jackson, R.B. and Vengosh, A., 2013. Impacts of Shale Gas Wastewater Disposal on Water Quality in Western Pennsylvania. *Environ Sci Technol*, 47(20): 11849-11857.

Chapter 7

Crystal Structure, Stability, and Electronic Properties of Hydrated Metal Sulfates $\text{MSO}_4(\text{H}_2\text{O})_n$ ($\text{M}=\text{Ni}, \text{Mg}$; $n=6,7$) and Their Mixed Phases: A First Principles Study

Changming Fang, **Xiaoqian Lu**, Wim Buijs, Zhaochuan Fan, Elif F. Genceli Güner, Marijn A. van Huis, Geert-Jan Witkamp, Thijs J. H. Vlugt, accepted by Chemical Engineering Science.

Abstract

Removal of Mg from hydrated Ni sulfates has long been a problem in the industrial purification process of hydrated Ni sulfates. In this work, we have investigated this industrial problem using state-of-the-art molecular simulations. Periodic Density Functional Theory (DFT) and cluster DFT calculations are used to study the crystal structures and phase stability of the hexahydrated and heptahydrated Ni and Mg sulfates and their mixed phases. The calculated lattice parameters of $\text{MSO}_4(\text{H}_2\text{O})_n$ ($\text{M}=\text{Ni}, \text{Mg}$; $n=6,7$) crystals are in good agreement with available experimental data. The relative energy differences of the mixed phase for both hexahydrated and heptahydrated Ni/Mg sulfates obtained from both the periodic and cluster DFT calculations are generally less than kT (25.8 meV, $T = 300$ K), indicating that a continuous solid solution is formed. We also investigated the Bader charges and electronic structures of the hexahydrated and heptahydrated Ni/Mg sulfates using the periodic DFT calculations. The energy band gaps of the hexahydrated and heptahydrated Ni and Mg sulfates were predicted by first-principles calculations. Large energy band gaps of about ~ 5.5 eV were obtained from the DFT-GGA calculations for hydrated Mg sulfates, and band gaps of about ~ 5.1 eV were obtained by the DFT-GGA+U calculations for hydrated Ni sulfates.

7.1 Introduction

Hydrated metal (II) sulfates, $MSO_4(H_2O)_n$ ($M=Ni, Mg$; $n=1\sim 11$) are widely used in different industrial processes. For instance, $NiSO_4(H_2O)_n$ -based solutions are commonly used in nickel plating, surface coating, super-capacitors, and highly efficient photocatalysts production (Carja et al., 2011; Dar et al., 2013; Lascelles et al., 2005; Patterson, 1994). While also be produced from nickel ore and from copper ore as a side product, most part of nickel sulfate is recovered from recycling products containing nickel. For producing solid phase nickel sulfate for commercial sale, crystallization is obligatory as the last step during producing process (Abbas et al., 2002; Moldoveanu and Demopoulos, 2002; Ramachandran et al., 1991) and highly pure nickel sulfate is usually required in applications. Among the most common impurities in solid nickel sulfate heptahydrate products, Mg is one impurity which is difficult to be removed because of the isomorphous replacement between Mg and Ni in $MSO_4(H_2O)_7$ (Smolik, 2000). Recent work on eutectic freeze crystallization showed that nickel sulfate heptahydrate can be recovered from industrial nickel sulfate streams with high purity, except for an accumulated Mg uptake in $NiSO_4(H_2O)_7$ crystals (Lu et al., 2014a). Afterwards, recrystallization of $NiSO_4(H_2O)_7$ obtained from eutectic freezing crystallization into $NiSO_4(H_2O)_6$ was used as a further purification process to remove Mg impurity. But according to experimental results (Lu et al., 2014b), this is a solvent mediated process, which means that the impurity content of Mg in the recrystallization liquid highly affects the final quality of product $NiSO_4(H_2O)_6$.

Hydrated metal (II) sulfates are not only of industrial interest, but are also commonly studied as model systems for their fundamental physical and chemical properties (Baur, 1964; Cox et al., 1955; Dar et al., 2013; Delorme et al., 2009; Grevel and Majzlan, 2009; Hawthorne, 2012; Koga and Tanaka, 1994; Lascelles et al., 2005; Maneva et al., 1990; Nesbitt et al., 2000; Nordstrom, 2009; Patterson, 1994; Squyres et al., 2004; Wells, 1984; Zalkin et al., 1964). The crystal structures and chemical bonds of Mg and Ni sulfate hexahydrates were measured by X-ray diffraction (Ptasiewicz-Bak et al., 1993; Zalkin et al., 1964) and an ionic model of $[Ni(H_2O)_6]^{2+}(SO_4)^{2-}$ was proposed (Ptasiewicz-Bak et al., 1993). Schlapp and Penney pointed out that, for a Ni^{2+} ion surrounded by an octahedron of negative ions or water molecules, the ground orbital state is a singlet (Schlapp and Penney, 1932). However, later this turned out to be erratic: all hydrated nickel sulfates and nitrates are paramagnetic (Swift and Connick, 1962). The magnetic properties of $NiSO_4(H_2O)_6$ have been intensively investigated by different experimental techniques (Fisher et al., 1967; O'Connor et al., 1941; Pontusch.Wm et al., 1973; Schlapp and Penney, 1932; Stout and Hadley, 1964; Watanabe, 1962). O'Connor et al. (1941) explored the magnetic rotatory power of crystalline nickel sulfate $NiSO_4(H_2O)_6$ in the ultraviolet region. The magnetic susceptibility of single crystals of $NiSO_4(H_2O)_6$ and $NiSO_4(H_2O)_7$ were measured in the temperature range between liquid He and room temperature (Watanabe, 1962). From the specific heat measurements of $NiSO_4(H_2O)_6$ single crystals between 1 K and 20 K, a peak was observed at 2.58 K (Stout and Hadley, 1964). Particularly important for

our study is the work of Benrath and Neumann (1939), who provided experimental evidence for the formation of a solid solution of $\text{Ni}_x\text{Mg}_{1-x}\text{SO}_4(\text{H}_2\text{O})_n$ ($x=0\sim1$; $n=6,7$). In addition, $\text{Ni}_{0.4}\text{Mg}_{0.6}\text{SO}_4(\text{H}_2\text{O})_6$ was reported being found in nature (Osborne, 1947).

The number of theoretical studies on Mg sulfate hydrates is limited. The thermoelastic properties of $\text{MgSO}_4(\text{H}_2\text{O})_7$ were recently studied using the density functional theory generalized gradient approximation (DFT-GGA) (Fortes et al., 2006). Luo et al. (2013) investigated absorption of water on MgSO_4 surfaces using GGA-DFT with the ultrasoft pseudopotential method. Separations between Mg and O surface atoms after water adsorption were observed in their modeling which indicated that deliquescence occurs on the MgSO_4 surfaces (Luo et al., 2013). Maslyuk et al. (2005) calculated crystal structures $\text{MgSO}_4\text{H}_2\text{O}$ using a combination of DFT and semiempirical methods, while the electronic structure of $\text{MgSO}_4\text{H}_2\text{O}$ was calculated by a hybrid density functional theory-Hartree-Fock (DFT-HF) approach. The calculated band gap for $\text{MgSO}_4\text{H}_2\text{O}$ was 7.77 eV, which are in agreement with experimentally determined band gap of 7.4 eV (Maslyuk et al., 2005). The configurations of isolated $\text{MgSO}_4(\text{H}_2\text{O})_n$ ($n=1,5$) molecules were optimized at a DFT PW91-TZ2P level (Iype et al., 2012). A proton transfer was found in $\text{MgSO}_4(\text{H}_2\text{O})_6$ (Iype et al., 2012), which we believe is an unrealistic erroneous result due to the single $\text{MgSO}_4(\text{H}_2\text{O})_6$ molecules chosen in these calculations (see our discussion in Section 7.2.2).

First-principles studies on Ni sulfate hydrates are even rarer in literature (Schröder et al., 2011). This is probably because of the difficulties in dealing with the Ni 3d state in the Ni-contained compounds. The relatively large systems of $\text{MSO}_4(\text{H}_2\text{O})_n$ (~ 100 atoms/unit cell) also make the computations very time-consuming. Due to the presence of the water molecules in the system, describing the dispersion interactions by DFT calculations is also difficult.

In this work, we study the crystal structure, phase stability and electronic structures of Ni and Mg sulfate hexahydrates and heptahydrates using state-of-the-art molecular simulations. The purpose of this study is threefold:

1. We are looking for a definite answer to the question which is arousing the interest of the hydrometallurgy industry: Can Mg incorporation in NiSO_4 products be prevented by recrystallization? Or do hydrated Ni and Mg sulfates form a continuous solid solution as suggested by Benrath and Neumann (1939)?
2. As mentioned above, first principles calculations on the hydrated Ni/Mg sulfates are very challenging. Using a combination of state-of-the-art energy functionals in the periodic DFT calculations, we aim to provide a trustful description of the physical interactions.
3. We are also exploring another molecular modeling approach, the DFT cluster calculations, which require less computational power and are therefore able to simulate larger systems or

to shorten the simulation time. A comparison between the periodic and cluster DFT calculations will be made.

The paper is structured as follow. Section 0 introduces the methods used in the periodic and cluster DFT calculations in detail. The crystals structures and the cluster models are also introduced. Section 7.3.1 presents the crystal structures and chemical bonding of hexahydrated and heptahydrated Ni/Mg sulfates calculated by both the periodic and cluster DFT calculations. Section 7.3.2 shows a comparison of the periodic and cluster DFT calculations of the relative stability of the $Ni_xMg_{1-x}SO_4(H_2O)_n$ ($n=6, 7$). Section 7.3.3 and 7.3.4 discuss Bader charges of atoms and the electronic structure of the $MSO_4(H_2O)_n$ from the periodic DFT calculations, respectively. Our conclusions are summarized in Section 7.4.

7.2 Methods

7.2.1 Periodic Density Functional Theory Calculations

In periodic DFT calculations, the projector-augmented wave (PAW) method (Blochl, 1994; Kresse and Joubert, 1999) was adopted. The first-principles code Vienna Ab-initio Simulations Package (VASP) (Kresse and Hafner, 1993; Kresse and Hafner, 1994) was employed for the structural optimizations and the electronic structure calculations. A nonlocal van der Waals density functional, optB86-vdW, was used in combination with the generalized gradient approximation (GGA) (Dion et al., 2004; Klimes et al., 2010; Klimes et al., 2011) to describe the exchange and correlation energy terms. This choice is based on two considerations: First, this newly developed correlation functional is based on the GGA approximation (Perdew et al., 1996) with the integration of the dispersion interactions, which is able to describe the hydrogen bonds of the water in the hydrated metal sulfates. Second, it has been established that GGA offers a better description of (spin-polarized) transition metals and compounds compared to the local (spin-polarized) density approximation (LDA), and it provides energetics of the compounds quite well (Amador et al., 1992; Fang et al., 2010). However, it is well known that the standard density functionals such as LDA and GGA fail to describe localized states (e.g. the Ni 3d states in NiO and NiSO₄) (Hubbard, 1963; Larsson, 2006; Madsen and Novak, 2005; Sawatzky and Allen, 1984). This deficiency can be solved by describing the on-site interactions of the localized 3d states with a simple parameter, the Hubbard U (Hubbard, 1963) with $U = 5.96$ eV for Ni 3d in NiO (Madsen and Novak, 2005).

The crystal models of $MSO_4(H_2O)_n$ ($M=Ni, Mg$; $n=6, 7$) were constructed on the basis of the available experimental data (Baur, 1964; Frondel and Palache, 1949; J.M. Kavitha and Mahadevan, 2013; Zalkin et al., 1964). For the $MSO_4(H_2O)_6$, two diferent phases, i.e. T (space group: P4₁2₁2) and m (space group: C2/c), were taken into consideration. Although the T-MgSO₄(H₂O)₆ and m-NiSO₄(H₂O)₆ are not stable in nature, their lattice parameters can be obtained by DFT optimization of Ni- and Mg-substituted T-

$\text{MgSO}_4(\text{H}_2\text{O})_6$ and $\text{m-NiSO}_4(\text{H}_2\text{O})_6$ unit cells, respectively. Beside the hydrated metal sulfates, several related compounds were also studied through the periodic DFT calculations for validation and comparison. These related compounds included MO, α - and β - MSO_4 , and ice_XI. the crystal sturctures of all materials involved are shown in **Figure 7.1**.

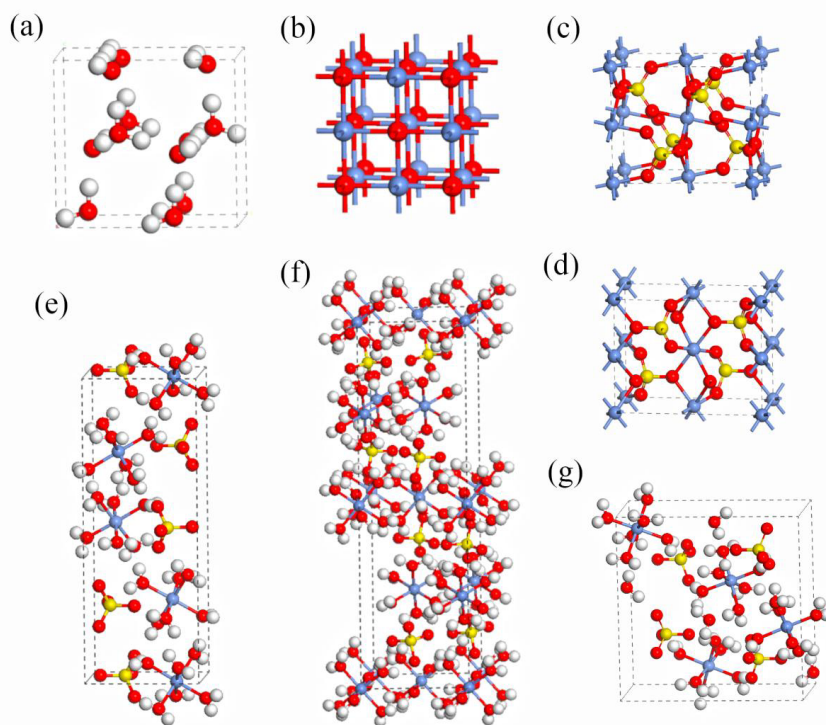


Figure 7.1 Schematic representation of crystal structures for (a) ice_XI, (b) MO, (c) α - MSO_4 , (d) β - MSO_4 , (e) T- $\text{MSO}_4(\text{H}_2\text{O})_6$, (f) m- $\text{MSO}_4(\text{H}_2\text{O})_6$, (g) $\text{MSO}_4(\text{H}_2\text{O})_7$. The white, red, gray, and yellow spheres are H, O, M (Ni or Mg), and S, respectively.

In the periodic DFT calculations, we used a cut-off energy of 600 eV for the wave functions and 850 eV for the augmentation functions. These high cut-off energies are necessary to accurately describe the localized Ni 3d states and the O 2p-S 3p and O sp-H 1s strong-bonding in the compounds. The electronic wave functions were sampled on a $6 \times 6 \times 2$ Monkhorst-Pack (MP) grid (Monkhorst and Pack, 1976) with 18 to 36 k-points and a $8 \times 4 \times 4$ MP grid with 16-64 k-points in the irreducible Brillouin zone (BZ) for the T- $\text{MSO}_4(\text{H}_2\text{O})_6$ and O- $\text{MSO}_4(\text{H}_2\text{O})_7$ phases, respectively. For the calculations of local electronic configurations and partial density of states of the atoms, the Wigner-Seitz (WS) radius was set as 1.2 Å for Ni and Mg, 0.9 Å for O and S and 0.4 Å for H, respectively. Note that the 3d electrons of the Ni atom

exhibit an itinerant character in the metals and their nitrides, in principle belonging to the whole crystal. However, we can decompose the plane waves in the atomic WS sphere and obtain Ni 3d components in the spheres for both the spin-up (or majority) and spin-down (minority) directions. In this way, a local magnetic moment is obtained from the difference between the number of spin-up and spin-down electrons in the WS sphere. The choices of the MP k-meshes and cut-off energies are based on convergence tests in which the energy convergence is kept below 1 meV/atom.

7.2.2 Cluster Density Functional Theory Calculations

The commercially available Spartan 14 package (Wavefunction Inc., Irvine, California, USA. www.wavefun.com) was used for all cluster calculations. The routine B3LYP/6-31G* for DFT calculations were used. Despite its known incapability of describing particularly van der Waals interactions correctly, or depicting electronic (fine) structure more generally, both energies and geometrical structures are usually reproduced quite well (Hehre, 2003). Typical bond length errors are less than 0.02 Å. All metal sulfate hydrates display strong static electrostatic behaviour, both in the $M(H_2O)_6$ cation and the sulfate anion, which should be adequately covered by B3LYP. Furthermore, by direct comparison of the total energies of very similar complexes, a cancellation of possible errors in the van der Waals interactions can be expected. Finally, it should be noted that the cluster calculations presented herein are only to be used for comparing their relative energies and geometries, but not for the determination of bulk electronic structure features of the solid state materials.

To set up meaningful comparisons with respect to geometry and total energy, clusters were selected from the known crystal structures of both $MgSO_4(H_2O)_6$ and $NiSO_4(H_2O)_7$. **Figure 7.2b** shows a tetrameric cluster from the unit cell of T- $MgSO_4(H_2O)_6$ containing four $Mg(H_2O)_6^{2+}$ cations and four sulfates. Geometry optimization of this tetrameric cluster leads to proton transfer from the M coordinated water molecules to the sulfate anion. The same type of proton transfer was reported also by (Iype et al., 2012) using a different DFT code. However, obviously this is an erroneous result due to the fact that the cluster shows a too large charge separation between the $Mg(H_2O)_6^{2+}$ cations and the sulfate anions at the border of the parent unit cell. The crystal structure does not show an indication for such a proton transfer. Therefore, we took the dimeric cluster for $MgSO_4(H_2O)_6$ (see **Figure 7.2c**), wherein the two sulfates are stabilized by H-bridges of the water molecules coordinated to the M^{2+} cations. In case of $NiSO_4(H_2O)_7$, the tetrameric unit cell could be directly chosen (see **Figure 7.2d**), as inside this unit cell there is sufficient hydrogen bridging towards the sulfate anions to avoid the previously-mentioned proton transfer.

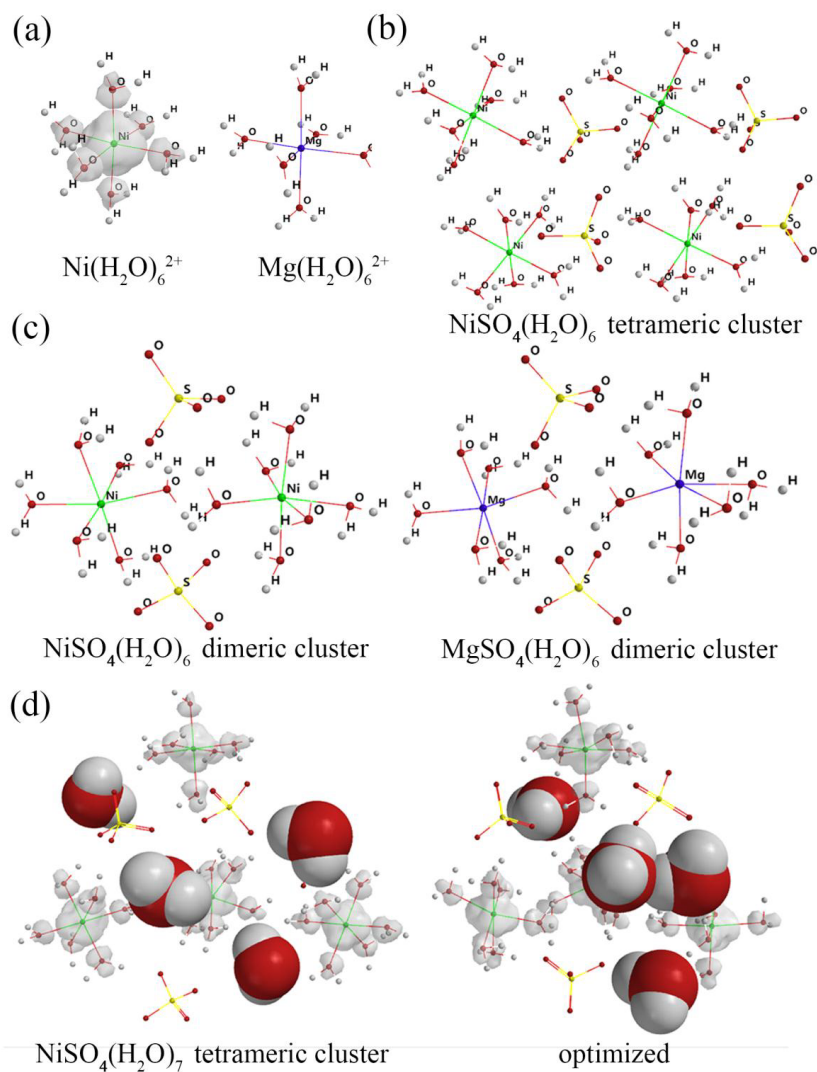


Figure 7.2 Constructed and B3LYP-optimized clusters of (a) $\text{Ni}(\text{H}_2\text{O})_6^{2+}$ and $\text{Mg}(\text{H}_2\text{O})_6^{2+}$ with spin densities on $\text{Ni}(\text{H}_2\text{O})_6^{2+}$ ($0.002e/\text{au}^3$), (b) optimized tetrameric NiSO_4 , (c) Dimeric $\text{MSO}_4(\text{H}_2\text{O})_6$ clusters, (d) unit cell of $\text{NiSO}_4(\text{H}_2\text{O})_7$ (left) and optimized tetrameric cluster (right) with spin densities on $\text{Ni}(\text{H}_2\text{O})_6^{2+}$ ($0.002e/\text{au}^3$). The white, red, green, purple, and yellow spheres are H, O, Ni, Mg, and S, respectively. Four free water molecules (see the main text) are shown in the vdW presentation.

7.3 Results and discussion

7.3.1 Structures and chemical bonds

Before discussing the hydrated Ni and Mg sulfates, we discuss the periodic DFT calculations on reference compounds (MO, α - and β - MSO_4 , and ice_XI) for validation and comparison. **Table 7.1** lists the lattice parameters of these compounds calculated using the periodic DFT calculations in comparison with available experimental data. In general, the calculated lattice parameters of all the related compounds are in good agreement with experimental data with deviations less than 4%. Therefore, the computational schemes used here are suitable for the studies of these reference compounds, thus, are also expected to be suited to the hydrated Ni and Mg sulfates and their mixed phases.

Table 7.1 Calculated lattice parameters for ice_XI, MgO, $MgSO_4$, NiO, and $NiSO_4$ from the periodic DFT calculations and available experimental data. The lattice parameters a , b and c are in Å.

| Compound | Space Group (Nr.) | | Bulk calc. | Exp. |
|---------------------|-------------------|-----|--------------------------|---|
| Ice_XI | $Cmc2_1$ (36) | a | 4.343 | 4.5019 ^a |
| | | b | 7.609 | 7.7978 ^a |
| | | c | 7.035 | 7.3280 ^a |
| MgO | $Fm-3m$ (225) | a | 4.235 | 4.13 ^b |
| α - $MgSO_4$ | $Cmcm$ (63) | a | 5.223 | 5.1686 ^c |
| | | b | 7.863 | 7.8678 ^c |
| | | c | 6.442 | 6.5667 ^c |
| β - $MgSO_4$ | $Pnma$ (62) | a | 8.654 | 8.5817 ^c |
| | | b | 6.667 | 6.6727 ^c |
| | | c | 4.743 | 4.7343 ^c |
| NiO | $Fm-3m$ (225) | a | 4.156/4.203 ^g | 4.1705 ^d |
| α - $NiSO_4$ | $Cmcm$ (63) | a | 5.196/5.195 ^g | 5.188 ^e , 5.155 ^f |
| | | b | 7.840/7.816 ^g | 7.848 ^e , 7.842 ^f |
| | | c | 6.267/6.290 ^g | 6.300 ^e , 6.338 ^f |
| β - $NiSO_4$ | $Pnma$ (62) | a | 8.615/8.613 ^g | |
| | | b | 6.460/6.464 ^g | |
| | | c | 4.720/4.721 ^g | |

- a. experimental report in Ref. (Leadbetter et al., 1985)
- b. experimental report in Ref. (Wyckoff, 1921)
- c. experimental report in Ref. (Fortes et al., 2007) (at 4.2 K)
- d. experimental report in Ref. (Bartel and Morosin, 1971) (extended to 0 K)
- e. experimental report in Ref. (Wildner, 1990)
- f. experimental report in Ref. (Frazer and Brown, 1962)
- g. DFT+U with U = 5.96 eV (see main text)

The lattice parameters of m- $MSO_4(H_2O)_6$, T- $MSO_4(H_2O)_6$, and $MSO_4(H_2O)_7$ obtained from the periodic DFT calculations are listed in Fout! Verwijzingsbron niet gevonden. together with available experimental data. The computed lattice parameters for all the hydrated Ni and Mg sulfates phases show good agreement with the available experimental data. The highest deviation from the experimental data is 3.1 % in the length of the a -axis of O- $MgSO_4(H_2O)_7$ (Epsom salt). **Table 7.3** shows the chemical bond lengths

in these hydrated Ni and Mg sulfates and their related compounds from the periodic DFT calculations. In all the solid phases, both Ni and Mg atoms/ions are in an octahedral coordination with oxygen atoms/ions, with bond-lengths of about 1.99 - 2.25 Å for Mg-O and 1.99 - 2.21 Å for Ni-O. In both Mg and Ni sulfates, each S atom/ion is tetragonally coordinated by four oxygen atoms/ions with the S-O interatomic distances ranging from 1.46 to 1.52 Å, revealing a high stability of (SO₄)²⁻ clusters in the ionic model. The calculated O-H bond lengths vary slightly around 0.99 Å.

Table 7.2 Calculated lattice parameters for hydrated metal sulfates from the periodic DFT calculations and available experimental data. The lattice parameters *a*, *b* and *c* are in Å.

| Compound | Space Group (Nr.) | | Calc. | Exp. |
|---|--|----------|----------------------------|---------------------|
| m-MgSO ₄ ·(H ₂ O) ₆ (Hexahydrate) | <i>C2/c</i> (15) | <i>a</i> | 9.883 | 10.110 ^a |
| | | <i>b</i> | 7.282 | 7.212 ^a |
| | | <i>c</i> | 24.005 | 24.41 ^a |
| | | β | 98.34° | 98.30 ^a |
| T-MgSO ₄ ·(H ₂ O) ₆ | <i>P4₁2₁2</i> (92) | <i>a</i> | 6.794 | |
| | | <i>c</i> | 18.068 | |
| MgSO ₄ ·(H ₂ O) ₇ (Epsom salt) | <i>Cmcm</i> (63) | <i>a</i> | 6.646 | 6.858 ^b |
| | | <i>b</i> | 11.810 | 11.86 ^b |
| | | <i>c</i> | 11.943 | 11.99 ^b |
| m-NiSO ₄ ·(H ₂ O) ₆ | <i>C2/c</i> (15) | <i>a</i> | 9.830/9.845 ^c | |
| | | <i>b</i> | 7.102/7.238 ^c | |
| | | <i>c</i> | 23.416/24.025 ^c | - |
| | | β | 98.67°/98.70° ^c | |
| T-NiSO ₄ ·(H ₂ O) ₆ (Retgersite) | <i>P4₁2₁2</i> (92) | <i>a</i> | 6.755/6.761 ^c | 6.765 ^c |
| | | <i>c</i> | 17.936/18.002 ^c | 18.20 ^c |
| NiSO ₄ ·(H ₂ O) ₇ (Morenosite) | <i>Cmcm</i> (63) | <i>a</i> | 6.601/6.608 ^c | 6.712 ^d |
| | | <i>b</i> | 11.737/11.758 ^c | 11.86 ^d |
| | | <i>c</i> | 11.863/11.861 ^c | 11.99 ^d |

- a. experimental report in Ref. (Zalkin et al., 1964)
- b. experimental report in Ref. (Baur, 1964)
- c. experimental report in Ref. (Fronzel and Palache, 1949)
- d. experimental report in Ref. (J.M. Kavitha and Mahadevan, 2013)
- e. DFT+U with U = 5.96 eV (see main text)

In line with the periodic DFT calculations, structural optimizations of the hydrated metal sulfate clusters by cluster DFT calculations yield octahedral Ni(H₂O)₆²⁺ and Mg(H₂O)₆²⁺ cations, as well as sulfate anions. **Figure 7.2a** shows both the octahedral coordination in Ni(H₂O)₆²⁺ and Mg(H₂O)₆²⁺ and the triplet spin state of the simple Ni(H₂O)₆²⁺ cation. The volumes of these two cations are 118.08 Å³, and 119.54 Å³ respectively, which differ less than 1%. Consequently, Mg-O bonds are slightly larger than Ni-O bonds: Mg-O = 2.120 Å and Ni-O = 2.077 Å. This similarity in shape and volume can be considered as an indication for a continuous solid solution.

Table 7.3 Calculated chemical bonds in hydrated metal sulfates and related compounds from both periodic and cluster DFT calculations. All bond lengths are in Å.

| Phase | Bonds | Periodic DFT calc. | Cluster DFT calc. |
|--|-------|-----------------------------------|--------------------|
| Ice_XI | H-O | 1.01 (×2) | - |
| MgO | Mg-O | 2.14 (×6) | - |
| NiO | Ni-O | 2.08 (×6) | - |
| α -MgSO ₄ | Mg-O | 2.03 (×2), 2.14 (×4) | - |
| | S-O | 1.46 (×2), 1.51 (×2) | - |
| α -NiSO ₄ | Ni-O | 2.02 (×2), 2.10 (×4) | - |
| | S-O | 1.46 (×2), 1.52 (×2) | - |
| β -MgSO ₄ | Mg-O | 1.99 (×2), 2.11 (×2), 2.25 (×2) | - |
| | S-O | 1.46 (×2), 1.49, 1.50 | - |
| β -NiSO ₄ | Ni-O | 1.99 (×2), 2.06 (×2), 2.21 (×2) | - |
| | S-O | 1.46 (×2), 1.51, 1.52 | - |
| m-MgSO ₄ ·(H ₂ O) ₆ | Mg-O | 2.06 (×2), 2.08 (×2), 2.09 (×2) | - |
| | S-O | 1.48, 1.49 (×2), 1.50 | - |
| m-NiSO ₄ ·(H ₂ O) ₆ | Ni-O | 2.06 (×2), 2.07 (×2), 2.08 (×2) | - |
| | S-O | 1.48, 1.49 (×2), 1.50 | - |
| T-MgSO ₄ ·(H ₂ O) ₆ | Mg-O | 2.02 (×2), 2.09 (×2), 2.11 (×2) | 2.112 ^a |
| | S-O | 1.49 (×4) | 1.520 ^a |
| | H-O | 0.98~1.00 | - |
| T-NiSO ₄ ·(H ₂ O) ₆ | Ni-O | 2.02 (×2), 2.08 (×2), 2.09 (×2) | 2.083 ^a |
| | S-O | 1.49 (×4) | 1.520 ^a |
| | H-O | 0.99~1.00 | - |
| MgSO ₄ ·(H ₂ O) ₇ | Mg-O | 2.05 (×2), 2.06, 2.07, 2.11, 2.14 | 2.110 ^a |
| | S-O | 1.47, 1.48, 1.49, 1.51 | 1.520 ^a |
| | H-O | 0.98~1.00 | - |
| NiSO ₄ ·(H ₂ O) ₇ | Ni-O | 2.04, 2.05 (×3), 2.08, 2.12 | 2.078 ^a |
| | S-O | 1.47, 1.48, 1.49, 1.51 | 1.520 ^a |
| | H-O | 0.99~1.01 | - |

a. Average value for all chemical bonds.

The average Ni-O bond length of the dimeric clusters (MSO₄(H₂O)₆) is slightly larger than the Ni-O bond length in the crystal structure: 2.083 Å (cluster) vs 2.051 Å (crystal). For the S-O bond lengths a similar observation can be obtained: 1.520 Å (cluster) vs 1.481 Å (crystal). Mg-O distances in the clusters are 2.111 Å. In the full Ni cluster the Ni-Ni atomic distance is 6.258 Å, while in the full Mg cluster the Mg-Mg atomic distance is 6.286 Å. The volumes of the dimeric clusters are in line with the bond length observations: the volume of the dimeric Ni cluster is 375.52 Å³ while the volume of dimeric Mg cluster is 379.12 Å³. Ni and Mg dimeric clusters have a similar geometry.

As is shown in **Figure 7.2d**, the B3LPY-optimized NiSO₄(H₂O)₇ tetrameric structure shows a slightly decreased volume compared to the initial unit cell, due to the lack of attractions from the surrounding atoms which are no longer present in the cluster. It can be concluded that the cluster calculation yields correct results with respect to the overall spin state of the tetrameric Ni(H₂O)₇SO₄ with 8 unpaired electrons (Swift and Connick, 1962). The results are in line with literature which states that all Ni(H₂O)_nSO₄ phases are paramagnetic (Swift and Connick, 1962). As is shown in **Table 7.3**, the average

Ni-O bond length of the B3LYP-optimized cluster is slightly larger than the Ni-O bond length in the crystal structure: 2.078 Å (cluster) vs 2.065 Å (crystal). For the S-O bond lengths a similar observation can be made: 1.520 Å (cluster) vs 1.488 Å (crystal). The average Ni-Ni distance is 6.504 Å in the crystal and 5.546 Å for the optimized cluster. The volumes of the clusters are: $V_{\text{crystal}} = 862.97 \text{ Å}^3$ and $V_{\text{optimised-cluster}} = 826.48 \text{ Å}^3$, the latter being considerably smaller than the former. The main reason for the much lower volume of the optimised cluster is, the rather large displacement of the four free water molecules from the side of the crystal towards the inside of the cluster. This can be explained by the fact that contrary to the real crystal, the cluster does not see its neighbouring cells.

The B3LYP-optimized full Mg clusters yield similar results as the full Ni clusters (**Table 7.3**). The average Mg-O bond length of the full Mg tetrameric cluster is 2.110 Å while the average from the periodic DFT calculations is 2.080 Å. The average S-O bond lengths are again 1.520 and 1.488 Å from the cluster and periodic DFT calculations, respectively. The average Mg-Mg distance is 5.631 Å. The volume of the full Mg cluster is 834.38 Å³, slightly larger than the volume of the all Ni-cluster.

7.3.2 Phase stabilities

In order to assess the relative stability of the mixed phases $(\text{Ni}_x\text{Mg}_{1-x})\text{SO}_4(\text{H}_2\text{O})_n$ ($x = 0\sim 1$; $n = 6,7$), the relative energy difference (ΔE) is defined as:

$$\begin{aligned} \Delta E[(\text{Ni}_x\text{Mg}_{1-x})\text{SO}_4(\text{H}_2\text{O})_n] \\ = E[(\text{Ni}_x\text{Mg}_{1-x})\text{SO}_4(\text{H}_2\text{O})_n] - x E[\text{NiSO}_4(\text{H}_2\text{O})_n] - (1-x) E[\text{MgSO}_4(\text{H}_2\text{O})_n] \end{aligned}$$

Here, the relative energy difference ΔE and the absolute energy E could either be the formation energy in the periodic DFT calculations or the total energy in the cluster DFT calculations.

In the periodic DFT calculations, considering the strong similarity of local structures between the T and m phases, only the T- $\text{MSO}_4(\text{H}_2\text{O})_6$ structure was considered for the stability comparison of the hexahydrate Ni and Mg sulfates. In the hydrate metal sulfates, the distances between metal atoms/ions are very large, typically larger than 5 Å. Such long metal-metal distances indicate weak exchange interactions and small energy differences between different configurations. Therefore, only one possible configuration of the mixed phase, $(\text{Ni}_x\text{Mg}_{1-x})\text{SO}_4(\text{H}_2\text{O})_n$, was calculated. At 0 K, the enthalpy difference is equal to the energy difference, $\Delta G = \Delta E$, where we ignore the zero-point vibration contribution.

The relative Gibbs free energy difference for $(\text{Ni}_x\text{Mg}_{1-x})\text{SO}_4(\text{H}_2\text{O})_n$ ($n=6,7$) obtained by the periodic DFT calculations are shown in **Figure 7.3**. Note that the density-functional theory only works for the ground states of materials, i.e. it describes the total valence electron energy at 0 K. As shown in **Figure 7.3**, the relative energy differences of the mixed phases with respect to the pure hydrate metal sulfates at 0 K are

rather small (typically about a few meV/f.u.). This can be understood as the consequence of the long atomic distances and the weak exchange interactions between metals. These results are in line with experiments that a magnetic ordering occurs at very low temperatures (2~3 K) (Maslyuk et al., 2005).

At elevated temperatures, configuration entropy plays a more important role in the free energy of the system. The weak interactions between the metal ions suggest that a random model for the configurations for the alloying phases can be used as a correction for the Gibbs free energy calculations. We considered a unit cell containing four metal ions. The configuration number (W) for one unit cell is 4 for $Ni_{0.25}Mg_{0.75}SO_4(H_2O)_n$ and $Ni_{0.75}Mg_{0.25}SO_4(H_2O)_n$, and is 6 for $Ni_{0.5}Mg_{0.5}SO_4(H_2O)_n$. The correction of the configuration entropy, $S = k \ln W$ (per unit cell), was included to estimate the free energies of the mixed phases at finite temperatures. It is suggested in **Figure 7.3** that the mixed phases with different fractions of Ni can be formed at room temperature (300 K). Note that our calculations also show an unstable $(Ni_{0.25}Mg_{0.75})SO_4(H_2O)_7$ phase with a relatively large positive energy difference (~ 11 meV/f.u.). Considering the small energy differences (~ 40 meV) and the large number (88~108) of atoms per unit cell, we believe this exception is just a marginally numerical error. The result of our periodic DFT calculations indicates that it is difficult to obtain hydrated Ni sulfate of high purities by recrystallizing Ni sulfates liquids with Mg^{2+} contamination at ambient conditions.

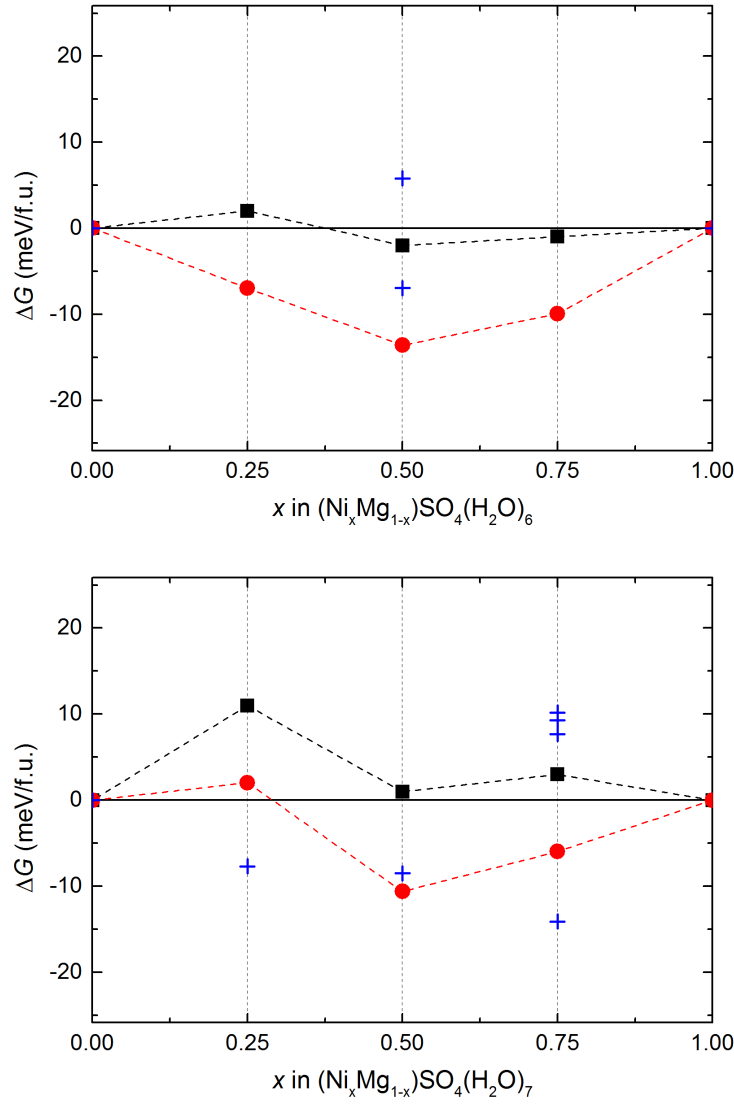


Figure 7.3 Relative stability of (a) $(\text{Ni}_x\text{Mg}_{1-x})\text{SO}_4(\text{H}_2\text{O})_6$ and (b) $(\text{Ni}_x\text{Mg}_{1-x})\text{SO}_4(\text{H}_2\text{O})_7$ calculated by periodic and cluster DFT calculations. The black squares are the relative formation energy difference ΔE from periodic DFT calculations at 0 K ($\Delta G = \Delta E$, the zero-point vibration energy is ignored); The red circles are those at 300 K with consideration of configuration entropy correction; The blue crosses are the relative total energy difference ΔE from cluster DFT calculations at 0 K ($\Delta G = \Delta E$, the zero-point vibration energy is considered). The scale of the y axes is from 25.85 to -25.85 meV/f.u., corresponding to the value of kT at 300 K.

The typical computing time for a similar system (same number of atoms) by the cluster DFT calculations (about one day for a tetrameric cluster) is one tenth of that by the periodic DFT calculations (more than one week for one unit cell). Therefore, we investigated the relative stabilities of a mixed phase of hydrate metal sulfates with more possible configurations in the cluster DFT calculations. For the mixed phases of the dimeric clusters (hexahydrate metal sulfates), both possible $Ni_{0.5}Mg_{0.5}(H_2O)_6SO_4$ configurations were chosen, while for the mixed phases of the tetrameric clusters (heptahydrate metal sulfates), all possible four $Ni_{0.75}Mg_{0.25}(H_2O)_7SO_4$ clusters, one $Ni_{0.5}Mg_{0.5}(H_2O)_7SO_4$ clusters, and one $Ni_{0.25}Mg_{0.75}(H_2O)_7SO_4$ clusters were chosen for full optimization and energy calculation. In the $Ni_{0.5}Mg_{0.5}(H_2O)_6SO_4$ dimeric clusters, the averaged Ni-Mg distance in the mixed clusters is 6.260 Å, slightly larger than the Ni-Ni distance (6.258 Å) in the full Ni dimeric cluster and smaller than the Mg-Mg distance (6.286 Å) in the full Mg dimeric cluster. The optimized volume of these $Ni_{0.5}Mg_{0.5}(H_2O)_6SO_4$ clusters (377.20 Å³) is also between that of the full Ni dimeric cluster (375.52 Å³) and the full Mg dimeric cluster (379.12 Å³). All of them are very similar, but increase with Mg concentration. In the optimized mixed phases of the tetrameric clusters, the average Ni-O bond length in the various clusters is 2.078 Å, The average Mg-O bond length is 2.110 Å, and the average S-O bond length is 1.520 Å. The calculated volumes of the $Ni_{0.75}Mg_{0.25}(H_2O)_7SO_4$, $Ni_{0.5}Mg_{0.5}(H_2O)_7SO_4$, and $Ni_{0.25}Mg_{0.75}(H_2O)_7SO_4$ clusters are 828.26 (averaged), 830.80, and 832.42 Å³, respectively, perfectly in line with the results for the all Ni- and all Mg-clusters. It is important to note that all 6 clusters remain visually intact, however slightly increasing in volume with increasing Mg-content. The larger deviation of the volume of the $M(H_2O)_7(SO_4)$ clusters from the original unit cell is due to the displacement of the seventh water molecule from the outside to the inside of the cluster, still maintaining the relative position of the octahedral $M(H_2O)_6^{2+}$ cation and the sulfate anion.

From cluster DFT calculations, it is clear that size and volume of the simple cations $Mg(H_2O)_6^{2+}$ and $Ni(H_2O)_6^{2+}$ are very similar, the former being slightly larger (~ 1%). This behaviour is consistently shown for the various dimeric and tetrameric clusters. However, cluster calculations cannot answer the question if partial or full isomorphous substitution of $Ni(H_2O)_6^{2+}$ by $Mg(H_2O)_6^{2+}$ is possible. Cluster calculations still can answer the question whether the solid phases can be mixed or form a continuous solid solution by comparing the ΔE with kT ($kT = 25.8$ meV, $T = 300$ K). The result from cluster calculations in **Figure 7.3** (blue crosses) provides an unambiguously answer to the question. Indeed, $\Delta E < kT$ for all cases studied. Therefore, the cluster DFT calculations are in full agreement with the periodic DFT calculations in that both $Ni_xMg_{1-x}SO_4(H_2O)_6$ and $Ni_xMg_{1-x}SO_4(H_2O)_7$ should form a continuous solid solution.

7.3.3 Charges and charge transfer

To better understand the chemistry of compounds, we calculated the charge of the ions/atoms and the charge transfer between them. In 1971, Bader and Beddal proposed an unambiguous definition of an atom/ion in a molecule/solid by dividing the molecule/solid into spatial regions defining the atoms. The

charge on an atom is determined by the number of electrons in its region (Bader and Beddall, 1971; Bader et al., 1981). The boundary of an atom is defined by the zero-flux surfaces between that atom and neighboring atoms. The Bader charges at the atomic/ionic sites in the related compounds from the periodic DFT calculations are listed in **Table 7.4**.

Table 7.4 Calculated Bader charges in hydrate metal sulfates and related compounds from the periodic DFT calculations. All charges are in e .

| Phase | Mg | Ni | S | O | H |
|--|------|------|------|---------------|-------------|
| Icc_XI | - | - | - | -1.30 ~ -1.31 | ~0.65 |
| MgO | 1.64 | - | - | -1.64 | - |
| NiO | - | 0.96 | - | -0.96 | - |
| α -MgSO ₄ | 1.71 | - | 3.90 | -1.36 ~ -1.45 | - |
| α -NiSO ₄ | - | 1.29 | 3.87 | -1.26 ~ -1.32 | - |
| β -MgSO ₄ | 1.71 | - | 3.91 | -1.38 ~ -1.41 | - |
| β -NiSO ₄ | - | 1.29 | 3.88 | -1.26 ~ -1.31 | - |
| m-MgSO ₄ ·(H ₂ O) ₆ | 1.63 | - | 3.47 | -1.16 ~ -1.29 | 0.58 ~ 0.65 |
| m-NiSO ₄ ·(H ₂ O) ₆ | - | 1.32 | 3.79 | -1.19 ~ -1.38 | 0.54 ~ 0.69 |
| T-MgSO ₄ ·(H ₂ O) ₆ | 1.70 | - | 3.83 | -1.31 ~ -1.38 | 0.64 ~ 0.69 |
| T-NiSO ₄ ·(H ₂ O) ₆ | - | 1.26 | 3.87 | -1.24 ~ -1.30 | 0.64 ~ 0.66 |
| MgSO ₄ ·(H ₂ O) ₇ | 1.70 | - | 3.81 | -1.29 ~ -1.37 | 0.65 ~ 0.68 |
| NiSO ₄ ·(H ₂ O) ₇ | - | 1.25 | 3.80 | -1.24 ~ -1.36 | 0.64 ~ 0.68 |

The Bader charges of each element are almost the same for the sulfates, sulfate hydrates, or monoxide. All Mg ions/atoms are more charged compared to the Ni atoms/ions in corresponding phases, which corresponds to the significantly larger electronegativity of Ni (1.91) than that of Mg (1.31) in the Pauling scale. All the S atoms/ions in the sulfates and their hydrates have almost the same Bader charges (+3.80 to 3.90 e) in spite of the difference between Ni and Mg compounds, which are in agreement with the difference in electronegativity, 2.58 for S less than 3.44 for O. According to the Bader charge analysis, the electronegativity of the (SO₄)²⁻ cluster is significantly higher than that of O from the comparison between MO and M(SO₄) (0.96 vs 1.27 for M=Ni and 1.6 vs 1.7 for M=Mg).

7.3.4 Electronic properties

Considering the significant structure differences (**Figure 7.1**), it is also interesting to investigate the electronic properties of the Mg and Ni oxides, sulfates, hexa-, and hepta-hydrates. The calculated total density states (tDOS) for the studied compounds are shown in **Figure 7.4**. **Figure 7.5**, the partial density of states (pDOS) of different atoms in selected phases. In **Table 7.5**, the electronic energy gaps of the compounds are also summarized and compared with the available experimental data.

Table 7.5 Calculated energy gaps for MO, MSO_4 ($M=Mg$ or Ni) and the hydrates from the periodic DFT calculations with comparison with available experimental data. The energy gaps are in eV.

| Phase | optB86-vdW | +U | Exp. |
|--|------------|------|-------------------|
| Ice_XI | 5.55 | - | 8.75 ^a |
| MgO | 5.25 | - | 7.8 ^b |
| NiO | 0 | 2.25 | 4.3 ^c |
| α -MgSO ₄ | 6.02 | - | - |
| α -NiSO ₄ | 1.02 | 3.56 | - |
| β -MgSO ₄ | - | - | - |
| m-MgSO ₄ ·(H ₂ O) ₆ | 5.56 | - | - |
| m-NiSO ₄ ·(H ₂ O) ₆ | 1.75 | 5.14 | - |
| T-NiSO ₄ ·(H ₂ O) ₆ | 1.86 | 5.05 | - |
| MgSO ₄ ·(H ₂ O) ₇ | 5.68 | - | - |
| NiSO ₄ ·(H ₂ O) ₇ | 1.78 | 5.24 | - |

- a. experimental report in Ref. (Coe, 2001)
- b. experimental report in Ref. (Roessler and Walker, 1967)
- c. experimental report in Ref. (Sawatzky and Allen, 1984)

First we discuss the electronic structure of MgO (**Figure 7.4a**). The ionic nature of this oxide indicates a simple electronic picture with three separate parts: (1) the O 2s states at about 15 eV below the Fermi level which is set at the top of the valence band; (2) the O 2p states dominating the valence band starting from about 5 eV up to the Fermi level; (3) the energy gap between the top of the valence band and the bottom of the conduction band. In this work, the calculated energy band gap of MgO is about 5.25 eV using the optB86-vdW density functional, which is smaller than the experimental value of 7.8 eV (Roessler and Walker, 1967). The eigen-character of the states at the bottom of conduction band for ionic compounds, such as MgO was dominated by O 3s states, rather than empty Mg 3s/sp states (de Boer and de Groot, 1998a; de Boer and de Groot, 1998b).

The crystal structure of NiO is similar to that of MgO. The only difference is that Ni (electronic configuration of 3d⁸ 4s² in the outer shell) is a 3d transition metal. NiO (3d⁸) is the prototype of a strongly correlated electron system (Hubbard, 1963; Larsson, 2006; Madsen and Novak, 2005; Sawatzky and Allen, 1984). The van der Waal density functional-GGA calculations shows a metallic behaviour even for the antiferromagnetic ordering (**Figure 7.4b** and **Figure 7.5a**). Furthermore, in contrast to the experimental observation (Larsson, 2006; Madsen and Novak, 2005; Sawatzky and Allen, 1984), the present calculation provided a low-spin solution with local moment of about 0.45 μ_B /Ni. When we employed the Hubbard U approach with $U = 5.96$ eV, $J = 0.0$ (Hubbard, 1963; Madsen and Novak, 2005), an energy gap of about 2.3 eV was obtained for the anti-ferromagnetic ordering. The Ni ions have high-spin state (2 μ_B /Ni). Although the calculated energy gap is still smaller than the experimental values (about 3.5 to 4.3 eV) (Larsson, 2006; Madsen and Novak, 2005; Sawatzky and Allen, 1984), the results are greatly improved by the Hubbard U approach (**Table 7.5**). For all the Ni-containing phases, our calculations also showed that

the anti-ferromagnetic solution is more stable. Therefore, all electronic calculations are based on the anti-ferromagnetic ordering for the Ni-containing phases (if possible) in the remainder of the paper.

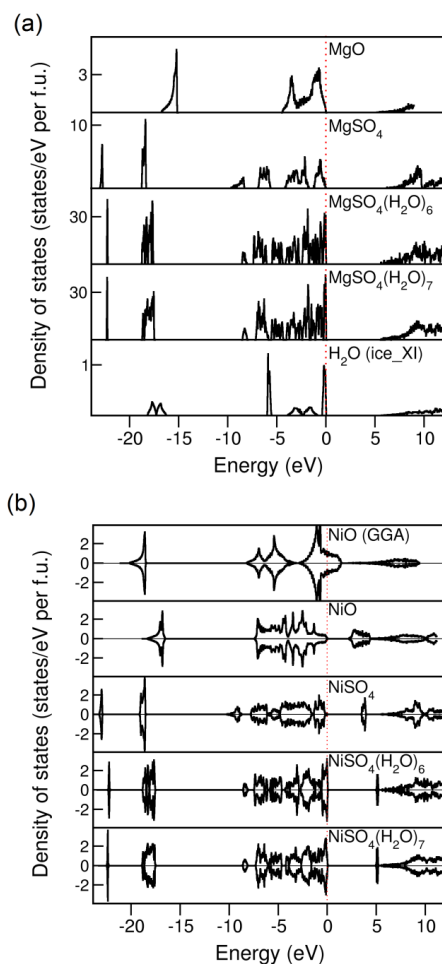


Figure 7.4 Total density of states (tDOS) from the periodic DFT calculations for (a) Mg-containing compounds and (b) Ni-containing compounds (AFM ordering) with Hubbard corrections for Ni 3d states.

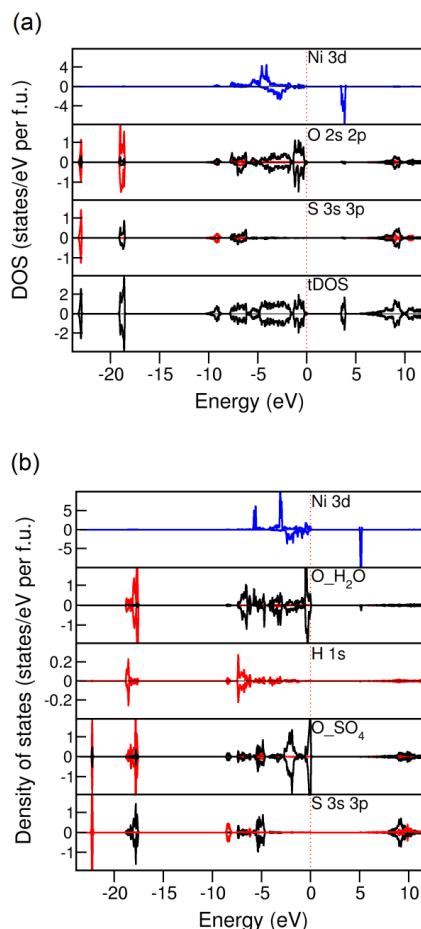


Figure 7.5 The partial density of states (pDOS) and total density of states (tDOS) from the periodic DFT calculations for (a) α -NiSO₄ and for (b) NiSO₄(H₂O)₆ computed using the optB86-vdW +U method. The red, black, and blue lines represent O 2s, O 2p and Ni 3d states, respectively.

As shown in **Figure 7.4** and **Figure 7.5b**, the electronic structures of the sulfates are more complex than the oxides. For Mg sulfate, there are six independent bands below the Fermi level. For Ni sulfate, the lowest narrow band at about -23 eV is dominated by S 3s states with some O sp character as well (**Figure 7.4a**). The second lowest band at about -18 eV is composed of O 2s states hybridizing with S 3sp states, which corresponds to the sp³ bonding in the tetragonal coordination in the (SO₄)²⁻ cluster. Such sp³ bonding can also be seen for the third and fourth bands consisting of S 3s and O 2p states (**Figure 7.4**). The top two band for magnesium sulfate (**Figure 7.4a**) are non-bonding O 2p states, while the bands in

the same region for the NiSO_4 originate from Ni 3d/O 2p mixing with the Ni 3d states dominating the upper part. The calculations give energy gaps for both MgSO_4 and NiSO_4 . However, the nature of bands are different: for MgSO_4 , the top of valence band is dominated by (nonbonding) O 2p states and the bottom of the conduction band by O 3s, while for NiSO_4 , both the top of the valence band and the bottom of the conduction band are dominated by Ni 3d states.

For the hydrated sulfates, the electronic structure is similar to that of anhydrous sulfates as shown in **Figure 7.4**. However, there are some notable differences: (1) the semicore S 3 bands and the Ni 3d bands of the hydrated phases become narrower than those of the corresponding anhydrous phases; (2) The calculated energy gaps of the hydrated Mg sulfates are smaller than that of the anhydrous phase, while for Ni sulfates, the opposite is true due to the longer Ni-Ni distances in the hydrated phases in comparison with the corresponding anhydrous phases.

As is shown in **Table 7.5**, the calculated band gaps for all $\text{MSO}_4(\text{H}_2\text{O})_n$ are relatively large (~ 5 eV), indicating all these hydrated Mg and Ni sulfates are intrinsically colorless. However, without available experimental data for comparison, the accuracy of the DFT-predicted energy gaps are unclear. DFT functionals in general underestimate the energy gaps of an insulator/semiconductors (Madsen and Novak, 2005; Perdew et al., 1996). The energy gaps calculated with optB86-vdW functionals (standard GGA) for the ice phase and the Mg-compounds are smaller than the experimental values, but in an acceptable range (**Table 7.5**). The calculated energy gaps for the Ni-compounds are too small, even for the metallic NiO phase (**Table 7.5**). Compared to the standard DFT-GGA method, the optB86-vdW-GGA+U approach significantly improves the calculated energy gaps for the Ni-compounds. However, the difference between DFT calculations and experimental data are significant. For example, the calculated band gap for NiO with Hubbard U approach is smaller than the experimental measurements. Besides the urgent needs of the improved new computational techniques, systematic experimental measurements about the electronic structures of these hydrate transition metal sulfates are worth future investigations.

7.4 Conclusions

In summary, we presented a comparative first-principles study for a series of Mg and Ni oxides, sulfates and hydrated sulfates, using both periodic and cluster DFT calculations. In the periodic DFT calculations, the van der Waals density functional (optB86-vdW) with Hubbard U for Ni 3d states was used. The calculated lattice parameters of all compounds agree well with the available experimental data. The total energy calculations showed a relatively small energy difference of the Mg substituted configuration of $\text{NiSO}_4(\text{H}_2\text{O})_n$ ($n = 6, 7$) for all concentrations. The energy differences are typically a few meV/f.u., which are smaller than kT (25.85 meV, $T = 300\text{K}$) indicating the formation of continuous solid solutions at ambient conditions. Considering the cumbersome computing in the periodic DFT calculation, we also

investigated the metal sulfates with the computationally less demanding cluster DFT calculations. Though a dimeric or tetrameric cluster contains only a few tens to a few hundred atoms, surprisingly good agreement was found in the calculated results of crystal structures and phase stabilities. This shows that large complex systems such as the hydrated metal sulfates can be efficiently investigated first principles methods. As there is a lack of systematic study of the electronic properties of the Hydrated metal (II) sulfates, we further extended our work to study the electronic structures of these compounds using the periodic DFT calculations. Our electronic structure calculations predict an insulating nature of the compounds. The itinerant nature of the localized Ni 3d states determines largely the electronic properties, in particular the energy gaps of the related phases.

References

- Spartan 14. Wavefunction Inc. www.wavefun.com, Von Karman Avenue, Suite 370, Irvine CA 92612.
- Abbas, A., Nobbs, D. and Romagnoli, J.A., 2002. Investigation of On-Line Optical Particle Characterization in Reaction and Cooling Crystallization Systems. *Current State of the Art. Measurement Science and Technology*, 13(3): 349.
- Amador, C., Lambrecht, W.R.L. and Segall, B., 1992. Application of Generalized Gradient-Corrected Density Functionals to Iron. *Physical Review B*, 46(3): 1870-1873.
- Bader, R.F.W. and Beddall, P.M., 1971. Spatial Partitioning and Transferability of Molecular Energies. *Chemical Physics Letters*, 8(1): 29-36.
- Bader, R.F.W., Nguyendang, T.T. and Tal, Y., 1981. A Topological Theory of Molecular-Structure. *Reports on Progress in Physics*, 44(8): 893-948.
- Bartel, L.C. and Morosin, B., 1971. Exchange Striction in NiO. *Physical Review B*, 3(3): 1039-1043.
- Baur, W.H., 1964. On Crystal Chemistry of Salt Hydrates .4. Refinement of Crystal Structure of $\text{MgSO}_4 \cdot 7\text{H}_2\text{O}$ (Epsomite). *Acta Crystallographica*, 17(11): 1361-1369.
- Benrath, A. and Neumann, E., 1939. Über Mischkristalle in der Vitriolreihe. V. *Zeitschrift für anorganische und allgemeine Chemie*, 242(1): 70-78.
- Bloch, P.E., 1994. Projector Augmented-Wave Method. *Physical Review B*, 50(24): 17953-17979.
- Carja, G., Husanu, E., Gherasim, C. and Iovu, H., 2011. Layered Double Hydroxides Reconstructed in NiSO_4 Aqueous Solution as Highly Efficient Photocatalysts for Degrading Two Industrial Dyes. *Applied Catalysis B-Environmental*, 107(3-4): 253-259.
- Coe, J.V., 2001. Fundamental Properties of Bulk Water from Cluster Ion Data. *International Reviews in Physical Chemistry*, 20(1): 33-58.
- Cox, W.P., Hornung, E.W. and Giauque, W.F., 1955. The Spontaneous Transformation from Macrocrystalline to Microcrystalline Phases at Low Temperatures - the Heat Capacity of $\text{MgSO}_4 \cdot 6\text{H}_2\text{O}$. *Journal of the American Chemical Society*, 77(15): 3935-3938.
- Dar, F.I., Moonoswamy, K.R. and Es-Souni, M., 2013. Morphology and Property Control of NiO Nanostructures for Supercapacitor Applications. *Nanoscale Research Letters*, 8: 363.
- de Boer, P.K. and de Groot, R.A., 1998a. Conduction Bands and Invariant Energy Gaps in Alkali Bromides. *European Physical Journal B*, 4(1): 25-28.
- de Boer, P.K. and de Groot, R.A., 1998b. The Conduction Bands of MgO, MgS and HfO_2 . *Journal of Physics-Condensed Matter*, 10(45): 10241-10248.
- Delorme, F. et al., 2009. Synthesis and Anion Exchange Properties of a Zn/Ni Double Hydroxide Salt with a Guarinoite Structure. *Journal of Solid State Chemistry*, 182(9): 2350-2356.
- Dion, M., Rydberg, H., Schroder, E., Langreth, D.C. and Lundqvist, B.I., 2004. Van der Waals Density Functional for General Geometries. *Physical Review Letters*, 92(24): 246401.
- Fang, C.M., van Huis, M.A., Sluiter, M.H.F. and Zandbergen, H.W., 2010. Stability, Structure and Electronic Properties of $\gamma\text{-Fe}_2\text{C}_6$ from First-Principles Theory. *Acta Materialia*, 58(8): 2968-2977.
- Fisher, R.A., Hornung, E.W., Brodale, G.E. and Giauque, W.F., 1967. Magnetothermodynamics of $\alpha\text{-NiSO}_4 \cdot 6\text{H}_2\text{O}$.I. Heat Capacity Entropy Magnetic Moment and Internal Energy from 0.4 Degrees to 4.2 Degrees K with Fields 0-90 Kg Along C Axis. *Journal of Chemical Physics*, 46(12): 4945-4958.

- Fortes, A.D., Wood, I.G., Alfredsson, M., Vocadlo, L. and Knight, K.S., 2006. The Thermoelastic Properties Of $MgSO_4 \cdot 7D_2O$ (Epsomite) from Powder Neutron Diffraction and Ab Initio Calculation. *European Journal of Mineralogy*, 18(4): 449-462.
- Fortes, A.D., Wood, I.G., Vocadlo, L., Brand, H.E.A. and Knight, K.S., 2007. Crystal Structures and Thermal Expansion of α - $MgSO_4$ and β - $MgSO_4$ from 4.2 to 300 K by Neutron Powder Diffraction. *Journal of Applied Crystallography*, 40: 761-770.
- Frazer, B.C. and Brown, P.J., 1962. Antiferromagnetic Structure of $CrVO_4$ and Anhydrous Sulfates of Divalent Fe, Ni, and Co. *Physical Review*, 125(4): 1283-1291.
- Fron del, C. and Palache, C., 1949. Retgersite, $NiSO_4 \cdot 6H_2O$ a New Mineral. *American Mineralogist*, 34(3-4): 188-194.
- Grevel, K.D. and Majzlan, J., 2009. Internally Consistent Thermodynamic Data for Magnesium Sulfate Hydrates. *Geochimica Et Cosmochimica Acta*, 73(22): 6805-6815.
- Hawthorne, F., 2012. A Bond-Topological Approach to Theoretical Mineralogy: Crystal Structure, Chemical Composition and Chemical Reactions. *Physics and Chemistry of Minerals*, 39(10): 841-874.
- Hehre, W.J., 2003. A Guide to Molecular Mechanics and Quantum Chemical Calculations. Wavefunction.
- Hubbard, J., 1963. Electron Correlations in Narrow Energy Bands. *Proceedings of the Royal Society of London Series a-Mathematical and Physical Sciences*, 276(1364): 238-257.
- Iype, E. et al., 2012. DFT Study on Characterization of Hydrogen Bonds in the Hydrates of $MgSO_4$. *Journal of Physical Chemistry C*, 116(35): 18584-18590.
- J.M. Kavitha and Mahadevan, C.K., 2013. Growth and Characterization of Pure Glycine Added Morenosite Single Crystals. *Int. Journal of Engineering Research and Applications*, 3(5): 1931-1940.
- Klimes, J., Bowler, D.R. and Michaelides, A., 2010. Chemical Accuracy for the van der Waals Density Functional. *Journal of Physics-Condensed Matter*, 22(2): 022201.
- Klimes, J., Bowler, D.R. and Michaelides, A., 2011. Van der Waals Density Functionals Applied to Solids. *Physical Review B*, 83(19): 195131.
- Koga, N. and Tanaka, H., 1994. Kinetic and Morphological-Studies of the Thermal Dehydration of α -Nickel (II) Sulfate Hexahydrate. *Journal of Physical Chemistry*, 98(41): 10521-10528.
- Kresse, G. and Hafner, J., 1993. Abinitio Molecular-Dynamics for Liquid-Metals. *Physical Review B*, 47(1): 558-561.
- Kresse, G. and Hafner, J., 1994. Ab-Initio Molecular-Dynamics Simulation of the Liquid-Metal Amorphous-Semiconductor Transition in Germanium. *Physical Review B*, 49(20): 14251-14269.
- Kresse, G. and Joubert, D., 1999. From Ultrasoft Pseudopotentials to the Projector Augmented-Wave Method. *Physical Review B*, 59(3): 1758-1775.
- Larsson, S., 2006. Localization of Electrons and Excitations. *Chemical Physics*, 326(1): 115-122.
- Lascelles, K., Morgan, L.G., Nicholls, D. and Beyersmann, D., 2005. Nickel Compounds, *Ullmann's Encyclopedia of Industrial Chemistry*. Wiley-VCH Verlag GmbH & Co. KGaA.
- Leadbetter, A.J. et al., 1985. The Equilibrium Low-Temperature Structure of Ice. *Journal of Chemical Physics*, 82(1): 424-428.
- Lu, X., Güner, F.E.G., van Spronsen, J., Oosterhof, H. and Witkamp, G.-J., 2014a. Eutectic Freeze Crystallization of Nickel Sulfate from an Industrial Stream: a Comparison with Evaporative Crystallization, Hydrometallurgy.
- Lu, X., van Spronsen, J., Güner, F.E.G. and Witkamp, G.-J., 2014b. Recrystallization of Nickel Sulfate Products from Industrial Solution, Hydrometallurgy.

- Luo, J.H., Zhang, Y.H. and Li, Z.S., 2013. Adsorption of Water on an MgSO_4 (100) Surface: A First-Principles Investigation. *Chemphyschem*, 14(9): 1969-1976.
- Madsen, G.K.H. and Novak, P., 2005. Charge Order in Magnetite. An LDA+U Study. *Europhysics Letters*, 69(5): 777-783.
- Maneva, M., Rizova, D., Genov, L. and Liptay, G., 1990. On the Thermal-Decomposition of $\text{NiSO}_4 \cdot 7\text{H}_2\text{O}$, $\text{NiSO}_4 \cdot 6\text{H}_2\text{O}$, $\text{NiSO}_4 \cdot 4\text{H}_2\text{O}$, $\text{NiSO}_4 \cdot 1\text{H}_2\text{O}$ and of Their Deuterated Analogs. *Journal of Thermal Analysis*, 36(3): 915-922.
- Maslyuk, V.V., Tegenkamp, C., Pfnur, H. and Bredow, T., 2005. Properties of Ternary Insulating Systems: The Electronic Structure of $\text{MgSO}_4 \cdot \text{H}_2\text{O}$. *Journal of Physical Chemistry A*, 109(18): 4118-4124.
- Moldoveanu, G. and Demopoulos, G., 2002. Producing High-Grade Nickel Sulfate with Solvent Displacement Crystallization. *JOM*, 54(1): 49-53.
- Monkhorst, H.J. and Pack, J.D., 1976. Special Points for Brillouin-Zone Integrations. *Physical Review B*, 13(12): 5188-5192.
- Nesbitt, H.W., Legrand, D. and Bancroft, G.M., 2000. Interpretation of Ni 2p XPS Spectra of Ni Conductors and Ni Insulators. *Physics and Chemistry of Minerals*, 27(5): 357-366.
- Nordstrom, D.K., 2009. Acid Rock Drainage and Climate Change. *Journal of Geochemical Exploration*, 100(2-3): 97-104.
- O'Connor, J.J., Beck, C. and Underwood, N., 1941. Magnetic Rotatory Power of Crystalline Nickel Sulfate in the Ultraviolet Region. *Physical Review*, 60(6): 443-447.
- Osborne, H.C., 1947. Nickelian Epsomite from North Auckland, New Zealand. *American Mineralogist*, 32(9-10): 553-560.
- Patterson, H.B.W., 1994. Hydrogenation of Fats and Oils: Theory and Practice Amer Oil Chemists Society.
- Perdew, J.P., Burke, K. and Ernzerhof, M., 1996. Generalized Gradient Approximation Made Simple. *Physical Review Letters*, 77(18): 3865-3868.
- Pontusch, Wm, Piccini, A., Quadros, C.J.A. and Isotani, S., 1973. EPR Measurements on Single-Crystals of $\alpha\text{-NiSO}_4 \cdot 6\text{H}_2\text{O}$. *Physics Letters A*, 44(1): 57-58.
- Ptasiewicz-Bak, H., Olovsson, I. and McIntyre, G.J., 1993. Bonding Deformation and Superposition in the Electron Density of Tetragonal $\text{NiSO}_4 \cdot 6\text{H}_2\text{O}$ at 25 K. *Acta Crystallographica Section B*, 49(2): 192-201.
- Ramachandran, P., Venkateswaran, K.V. and Visvanathan, S., 1991. The Electrochemical Recovery of Nickel from Plating Residues. *JOM*, 43(6): 34-36.
- Roessler, D.M. and Walker, W.C., 1967. Electronic Spectrum and Ultraviolet Optical Properties of Crystalline MgO . *Physical Review*, 159(3): 733-738.
- Sawatzky, G.A. and Allen, J.W., 1984. Magnitude and Origin of the Band-Gap in NiO . *Physical Review Letters*, 53(24): 2339-2342.
- Schlapp, R. and Penney, W.G., 1932. Influence of Crystalline Fields on the Susceptibilities of Salts of Paramagnetic Ions. II. The Iron Group, Especially Ni, Cr and Co. *Physical Review*, 42(5): 0666-0686.
- Schröder, D. et al., 2011. Direct Observation of Triple Ions in Aqueous Solutions of Nickel (II) Sulfate: A Molecular Link Between the Gas Phase and Bulk Behavior. *Journal of the American Chemical Society*, 133(8): 2444-2451.
- Smolik, M., 2000. Distribution of Trace Amounts of M^{2+} Ions during Crystallization of $\text{NiSO}_4 \cdot 7\text{H}_2\text{O}$. *Polish Journal of Chemistry*, 74(10): 1447-1461.

*Crystal Structure, Stability, and Electronic Properties of Hydrated Metal Sulfates $MSO_4(H_2O)_n$
($M=Ni, Mg$; $n=6, 7$) and Their Mixed Phases: A First Principles Study*

- Squyres, S.W. et al., 2004. In Situ Evidence for an Ancient Aqueous Environment at Meridiani Planum, Mars. *Science*, 306(5702): 1709-1714.
- Stout, J.W. and Hadley, W.B., 1964. Heat Capacity of α - $NiSO_4 \cdot 6H_2O$ between 1 - 20 K: Electronic Energy Levels of Ni^{++} Ion. *Journal of Chemical Physics*, 40(1): 55.
- Swift, T.J. and Connick, R.E., 1962. NMR-Relaxation Mechanisms of O_{17} in Aqueous Solutions of Paramagnetic Cations and the Lifetime of Water Molecules in the First Coordination Sphere. *The Journal of Chemical Physics*, 37(2): 307-320.
- Watanabe, T., 1962. Magnetic Properties of $NiSO_4 \cdot 7H_2O$ and α - $NiSO_4 \cdot 6H_2O$ at Low Temperatures. *Journal of the Physical Society of Japan*, 17(12): 1856-1864.
- Wells, A.F., 1984. *Structural Inorganic Chemistry*. Oxford University Press.
- Wildner, M., 1990. Crystal Structure Refinements of $CoSO_4$ and $NiSO_4$: Very Short Interpolyhedral O-O Contacts. *Zeitschrift für Kristallographie*, 191: 223-229.
- Wyckoff, R.W.G., 1921. The Crystal Structure of Magnesium Oxide. *American Journal of Science*, 1(2): 138-152.
- Zalkin, A., Templeton, D.H. and Ruben, H., 1964. Crystal Structure + Hydrogen Bonding of Magnesium Sulfate Hexahydrate. *Acta Crystallographica*, 17(3): 235-240.



Nieuwe Toepassingen van Eutectische Vrieskristallisatie

In de afgelopen decennia is de consumptie van grondstoffen en energie wereldwijd enorm toegenomen. Dit gaat gepaard met een vergelijkbare toename in industrieel afval waarvan de behandeling grote problemen stelt. Uit een economisch oogpunt heeft het afval waarde omdat het waardevolle materialen bevat. Daarnaast is het dumpen van onbehandeld afval onacceptabel. De voorzienbare uitputting van metaalhoudende ertsvoorraden, zuiver water en andere grondstoffen dwingt ons tot het ontwikkelen van efficiënte technologieën om deze grondstoffen terug te winnen. Dit proefschrift heeft als doel om nieuwe applicaties van eutectische vrieskristallisatie (EFC: Eutectic Freeze Crystallisation)) te ontwikkelen. Eutectische vrieskristallisatie is een veelbelovende kristallisatie technologie waarbij op energie vriendelijke wijze (tot 90% besparing op energie in vergelijking met verdampingskristallisatie) industriële stromen worden gescheiden in zuiver zout en zuiver water.

EFC werkt bij de eutectische temperatuur en samenstelling van een waterige oplossing. Het water en de in het water opgeloste zouten van de meeste proces stromen worden gescheiden in puur ijs en pure zouten. De lagere procestemperatuur ten opzichte van verdamping is veiliger in de procesvoering en minder corrosief voor de apparatuur. Toepassingen van EFC zijn mogelijk in de voedsel, farmaceutische, petrochemische, kunstmest en vergelijkbare industrieën.

De inleiding en de scope van dit proefschrift is beschreven in hoofdstuk 1, waarbij de focus is op de industriële toepassing van EFC in de chemische en de olie en gas industrie. HR-ICP-MS wordt toegepast als analytische methode om de zuiverheid van de verkregen producten te bepalen.

Hoofdstuk 2 beschrijft de toepassing van EFC op een NiSO_4 bevattende industriële stroom in batch uitvoering op 1 liter schaal in het laboratorium en in continu uitvoering op 200 l schaal op

een productielocatie van nikkelsulfaat. De warmte overdracht in de kristallisator kon gehandhaafd blijven op 9 kW/m² bij een productie snelheid van 16 kg ijs per uur en 4 kg nikkelsulfaat per uur. Omdat natrium ionen de grootste verontreiniging in de startoplossing zijn werden het quaternaire punt en twee eutectische lijnen van het ternaire fasesdiagram van Na₂SO₄-NiSO₄-H₂O bepaald. Met deze informatie konden de mogelijkheden van EFC voor deze industriële stroom bepaald worden.

Hoofdstuk 3 beschrijft de omkristallisatie van NiSO₄·7H₂O, geproduceerd uit een industriële stroom met EFC, in NiSO₄·6H₂O. In de range van 40-80°C werd het zuiverste product verkregen bij 50°C. Moederloog van de omkristallisatie werd gerecirculeerd in het omkristallisatieproces ter simulatie van een industrieel proces op volle schaal. Er werd geconstateerd dat de omkristallisatie een oplosmiddel gemedieerd proces is, waarbij de verontreinigingen zich over beide fasen herverdeelde. De HRICP-MS analyse resultaten werden gebruikt om de partitie en distributie coëfficiënten van de onzuiverheden over de twee fasen te bepalen.

Hoofdstuk 4 beschrijft de ontwikkeling en uitvoering van de HRICP-MS methode om sporenelementen in de diverse nikkelsulfaatstromen te bepalen. Ten eerste werd de concentratie van sporenelementen in de blanco oplossingen en in de standaarden bepaald. Ten tweede werd het geheugen effect gereduceerd door de spoeltijden te verlengen. Ten derde werd er in iedere run signaal afname geconstateerd die niet gecompenseerd kon worden door het hanteren van interne standaarden. Door te corrigeren voor signaalafname met behulp van standaard metingen gedurende de run konden betrouwbare meetgegevens verkregen worden.

Hoofdstuk 5 beschrijft het terugwinnen van waardevolle stoffen, met behulp van EFC op 1 liter batch schaal, uit water dat mee geproduceerd wordt bij de winning van olie uit Koeweit. Inclusies van moederloog in het finale ijsproduct zijn qua volume kleiner dan 0.05% en in het NaCl·2H₂O zoutproduct kleiner dan 0.1%. Vervolgens werd het EFC proces opgeschaald naar een 10 liter batch proces in een geschraapte wand kristallisator. Een maximum temperatuurverschil tussen de koelvloeistof en de NaCl·2H₂O/ijs slurry van 3.5°C kon gehandhaafd worden. De kwaliteit van het zout en het ijs op 1 en 10 liter schaal is vergelijkbaar. NaCl·2H₂O werd omgekristalliseerd in NaCl als een verdere zuiveringsstap waardoor een hoge kwaliteit NaCl verkregen werd.

Hoofdstuk 6 beschrijft de behandeling van gesimuleerd water (zoutoplossing), dat mee geproduceerd wordt bij de productie van schaliegas, met EFC. Het geproduceerde ijs was voldoende zuiver om weer te kunnen worden hergebruikt bij de schaliegaswinning. Door het stapsgewijze koelen in een batch EFC proces werd een gedeelte van het fasediagram van de oplossing met de eutectische punten van BaCl_2 , NaCl en SrCl_2 bepaald. Aan het einde van het batch experiment bevatte de oplossing voornamelijk CaCl_2 met nog enkele verontreinigingen. Het batch proces werd opgeschaald naar een 200 liter geschraapte wand kristallisator. In deze kristallisator kon een warmteoverdracht van 4kW/m^2 gehandhaafd worden zonder excessieve aankorsting op het inwendig oppervlak van de kristallisator.

Hoofdstuk 7 beschrijft de berekening van de fasestabiliteit van de hexa en heptahydraten van nikkel en magnesiumsulfaat en van de mengfasen met behulp van periodic Density Functional Theory (DFT) en cluster DFT. De berekende rooster parameters van $\text{MSO}_4(\text{H}_2\text{O})_n$ ($\text{M}=\text{Ni}, \text{Mg}$; $n=6,7$) zijn in goede overeenstemming met experimentele data. De relatieve energiever verschillen van de gemengde fasen van zowel de hexahydraat als de heptahydraat Ni/Mg sulfaten verkregen van zowel de periodic en cluster DFT berekeningen zijn kleiner als kT (25.8 meV , $T=300\text{K}$) wat aangeeft dat een continu vaste oplossing is gevormd.



Novel Applications of Eutectic Freeze Crystallization

During the last decades, the consumption of raw materials and energy in the world has faced a tremendous increase with a corresponding industrial waste volume increases, which treatment poses serious challenges. From an economical point of view, the waste has values as it contains valuable matters. Disposal of these streams without any further treatment is the environmentally unacceptable. The foreseeable upcoming depletion of metals, pure water and other raw materials forces us to find efficient technologies to recover those, and this thesis aims to investigate novel applications of a promising crystallization technology, Eutectic Freeze Crystallization (EFC) for the energy friendly (up to 90 % lower energy costs compared to evaporation) complete recovery of salt and fresh water from industrial streams.

EFC operates around the eutectic temperature and composition of an aqueous solution and recovers the dissolved salts and fresh water from almost all aqueous salt or acid containing process stream, producing extremely pure ice and pure salts. The low operating temperature promotes safe and corrosion-free operation. Applications are possible in food, pharmaceutical, petrochemical and fertilizer industries etc. An introduction and the scope of this thesis are given in **Chapter 1**. This work focusses on the industrial application of EFC in (bio-)chemical and oil and gas industries. HrICP-MS is used as an analytical tool to assess the purity obtained using EFC. In **Chapter 2**, EFC was performed for an NiSO_4 containing industrial stream from 1 liter scale batch set-up in the laboratory to an industrial scale continuous pilot plant (200 liter) at the production location of nickel sulfate. The heat transfer rate from the crystallizer could be maintained at 9 kW/m^2 with ice and nickel sulfate production rates of 16 and 4 kg/h respectively. Since the major impurity in the starting solution is sodium, the quaternary point and the two eutectic solubility lines for the Na_2SO_4 - NiSO_4 - H_2O ternary system were also experimentally determined to investigate the limitations of EFC.

Recrystallization of $\text{NiSO}_4 \cdot 7\text{H}_2\text{O}$ from produced with EFC into the $\text{NiSO}_4 \cdot 6\text{H}_2\text{O}$ is described in **Chapter 3**, and an effort of trace element analysis was performed by hrICP-MS. Within the range of 40°C to 90°C an optimal i.e. most pure product was found at 50°C . Recrystallization mother liquor was recycled to assess the performance in industrial full continuous operation. It was found that the recrystallization occurs via the solution, allowing a redistribution of impurities. The results

from hrICP-MS were used to calculate partition coefficients and distribution coefficients for impurity uptake in the NiSO_4 crystals. Efforts to develop and perform elemental analysis of traces in the nickel sulfate system using hrICP-MS are presented in **Chapter 4**. First, contaminations in blanks and standard solution were assessed, and calibration curves were measured. Second, observed memory effects (i.e. the signal is influenced by the signal of the preceding sample or standard) were reduced by extensive flushing. Third, a strong decrease on the sensitivity during one single run consisting of blanks, samples and standard solutions was observed, and it was surprisingly found that this effect could not be eliminated by using internal standards. By correction of the signal decline from standard curves at different stages within one run, and by performing three runs reliable data could be collected.

Chapter 5 describes how saline water from Kuwait oil production and valuable products were recovered by EFC in 1 liter batch experiment. Inclusions of mother liquor in the final ice product are below 0.05 wt%, and in $\text{NaCl}\cdot 2\text{H}_2\text{O}$ below 0.1 wt%. Then EFC was scaled up to batch 10 liter scraped wall crystallizer. A maximum ΔT of 3.5 °C between the cooling liquid and the $\text{NaCl}\cdot 2\text{H}_2\text{O}$ /ice slurry could be maintained. The quality of final salt and ice products have a good reproducibility from 1 liter to 10 liter. Recrystallization were performed from $\text{NaCl}\cdot 2\text{H}_2\text{O}$ into NaCl as a further purification step, yielding more pure NaCl.

Simulated shale gas water was treated with EFC (**Chapter 6**), and the ice products were deemed sufficiently pure to be reused in fracking fluid. By stepwise cooling down in a batch EFC process, the system of the solution with the eutectic points of BaCl_2 , NaCl and SrCl_2 was characterized. At the end of the batch sequence the solution will consist of calcium chloride with minor impurities. The batch process was scaled up in a 200 liter scraped wall crystallizer, and a heat transfer rate of 4 kW/m² over the heat exchangers could be maintained without excessive scaling inside the crystallizer.

In **Chapter 7**, an industrial problem of removing Mg from hydrated nickel sulfates using state-of-the-art molecular simulations was investigated. Periodic Density Functional Theory (DFT) and cluster DFT calculations are used to study the crystal structures and phase stability of the hexahydrated and heptahydrated Ni and Mg sulfates and their mixed phases. The calculated lattice parameters of $\text{MSO}_4(\text{H}_2\text{O})_n$ (M=Ni, Mg; n=6,7) crystals are in good agreement with available experimental data. The relative energy differences of the mixed phase for both hexahydrated and heptahydrated Ni/Mg sulfates obtained from both the periodic and cluster DFT calculations are generally less than kT (25.8 meV, $T = 300$ K), indicating that a continuous solid solution is formed.

Acknowledgement

Life will be lonely without the companion of friends; doing research will be difficult without the help of supervisors and colleagues. In my life, especially for this 5 years PhD study in Delft, I do have received lots of support from some nice people, and at the moment of the accomplishment for my PhD thesis, I would like to express my gratitude to all of you.

Firstly, I would like to thank my promoter Prof. dr. Geert Jan Witkamp for his supervision to this thesis's work. Dear Geert Jan, thank you sincerely for offering me this precious opportunity to do research on EFC project in Delft University of Technology. Without your support and encouragement, I wouldn't be able to accomplish my PhD study eventually. Working with you is a great pleasure and I do feel your strong knowledge background and novel ideas for EFC research. A heartfelt thanks for all the help from you.

Meanwhile, a hearty gratitude to my co-promoter Dr. Elif F. Genceli Güner for her valuable supervision on my research and kind help for my life in Delft. Dear Elif, thank you very much for your patient daily supervision, especially when I had problems. And also thank you for your kind personality that you supply lots of help on solving my staying difficulties in delft. I cannot forget your efficient guidance on correcting my PowerPoint for conferences which even occupied lots of your spare time, etc. I am so glad to meet you as my supervisor.

A gratitude also to Dr. Jaap van Spronsen for helping me finalize my thesis. Dear Jaap, thank you very much for your support. Without you, I wouldn't finish my thesis successfully. Thank you for all the help you provide, which guarantees the accomplishment of my thesis draft on time. I do appreciate.

Meantime, I would also like to thanks the China Scholarship Council (CSC) for the 4 years financial support, which offers me this opportunity of studying abroad. Also thanks to Ir. Cees Timmers. Dear Cees, I am glad to meet you as a manager for CSC project. Thank you to arrange my study in TUDelft, and especially, your kind help for the last year of my PhD. Without your support, I wouldn't pass this hard time myself. Meanwhile, I would also like to thanks Franca Post. Thank you, Franca, from the first moment for arranging nice accommodation for me in Delft till the ID extension application at the end of my study, your efficient work guarantees my stay in the Netherlands very comfortable.

Looking back on this 5 years in Delft, the accomplishment of my study cannot be done without the help from the Department of Process and Energy. First, I would like to thank our chairman, Prof. dr. ir. Bendiks Jan Boersma. Thank you for your powerful help on progressing my promotion, on providing support for printing this thesis and my stay in Delft, and especially the help during the summer holiday does encourage me to pass the last period before my defence. Also many thanks to Prof. dr. ir. Thijs.J.H. Vlugt. Dear Thijs, thank you for supplying the academic cooperation to my thesis, and for offering me a nice summer job last year, and for giving kind advices and help all the time when I had problems or met difficulties. Without your help, I wouldn't manage so many difficulties and finish my PhD successfully. Meanwhile, also thank Prof. dr. Wim Buijs. Thank you, Wim, for teaching me about computer simulations at the beginning when I have no background about it. Working with you is an enjoyable experience.

Since the main part of my research is based on experiments, I must thank Michel van den Brink. Thank you, Michel, for your patient explanations on my plenty questions. Without you, my experiments could not go well till the end. My gratitude to our dear secretaries, Rob, Helma, Ilona, Leslie and Eveline. Thanks very much for being always kind and helpful to me, especially the help for my 5th year. Also thank our workshop, I appreciate your kind help during my PhD study.

Great thanks to all my friends and colleagues from P&E: Alondra, Sara, Sergio, Stevia, Somayeh, Ivona, Marcos, Albert, Kamarza, Orchidea, Helene, Dennis. Thanks for sharing research life in TUDelft. Also thanks to Mattijs Huisman. You did help me a lot when I started my research on EFC. And Bart and Mohammed from EFC bv. also. Thank you for discussing with me on EFC topic and I do enjoy the talking with you.

Many thanks to Joanna and Frank, thank you for helping my Dutch. And to all of our excellent Summer School Group members, I enjoyed the time with all of you in Wuhan in 2013.

Also many thanks to my Chinese friends I met in the Netherlands. Liyuan Fan and Zhaochuan Fan, thank you for accompanying me during my most difficult emotional time and sharing trips to Germany and Greece. Without you, I couldn't pass that period for ever. To Ningjie Fu, I still cherish the memory with you in Delft for exercise together. Bing Liu, thanks for all the activities initiated by you. Xiangmei Meng and Ming Liu, thanks for giving me kind advice for life and research. Hua dong, Zihan Tan and Qu Chen, thank you for helping my moving in Delft. Also great thanks to the friends, Huaizhou Shi, Xiangyun Deng, Jie Lu, Hong Yan, Likun Ma, Xu Huang, Hongxia Zhou, Xiaogang Yang, Dongjuan Xiao, Fangliang Xiao, Jingang Wang, we do share the nice studying experience in Delft.

Heartfelt thanks to my supervisors in Shandong University and Shandong Jianzhu University, Prof. dr. Xiufang Bian, Xubo Qin and Prof. Guiqing Wang. Thank you for giving me kind guidance and support for my study and life. Also thanks to Yanwen Bai. Thank you for helping me assist all the documental work in China.

Special thanks to Tim Erken, for your encouragement and patience to help me pass my hardest time at the end of my PhD. And also thanks to let me enjoy the wonderful time with your kind family members. I feel very lucky to meet you on the plane.

At the end, I would like to say thanks to my dear mom and dad. Without the support from you, I cannot finish my PhD study successfully. I do feel the endless love from you which helps me to overcome all the difficulties in my life, and I do learn from you how to become a nice person. I gratitude for the love and care received from childhood, and your love is the precious possession in my life. I love you forever.

最后，我要衷心感谢我的爸爸妈妈，是你们的无限支持让我得以完成博士学业；是你们的无限关爱让我无惧人生道路上的任何困难；是你们朴实无华的教诲让我在完成学业之时更懂得如何做人。感谢你们用尽毕生精力对我的无微不至地培养。你们给予的无私的爱是我一生最为珍视的财富。爸爸妈妈，你们辛苦了！永远爱你们。

Xiaoqian Lu
August 2014 in Delft



Curriculum Vitae

Xiaoqian Lu

Born February 8th, 1984 in Jinan, Shandong Province, China.



| | |
|-------------|---|
| 2002 ~ 2006 | Undergraduate Bachelor of Material Science and Engineering Shandong Jianzhu University Jinan, China |
| 2006 ~ 2009 | Postgraduate Master – Doctor Combinnd Program of Material Science and Engineering Shandong University Jinan, China |
| 2009 ~ now | PhD Delft University of Technology Delft, the Netherlands |

Publications

Xiaoqian Lu, F.Elif Genceli Güner, Jaap van Spronsen, Harald Oosterhof, Geert-Jan Witkamp, Eutectic Freeze crystallization of Nickel Sulfate from an Industrial Stream: a comparison with evaporative crystallization. Prepared for submission to Hydrometallurgy.

Xiaoqian Lu, Jaap van Spronsen, F.Elif Genceli Güner, Geert-Jan Witkamp, Recrystallization of Nickel Sulfate products from Industrial Solution. Prepared for submission to Hydrometallurgy.

Xiaoqian Lu, F.Elif Genceli Güner, Essam El-Sayed, Ali Alodwani, Jaap van Spronsen, Geert-Jan Witkamp, Desalination of oil coproduced water by eutectic freeze crystallization, Prepared for submission to Desalination.

Xiaoqian Lu, Mohammed Aljirjawi, Jaap van Spronsen, Geert-Jan Witkamp, Eutectic Freeze Crystallization as a tool for separation of shale gas produced water into pure ice and salt by eutectic freeze crystallization. Prepared for submission to Desalination.

Changming Fang, **Xiaoqian Lu**, Wim Buijs, Zhaochuan Fan, F.Elif Genceli Güner, Marijn A. van Huis, Geert Jan Witkamp, Thijs J.H. Vlugt, Structure Stabilities and Electronic Structures of $\text{Ni}_x\text{Mg}_{1-x}(\text{H}_2\text{O})_n$ ($x=0\sim 1$, $n=6,7$): a Comparative First Principles Study, Chemical Engineering Science, accepted.

Conference

Xiaoqian Lu, F. Elif Genceli Güner, Jaap van Spronsen, Geert-Jan Witkamp, Nickel sulfate production by eutectic freeze crystallization, Netherlands Process Technology Symposium 2010 (NPS 10), 25-27 October, 2010, Veldhoven, the Netherlands.

Xiaoqian Lu, F. Elif Genceli Güner, Jaap van Spronsen, Geert-Jan Witkamp, Eutectic freeze crystallization for the production of pure sodium chloride, Netherlands Process Technology Symposium 2011 (NPS 11), 24-26 October, 2011, Arnhem, the Netherlands.

X. Lu, F.E. Genceli, J. van Spronsen, G.J. Witkamp, Desalination of oil coproduced saline water by eutectic freeze crystallization, Biwac 2012 – 19th international workshop on industrial crystallization, pp. 290-297, 7-9 September, 2012, Tianjin, China.

List of Publications

Xiaoqian Lu, Bart de Graaff, F. Elif Genceli Güner, Jaap van Spronsen, Geert-Jan Witkamp, Desalination of fossil fuel coproduced saline water by eutectic freeze crystallization, 9th European Congress of Chemical Engineering, 21-24 April 2013, the Hague, the Netherlands.

Xiaoqian Lu, Geert Jan Witkamp, F.Elif Genceli Güner, Recrystallization of Nickel Sulfate products from industrial solution, Biwic 2013 – 20th international workshop on industrial crystallization, 18-20 September, 2013, Odense, Denmark.

